Doctoral Dissertation

博士論文

Mapping the Universe with Weak Lensing from Subaru Hyper Suprime-Cam Survey

（すばるハイパースープリムカムサーベイ観測による重力レンズマップ生成）

A Dissertation Submitted for the Degree of Doctor of Philosophy

July 2021

令和 3 年 7 月 博士（理学）申請

Department of Physics, Graduate School of Science,
The University of Tokyo

東京大学大学院理学系研究科物理学専攻

Xiangchong Li

李翔翀

Abstract

ΛCDM model, which is the current standard cosmology model, provides a simple but reasonably good explanation of cosmological observations. In this model, the universe is dominated by dark energy (Λ) and cold dark matter (CDM)—roughly 68% of the universe is dark energy; 27% is dark matter; and less than 5% is normal matter. Both dark energy and dark matter behave substantially differently from normal matter. Dark energy has a negative pressure that can cause cosmological expansion. Dark matter only feels the force of gravity, whereas it does not interact electromagnetically.

Weak gravitational lensing, a phenomenon of light from distant galaxies being bent by foreground density fluctuations due to gravity, results in weak but coherent distortions on background galaxy images. Weak lensing hence offers a probe into the foreground mass distributions by measuring the coherent distortions from background galaxies. Since weak lensing is purely caused by gravitational effect, it is sensitive to not only normal matter but also dark matter. Using measurements of lensing distortions from a large ensemble of galaxy images across large areas of the sky, it is possible to reconstruct three dimensional (3D) mass maps that are majorly composed of the dark matter.

However, there are several difficulties in the 3D weak lensing mass map reconstruction: (i) Weak lensing distortions are only about 10% of galaxy's intrinsic shape dispersion, shape estimation error due to the sky variance, and the systematic errors. Controlling the systematics in the measurements of such small signals is challenging. (ii) Weak lensing distortions are proportional to the integral of masses along the line-of-sight. It is challenging to reconstruct a mass map with a good line-of-sight resolution from the integrated mass maps obtained from weak lensing distortions on a few source galaxy redshift planes.

In this thesis, I will first present the galaxy shear catalog measured from

the i-band imaging data from the Wide layer of the Hyper Suprime-Cam (HSC) Subaru Strategic Program (SSP) Survey observed between 2014–2019. The galaxy shapes are calibrated with image simulations that resemble the observing conditions of the survey based on galaxy images from the Hubble Space Telescope in the COSMOS region. The catalog covers an area of 433.48 deg^2 of the northern sky, split into six observational fields. The mean i-band seeing is 0.59 arcsec. With conservative galaxy selection criteria (e.g., i-band magnitude brighter than 24.5), the observed raw galaxy number density is 22.9 arcmin^{-2}. The shear calibration removes the galaxy property-dependent multiplicative shear estimation bias to a level: $|\delta m| < 9 \times 10^{-3}$. The bias residual δm shows no dependence on redshift in the range $0 < z \leq 3$. The requirements for cosmological weak-lensing science are defined for this shear catalog. In addition, potential systematics in the catalog are quantified using a series of internal null tests related to shear estimation.

Subsequently, I will reconstruct 3D weak lensing mass maps using the weak lensing distortions measured from galaxy images observed by the Hyper Suprime-Cam (HSC) survey—a large scale imaging survey target on weak lensing science. To be more specific, I will tackle the aforementioned challenges by (i) Develop realistic galaxy image simulations that can be used to validate and calibrate estimations of the weak lensing distortion; (ii) Develop a weak lensing distortion estimator with minimal dependence on calibration from image simulations; (iii) Develop a sparsity-based mass map reconstruction algorithm for high-resolution 3D mass map reconstructions.

Galaxy clusters, the most massive bounded objects in the universe, can be identified from the reconstructed 3D weak lensing mass maps. In addition, the mass maps provide both the redshift and the mass information of the identified galaxy clusters. The galaxy clusters detected from weak lensing 3D mass maps are matched to galaxy cluster catalogs detected according to galaxy distribution for cross comparison.

Contents

List of Figures

1

Introduction

Contents

This chapter introduces the cosmology model (Section 1.1) and the weak gravitational lensing (Section 1.2) that can be used to constrain the cosmology model (Section 1.3). Finally, Section 1.4 clarifies the motivation and outlines the structure of this thesis.

1.1 Cosmology

In this section, I briefly review the concordance cosmology, namely the ΛCDM cosmology model and the formation of the large scale structure in the Universe. Here

"Λ" refers to the cosmological constant which explains the accelerating expansion, and "CDM" refers to cold dark matter which plays an important role in the structure formation.

1.1.1 Geometry

The standard cosmology model is built up upon the cosmological principle suggested by observational evidence (e.g., Cosmic Microwave Background (CMB) Planck Collaboration et al., 2020)—When averaged over large scales, there are neither special position (homogeneous) nor special direction (isotropic) in the Universe.

The space-time consistent with the cosmological principle can be described by the Robertson-Walker metric:

$$ds^2 = -c^2dt^2 + a^2(t)\left(\frac{dr^2}{1-Kr^2} + r^2(d\theta^2 + \sin^2(\theta)d\phi^2)\right). \tag{1.1}$$

K is the spatial curvature of the Universe which takes the values 0 (flat Euclidean space), +1 (spherical geometry) or −1 (hyperbolic surface).

It has been discovered by Hubble that galaxies are receding from the Earth with velocities approximately proportional to their distance from the Earth for galaxies up to a few hundred million parsecs (Mpc) away, which indicates that the Universe is expanding. Recent observations using tape Ia supernova suggest that that the expansion of Universe is accelerating (Riess et al., 1998). As a result of the cosmological expansion, light travels through the space is stretched to longer wavelengths and appear to be redder. Cosmological redshift is defined as a monotonic function of the scale factor:

$$z(a) = \frac{1}{a} - 1\,. \tag{1.2}$$

The accelerating expansion of our Universe indicates that only $\sim 5\%$ of the energy density in the Universe is composed of baryonic matter and photon, and the rest $\sim 95\%$, e.g., dark energy ($\sim 69\%$), cold dark matter ($\sim 26\%$), has yet been directly detected in the laboratory. The density of cold dark matter (baryonic matter) is denoted as $\rho_{\rm cdm}$ (ρ_b), the matter density is defined as $\rho_m = \rho_{\rm cdm} + \rho_b$, and the relativistic matter (e.g. photon) density is defined as ρ_γ. In addition, the density of the cosmological constant and the curvature is defined as

$$\begin{aligned} \rho_\Lambda(z) &= \frac{\Lambda c^2}{8\pi G}, \\ \rho_k(z) &= -\frac{3K}{8\pi G a^2(z)}, \end{aligned} \tag{1.3}$$

where Λ is the cosmological constant.

Following the Einstein equations, the relation between the geometry and the matter density is given by

$$H^2(z) = \frac{8\pi G}{3}(\rho_m(z) + \rho_\gamma(z) + \rho_\Lambda + \rho_k)\,. \tag{1.4}$$

The density evolution of a specific type of matter "x" is given by

$$\rho_{\rm x} = \rho_{{\rm x};0} a^{-3(1+w)}, \tag{1.5}$$

where w is the equation of state parameter relating the density (ρ) and the pressure (P) of the density fluid as $P = w\rho c^2$. For relativistic particles such as radiation, $w = \frac{1}{3}$, whereas for non-relativistic particles, $w = 0$. Λ is the cosmological constant, and if taking the cosmological constant as a perfect fluid, the equation of state of dark energy should satisfy $w = -1$.

To simplify the notation, the critical density for the current Universe at $z = 0$ is defined as

$$\rho_{c;0} = \frac{3H_0^2}{8\pi G}, \tag{1.6}$$

where H_0 is the current value of the Hubble parameter. The fractional density of cosmological constant, CDM, baryonic matter, relativistic matter and curvature are defined as

$$\Omega_{\rm x} = \frac{\rho_{\rm x}}{\rho_c}\,. \tag{1.7}$$

The Hubble parameter at redshift z is related to its current value as

$$\begin{aligned} H(z) &= H_0 E(z), \\ E(z) &= \sqrt{\Omega_{m;0}\,(1+z)^3 + \Omega_{\gamma;0}\,(1+z)^4 + \Omega_{\Lambda;0} + \Omega_{k;0}\,(1+z)^2}, \end{aligned} \tag{1.8}$$

where the current fractional density for each component is denoted as $\Omega_{{\rm x};0}$.

From Equation (1.1), the distance between the source and the observer in the comoving frame is given by

$$\chi(z) = \int_0^z \frac{c}{H(z')} dz'\,. \tag{1.9}$$

The angular size of objects can be directly observed, which can then be converted to physical size using the called angular diameter distance defined as

$$D_A(z) = \frac{\chi(z)}{1+z}\,. \tag{1.10}$$

As the scales of BAO and CMB anisotropy peaks are known from physical models, the observed angular size can be used to determine the corresponding angular diameter distances D_A as a function of redshift, which can be used to probe the geometry of the Universe.

1.1.2 Power Spectrum of Density Fluctuations

I first explore the growth of perturbation in the linear regime, where the amplitude of the density fluctuation is sufficiently small ($|\delta| \ll 1$). With the definition of sound velocity for a matter component "x": $c_{\rm x} = \sqrt{\partial P_{\rm x}/\partial \rho_{\rm x}}$, the evolution equation of the density fluctuation for a single component cosmology is

$$\ddot{\delta} + 2\,\frac{\dot{a}}{a}\dot{\delta} - \left(\frac{c_{\rm x}^2}{a^2}\nabla^2\delta + 4\pi G\rho_{\rm x}\delta\right) = 0\,. \tag{1.11}$$

The density fluctuation is expressed as a superposition of sinusoidal functions to solve the equation:

$$\delta(t) = \int \delta_k(t) e^{i\vec{k}\cdot\vec{x}} d^3k\,. \tag{1.12}$$

The linear perturbation equation for each k-mode is obtained as follows

$$\ddot{\delta}_k + 2\,H\dot{\delta}_k + (\frac{c_{\rm x}^2}{a^2}k^2\delta_k - 4\pi G\rho_{\rm x}\delta_k) = 0\,. \tag{1.13}$$

As indicated by Equation (1.13), different Fourier modes (δ_k) evolves independently. According to the inflation theory, the primordial k-modes are independent; therefore, the power spectrum is given by

$$\left\langle \delta_k^\dagger \delta_{k'} \right\rangle = (2\pi)^3 P_{\rm lin}(\vec{k})\delta_{\rm D}^3(\vec{k} - \vec{k'}), \tag{1.14}$$

where $P_{\rm lin}$ is the linear power spectrum, and $\delta_{\rm D}$ is the Dirac delta function. This Gaussianity is confirmed bt the measurements of the of the CMB anisotropies (Komatsu et al., 2003). In addition, for the Universe when the scale factor equals a, structures grow only at the scales with

$$\lambda(a) = \frac{2\pi a}{|k|} > c_{\rm x}\sqrt{\frac{\pi}{G\rho_{\rm x}}} = \lambda_J, \tag{1.15}$$

where λ_J is known as Jeans length below which oscillations rather than gravitational collapses occur.

For the Universe composed of only non-relativistic matter at the late stage of Universe the pressure of which is negligible ($c_s = 0$), each wave mode grows indepen-

dently: $\delta_k(a) \propto D_+(a)$. Note, for this case, the structure growth is scale independent (independent of $\vec{k}$), hence the shape of the power spectrum does not change during the evolution.

For the Universe with relativistic matter and non-relativistic matter at the early stage of Universe, the k-modes with wavelength below the Jeans length grow slowly due to the damped oscillations of the photon-baryon fluid and the streaming of collisionless matter (e.g. hot dark matter, neutrino). The evolution of the power spectrum of density perturbations is described in terms of transfer functions $T(k)$ (Bardeen et al., 1986). The linear power spectrum is given by

$$P_{\rm lin}(k,z) = P_{\rm lin}(k,z_0)T^2(k)\frac{D_+^2(z)}{D_+^2(z_0)} \tag{1.16}$$

1.1.3 Halo Mass Function

In this section, I move on to the empirical model describing the structure in the nonlinear regime. Numerical simulations are required to model the nonlinear growth as the k-modes do not grow independently, and the mode-to-mode coupling modifies both the shape and amplitude of the power spectrum over the k-modes that are in nonlinear regime.

For a given smoothing scale R at redshift z, the variation of density contrast field is defined as

$$\sigma_R^2 = \int W_R(\vec{k})^2 P_{\rm lin}(\vec{k},z) d^3k, \tag{1.17}$$

where $W_R(\vec{k})$ refers to a top-hat filter in Fourier space which has the following form in configuration space:

$$W_R(\vec{x}) = \begin{cases} \frac{3}{4\pi R^3} & |x| < R \\ 0 & else\,. \end{cases} \tag{1.18}$$

The smoothed density filed follows a Gaussian distribution with zero mean and standard deviation of σ_R.

Following the Press-Schechter (PS) theory (Press & Schechter, 1974), for a given smoothing scale R at a epoch z, the smoothed density field will collapse into gravitationally bounded structure with mass $M \geq \frac{4\pi}{3}R^3\rho_m(z)$ if the smoothed overdensity exceeds the critical density δ_c. $\delta_c \approx 1.686$ is the critical overdensity for spherical collapse according to the linear structure growth (Bardeen et al., 1986). Therefore, the probability of the formation of virialized objects as a function of redshift z and scale R is

$$P(R,z) = \frac{2}{\sqrt{2\pi}\sigma(R,z)}\int_{\delta_c}^{+\infty} d\delta \exp\left(-\frac{\delta}{2\sigma^2(R,z)}\right)\,. \tag{1.19}$$

The number density of virialized objects in the range $[M,\ M + dM]$ is given by

$$\begin{aligned}\frac{dn(M,z)}{dM} &= \frac{\rho_m}{M}\left|\frac{dP(R,z)}{dR}\right|\frac{dR}{dM} \\ &= \sqrt{\frac{2}{\pi}}\frac{\rho_m \delta_c}{3M^2\sigma}e^{-\delta_c^2/2\sigma^2}\left|\frac{d\ln\sigma}{d\ln R}\right|,\end{aligned} \tag{1.20}$$

which is known as halo mass function. The halo multiplicity function is defined as

$$f(\sigma,z) = \frac{M}{\rho_m}\frac{dn(M,z)}{d\ln\sigma^{-1}}, \tag{1.21}$$

which has the following form in the PS theory:

$$f_{\rm PS} = \sqrt{\frac{2}{\pi}}\frac{\delta_c}{\sigma}e^{-\delta_c^2/2\sigma^2}. \tag{1.22}$$

The halo mass function is calibrated with N-body simulations by fitting the halo multiplicity function in, for example, Tinker et al. (2008).

1.2 Weak Gravitational Lensing

Weak gravitational lensing, the phenomenon that light from distant galaxies is bent by the density fluctuation along the line-of-sight, imprints the information of foreground perturbation to the background galaxy images. Since the lensing distortion is purely caused by gravity, it is sensitive to all the matter distribution, including both normal matter and dark matter, along the line of sight. Therefore, it offers a probe into the evolution of matter distribution in the Universe without relying on knowledge of the connection between dark matter and normal matter.

I first review the light deflection caused by lensing effect, which distort the angular positions on the transverse plane (Section 1.2.1). Since the angle distortion is not homogeneous, the lensing effect distorts the shapes of background galaxies, and the distortion is related to the projected mass of the foreground overdensity (Section 1.2.2).

1.2.1 Light Deflection

According to the general relativity, the line element for the space perturbed by the inhomogeneous density distribution can be written by

$$ds^2 = c^2(1 + 2\frac{\phi}{c^2})dt^2 - (1 - 2\frac{\phi}{c^2})dl^2, \tag{1.23}$$

where ϕ is the Newtonian gravitational potential perturbation (Mukhanov et al., 1992) with $\phi \ll c^2$. The deflection angle of light path due to the perturbation is given by

$$\vec{\alpha} = -\frac{2}{c^2}\int dl \nabla_{\perp}\phi, \tag{1.24}$$

where the integral is conducted along the light path, and the gradient operator is defined in the comoving coordinates. As a result of the light deflection, the angular position is distorted by

$$\beta_i = \frac{\partial}{\partial\theta_i}\Phi, \tag{1.25}$$

where $i = 1, 2$ are the indices of the angular position vector, Φ is the lensing potential defined as

$$\Phi = \frac{2}{c^2}\int_0^{\chi_s} d\chi_l \phi(\vec{\theta}, \chi_l)\frac{\chi_{ls}}{\chi_s\chi_l}\,. \tag{1.26}$$

The lensed position $\vec{\theta_l}$ of the source is related to the unlensed position $\vec{\theta_s}$ by

$$\vec{\theta_l} = \vec{\theta_s} - \vec{\beta}\,. \tag{1.27}$$

1.2.2 Image Distortion

The local distortion on galaxy images caused by gravitation lensing is a transform by Jacobian operator with matrix elements given by

$$\boldsymbol{J} = \delta_{ij} - \frac{\partial^2\Phi}{\partial\theta_i\partial\theta_j} = \begin{pmatrix} 1-\kappa-\gamma_1 & -\gamma_2 \\ -\gamma_2 & 1-\kappa+\gamma_1 \end{pmatrix}. \tag{1.28}$$

The elements of the Jacobian matrix can be written as second order derivatives of the lensing potential. The lensing convergence κ is defined as

$$\begin{aligned} \kappa &= \frac{1}{2}\left(\frac{\partial^2\Phi}{\partial\theta_x^2} + \frac{\partial^2\Phi}{\partial\theta_y^2}\right) \\ &= \frac{3H_0\Omega_{\rm m}}{2c}\int_0^{z_s} dz_l \frac{\chi_l\chi_{sl}(1+z_l)}{\chi_s E\left(z_l\right)}\delta(\vec{\theta}, z_l), \end{aligned} \tag{1.29}$$

and the spin-2 components (γ_1, γ_2) are defined as

$$\begin{aligned} \gamma_1 &= \frac{1}{2}\left(\frac{\partial^2\Phi}{\partial\theta_x^2} - \frac{\partial^2\Phi}{\partial\theta_y^2}\right), \\ \gamma_2 &= \frac{1}{2}\left(\frac{2\,\partial^2\Phi}{\partial\theta_x\partial\theta_y}\right). \end{aligned} \tag{1.30}$$

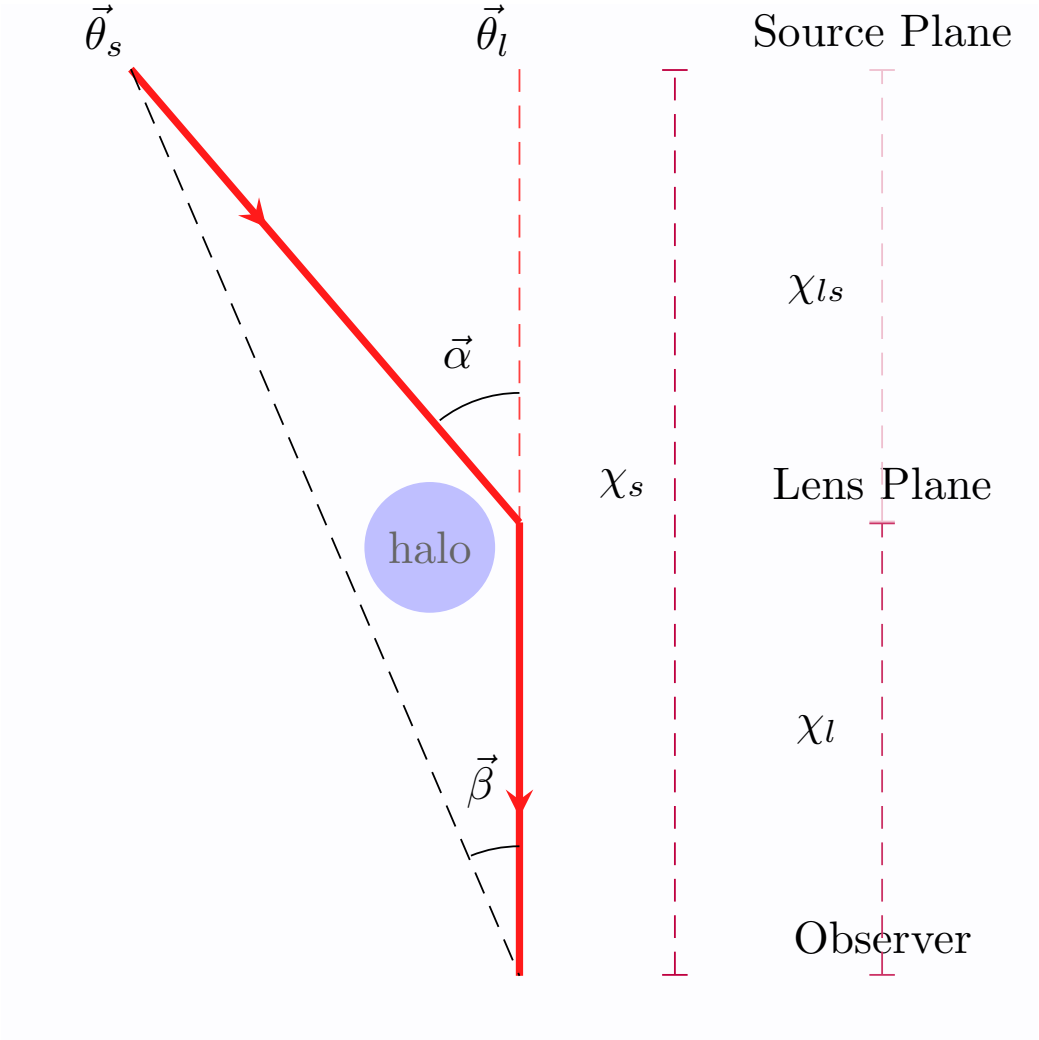

FIGURE 1.1: An illustration of gravitational lensing by a single lens, the effects of which are highly exaggerated. As light rays travel from a point source at $\vec{\theta}_s$ to observer their paths are distorted, the position of the point source are distorted. χ_l, χ_s, χ_{ls} are the comoving distance between lens, source and the observer.

κ isotropically changes the size and flux of galaxies, γ_1 anisotropically stretch galaxies along x-axis, whereas γ_2 anisotropically stretch galaxies along the $y = x$ direction. As a result, the lensing-shear distorts background galaxy images through a linear transform and perserve the surface brightness, which is given by

$$\begin{aligned} \vec{x}_I &= \mathbf{J} \cdot \vec{x}, \\ f(\vec{x}) &= f_I(\vec{x}_I)\,. \end{aligned} \tag{1.31}$$

f_I (f) is the surface brightness field of the intrinsic (lensed) galaxy; $\vec{x}_I$ ($\vec{x}$) refers to the local coordinates for the source (image) plane. In the weak lensing regime when

$\gamma_{1,2} \ll 1$ and $\kappa \ll 1$, the Jacobian matrix can be written into a reduced form:

$$\begin{aligned}\mathbf{J} =& \begin{pmatrix} 1-\kappa-\gamma_1 & -\gamma_2 \\ -\gamma_2 & 1-\kappa+\gamma_1 \end{pmatrix} \\ =&(1-\kappa)\begin{pmatrix} 1-g_1 & -g_2 \\ -g_2 & 1+g_1 \end{pmatrix},\end{aligned} \tag{1.32}$$

where $g_{1,2} = \gamma_{1,2}/(1-\kappa)$ is the reduced shear.

Even though the lensing shear distortion is too small to be precisely estimated on single galaxy level, with the assumption that intrinsic galaxies are randomly oriented (however, see Hirata & Seljak, 2004, for intrinsic alignment of galaxies), it is possible to infer the reduced lensing shear distortion from a large number of galaxies. However, controlling the systematics (e.g., from point-spread function, noise, and selection) in the measurements of such a small signal of such small signals is challenging.

1.3 Weak-lensing measurements

This section introduces two important measurements based on weak lensing shear distortion. The first one is cosmic shear measurement, which is the two point correlation functions of lensing-shear distortions (Section 1.3.1). It offers a direct probe into the matter power spectrum, which capture the linear information of the matter distortion in the Universe. The other one is peaks identified from weak lensing mass maps (Section 1.3.2). The peaks with high values offer a probe into the halo mass function, which is sensitive to non-Gaussian information of the matter distortion.

1.3.1 Cosmic shear

The standard estimates of cosmic shear two-point correlation functions, which is defined as

$$\xi_{\pm}(\theta) = \langle \hat{g}_+(\vec{r})\hat{g}_+(\vec{r}+\vec{\theta})\rangle \pm \langle \hat{g}_\times(\vec{r})\hat{g}_\times(\vec{r}+\vec{\theta})\rangle, \tag{1.33}$$

where the per-object shear estimates $\hat{g}$ for pairs of galaxies are decomposed into the tangential ($\hat{g}_+$) and cross component ($\hat{g}_\times$). As the lensing-shear distortion is related to the projected mass along the line of sight, the cosmic shear two-point correlation functions are related to the correlations of matter distortion, and thus related to the matter power spectrum introduced in 1.1.2. The relation between the shear-shear correlation and the power spectrum of κ field is given by

$$\xi_{\pm}(\theta) = \frac{1}{2\pi}\int dll J_{0,4}(l\theta)P_\kappa(l), \tag{1.34}$$

where P_κ is the power specturm of κ field, and J_0 (J_4) is the zeroth-order (fourth-order) Bessel function of the first kind. Adopting the flat-sky and the Limber approximations, the convergence power specturm can be computed from the nonlinear matter power spectrum P_δ via

$$P_\kappa(l) = \int d\chi \frac{q^2(\chi)}{\chi^2} P_\delta\left(\frac{l}{\chi}, \chi\right) . \tag{1.35}$$

The lensing efficienct function $q(\chi)$ is defined as

$$q(\chi) = \frac{3}{2}\Omega_m \left(\frac{H_0}{c}\right)^2 \int_\chi^{+\infty} d\chi' n(\chi')(1+z)\frac{\chi(\chi'-\chi)}{\chi'}, \tag{1.36}$$

where $n(\chi)$ denotes the source number distribution over comoving distance ξ . Readers can refer to Kilbinger (2015) for more details.

1.3.2 Peaks from weak lensing mass maps

The shear γ field can be converted to the convergence κ field via (Kaiser & Squires, 1993)

$$\kappa(\vec{\theta}) = \frac{1}{\pi}\int d^2\theta' \frac{\gamma_t(\vec{\theta'}|\vec{\theta})}{|\vec{\theta}-\vec{\theta'}|^2}, \tag{1.37}$$

where $\hat{\gamma}_t(\vec{\theta'}|\vec{\theta})$ is a tangential shear at position $\vec{\theta'}$ computed with respect to the reference position $\vec{\theta}$. Here we write the shear field and convergence field into complex form, and this transfrom is a convolution in two dimensional angular plane, which can be computed in Fourier space as

$$\tilde{\kappa}(\vec{l}) = \pi^{-1}\tilde{\gamma}(\vec{l})\tilde{D}^*(\vec{l}) \quad \text{for} \quad \vec{l} \neq \vec{0}, \tag{1.38}$$

where $\tilde{D}(\vec{l})$ is the Fourier transform of the convolution kernel in equation (1.37)

$$\tilde{D}(\vec{l}) = \pi\frac{l_1^2 - l_2^2 + 2il_1l_2}{|\vec{l}|^2} . \tag{1.39}$$

The convergence κ field in configuration space is then reconstructed by inverse Fourier transforming $\tilde{\kappa}(\vec{l})$.

The 2D convergence map is a projected integral of matter density map along the line of sight, which is given by Equation 1.29. Therefore, it is possible to identify the galaxy clusters, which are the most massive bounded object in the universe, from the peaks on the reconstructed convergence map with high values (Fan et al., 2010).

1.4 Motivation and Outline

1.4.1 Motivation

Currently, most of the observational studies on weak gravitational lensing focus on measuring two point correlation functions (Hamana et al., 2020; Hikage et al., 2019) and peak statistics on 2D mass maps (Miyazaki et al., 2018a). It is reasonable to ask whether it is possible to reconstruct 3D mass map from weak lensing shear distortions, locate galaxy clusters—the heaviest gravitationally bounded objects in the Universe—from 3D weak lensing mass maps and use the halo number density as a function of mass and redshift to constrain the cosmology model. There are two technical difficulties need to be overcome for the 3D mass map reconstruction and the 3D weak lensing galaxy cluster identification, which is summarized as follows:

- Weak lensing shear distortion is only about 10% of galaxy's intrinsic shape dispersion and shape measurement error due to photon noise. Controlling the systematics in the measurements (e.g., from point-spread function, noise, and selection) of such small signals is challenging.
- The weak lensing shear distortion on a source galaxy is proportional to the integral of structures along the line-of-sight from the observer to the source galaxy. It is challenging to derive a high-resolution mass map from integrated mass maps observed at a few source galaxy redshifts. That is, it is difficult to avoid smearing of structures along the line-of-sight.

This thesis tackles these difficulties and accurately estimate the cluster abundance as a function of galaxy cluster mass and redshift from weak gravitationally lensing only. Since only weak lensing measurements are used in deriving the cluster abundance, it is possible to fully quantify the systematics and errors using weak lensing mock catalogs generated from N-body simulations (e.g., Shirasaki et al., 2019). The measured cluster abundance can be used to constrain the standard ΛCDM cosmology model. Moreover, it is also possible to use the cluster abundance to constrain the neutrino mass sum (e.g., Li et al., 2019) and the dark energy model (e.g., Martinet et al., 2021).

1.4.2 Outline

This thesis presents the three-year HSC shear catalog that will be used for HSC weak lensing science and reconstructs 3D weak lensing mass maps using the three-year

HSC shear catalog. The structure of the thesis is demonstrated in Figure 1.2 and summarized as follows:

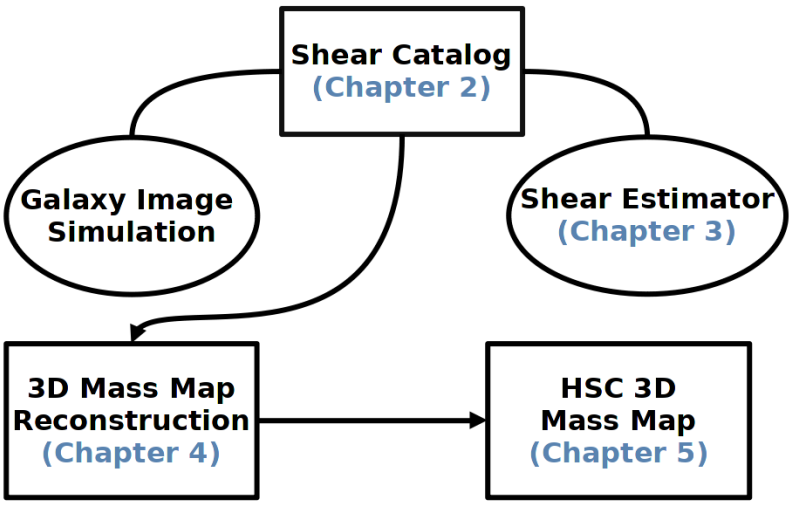

FIGURE 1.2: Outline of the dissertation.

Chapter 2 presents the galaxy shear catalog for the three-year cosmological weak gravitational lensing analyses using data from the Wide layer of the HSC-SSP survey following Li et al. (2021b). Realistic galaxy image simulations are constructed to test and calibrate the estimations of weak lensing shear distortions. The image simulations transform high-resolution, high-SNR galaxy images from the Hubble space telescope (Leauthaud et al., 2007) in the COSMOS region to the HSC-like images (Mandelbaum et al., 2018a) according to the observational condition of the HSC (e.g., noise and point-spread function). With a 24.5th magnitude cut, the number histograms over galaxy properties (including size, brightness, shape) of the simulated galaxies match those of the real HSC galaxies; that is, the difference between the simulation and observation is less than 1%. This galaxy image simulation is used to calibrate weak lensing measurement and produce galaxy shape catalogs.

Chapter 3 develops the `FPFS` estimator for weak lensing shear distortions with minimal dependence on calibrations from image simulations in the second part of Chapter 2 following Li et al. (2018); Li et al. (2020). The estimator uses four polar shapelet modes (Massey & Refregier, 2005) that are calculated from the power function of the Fourier transforms of galaxies after deconvolving the point-spread functions in Fourier space (Zhang & Komatsu, 2011) after deconvolving the PSF's

power function. The `FPFS` estimator is able to recovery weak lensing shear distortion with sub-percent level accuracy for isolated galaxies. However, unfortunately, it requires calibrations for a $\sim 5\%$ shear estimation bias under the conditions that blending exist.

Chapter 4 develops a sparsity-based mass map reconstruction algorithm for high-resolution 3D mass map reconstructions in Chapter 3 following Li et al. (2021a). The primary difficulty in the 3-D mass map reconstruction is that the lensing kernels for lens systems at different redshifts are highly correlated. As a result, the standard lasso sparsity algorithm, which uses the l^1 penalty for model selection and estimation, can not tell in which lens redshift bin the mass is located. Therefore, the mass maps reconstructed with the l^1 lasso algorithm suffer from smears of the structure along the line of sight. Therefore, the mass maps reconstructed with the l^1 lasso algorithm suffer from smears of the structure along the line of sight. The adaptive lasso is a derivative version of the lasso algorithm which applies adaptive weights to penalize different parameters. By using the adaptive lasso algorithm, the smears of the structure along the line of sight are eliminated since the adaptive lasso algorithm is an approximation of l^0 penalty, which prefers a sparser solution, and it is able to select the related models consistently regardless of the correlations between models Zou (2006). I propose to represent the clumpy density distribution as a summation of Navarro-Frenk-White halos (Navarro et al., 1997) with different scales in comoving coordinates to improve the line-of-sight resolution. The algorithm is able to detect halo with minimal mass limits of $10^{13.5}M_\odot/h$, $10^{14.3}M_\odot/h$, $10^{15.0}M_\odot/h$ for the low ($z < 0.3$), median ($0.3 \leq z < 0.6$) and high ($0.6 \leq z < 0.9$) redshifts, respectively. The redshifts estimated by the algorithm is slightly lower than the true redshift by 0.03 for halos with input redshifts ranging from 0.1 to 0.4. For halos at other redshifts, no obvious bias in redshift estimation is found.

Chapter 5 reconstructs 3D weak lensing mass maps using the weak lensing shear distortions measured from HSC galaxies (Li et al., 2021b) in Section 4. Galaxy clusters (groups), the most massive bounded objects in the Universe, are identified from the reconstructed 3D mass maps. In addition, the mass map provides redshift and mass information of the identified galaxy clusters (groups). The galaxy clusters (groups) detected from weak lensing 3D mass maps are matched to cluster catalogs detected from the distributions of galaxies for cross-comparison.

2

HSC three-year shear catalog

Contents

This chapter introduces the three-year shear catalog for the Hyper Suprime-Cam (HSC) Survey weak-lensing science. First, the three-year HSC Survey is summarized in Section 2.1. Second, the requirements on the control of systematics is determined according to the expected SNR of the cosmic shear signal in Section 2.2. Then Section 2.3 describes the basics of image processing for the HSC survey. Section 2.4 introduces the realistic galaxy image simulation that is used to calibrate the shear estimation, and Section 2.5 calibrate the galaxy shape measured by the `reGauss` shear estimator (Hirata & Seljak, 2003). Section 2.6 conducts "null tests" related to galaxy and star shapes within the shear catalog.

2.1 Hyper Suprime-Cam (HSC) Survey

Galaxy imaging surveys have given us information about the contents of the Universe for nearly a century. The ongoing Stage III wide-area multi-color surveys setting weak lensing as their primary science goal are: the Kilo-Degree Survey[1] (KiDS; de Jong et al., 2013), the Dark Energy Survey[2] (DES; Dark Energy Survey Collaboration et al., 2016), and the Hyper Suprime-Cam survey[3] (HSC; Aihara et al., 2018a). In the coming decade, three Stage IV imaging surveys will become available and promise to place further stringent constraints on cosmological parameters including the nature of dark energy and dark matter, the neutrino mass. Those are the Euclid satellite mission[4] (Laureijs et al., 2011), Vera C. Rubin Observatory's Legacy Survey of Space and Time [5] (LSST; Ivezić et al., 2019), and the Nancy Grace Roman Space Telescope[6] (Spergel et al., 2015).

[1] http://kids.strw.leidenuniv.nl
[2] https://www.darkenergysurvey.org
[3] https://hsc.mtk.nao.ac.jp/ssp/
[4] https://sci.esa.int/web/euclid
[5] https://www.lsst.org
[6] https://roman.gsfc.nasa.gov

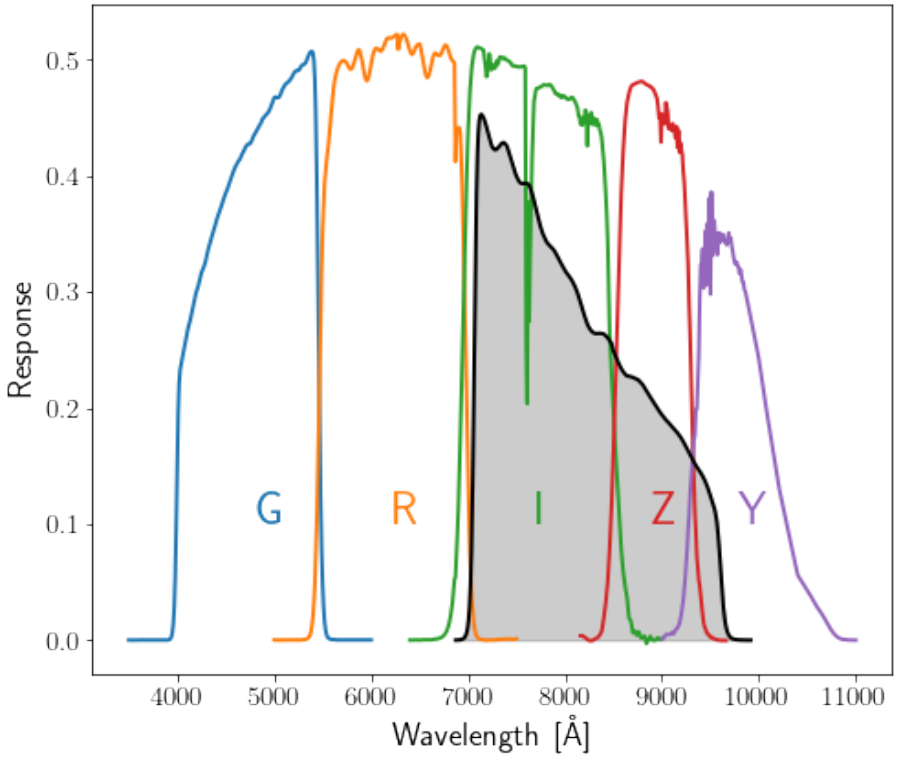

FIGURE 2.1: The colored lines show the filter responses of the *grizy*-bands of the HSC imager. The grey region shows the filter response of the F814W band of HST.

Hyper Suprime-Cam (Aihara et al., 2018a, HSC) Survey is a multi-band (i.e., *grizy* broad-bands plus 4 narrow bands) imaging survey using the Hyper Suprime-Cam mounted on the Subaru telescope (Miyazaki et al., 2018b). Subaru telescope is an optical-infrared telescope with a diameter of 8.2 m located at the summit of Maunakea, Hawaii, and operated by the National Astronomical Observatory of Japan (NAOJ). The filter responses of the broad bands are demonstrated in Figure 2.1. As shown, the response of the i-band filter has a large overlap with the F814W band of the Hubble Space Telescope (HST; Koekemoer et al., 2007).

The HSC imager has 104 science CCDs with a field-of-view 1.8 deg^2 and a $0\farcs168$ pixel scale. Thanks to the large field-of-view, the wide layer of the HSC survey covers ~ 1400 deg^2 with an optical depth of ~ 26 in i-band. The average seeing size is $\sim 0\farcs6$ in the i-band.

The HSC survey is awarded 330 nights over six years and it started in March 2014. The target observational footprint of the HSC survey is shown in Figure 2.2, which is from hscMap[7]. As shown, the HSC survey has overlaps with the Sloan Digital Sky Survey (SDSS) Baryon Oscillation Spectroscopic Survey (BOSS) footprint, as the

[7] https://hscmap.mtk.nao.ac.jp/

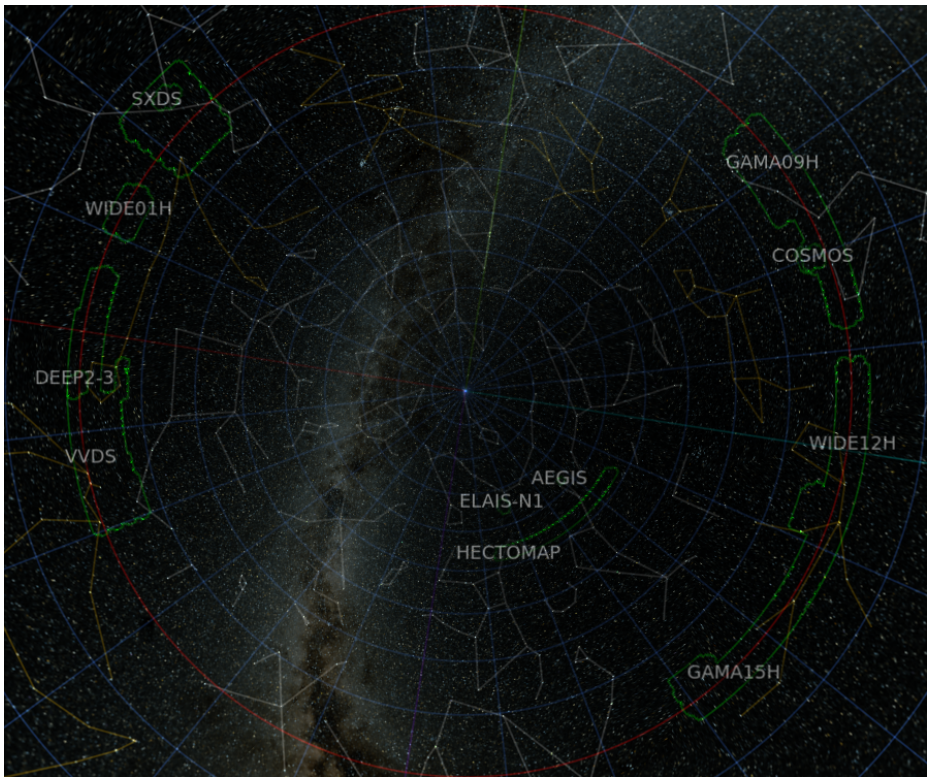

FIGURE 2.2: The green boundary shows the region covered by the second public data release of the HSC survey The figure is from hscMap.

SDSS/BOSS sources are used as a baseline of photometric and astrometric calibration. Further more, the HSC footprint covers the COSMOS region that is observed by the HST with a depth of roughly 24.5th magnitude. The COSMOS HST image recorded in the F814W band has a much smaller seeing size and lower noise variance. Therefore, the COSMOS HST images serve as a baseline for the calibration of galaxy shape measurements. The three-year HSC weak-lensing shear catalog is based on the S19A internal data release, which was acquired from March 2014 to April 2019 and released in September 2019. The S19A images are processed with `hscPipe` v7.

2.2 Requirement on the Control of Systematics

Accurate shear estimation is challenging due to a number of systematics Mandelbaum (see 2018, for review on weak lensing realted systematics). Considering that shear distortion is small in the weak lensing regime, the relation between the estimated shear and the true shear is quantified as follows if $O(g^4)$ of the small shear distortion is neglected:

$$\hat{g}_\alpha = (1+m)g_\alpha + a\, e_{\mathrm{PSF},\alpha}, \tag{2.1}$$

where m is referred to as multiplicative bias; a is referred to as the fractional additive bias that quantifies the fraction of the PSF anisotropy leaking into the shear measurement. The two components of the additive bias are given by $c_\alpha \equiv a\, e_{\mathrm{PSF},\alpha}$, where $e_{\mathrm{PSF},\alpha}$ refers to the ellipticity of PSF that quantifies the PSF anisotropy.

One of the systematics in the weak lensing shear estimation is the smearing from point spread functions (PSFs) caused by the light diffraction by telescopes and the atmosphere, and the pixel response. PSFs change the shape of galaxies, the bias of which to the shear measurement should be quantified and removed. In addition, galaxy images are contaminated by photon noise due to the sky variance. Furthermore, in the deep, ground based imaging survey (e.g., HSC and LSST), blending of galaxies become a severe problem in the shear estimation.

In order to set meaningful requirements on the control of systematic residuals, it is improved to estimate the statistical error – the standard deviation of which is denoted as σ_{stat} – that can be obtained from a cosmological analysis. This is beacuse only the systematic residuals with significances that are comparable to or greater than the statistical uncertainty should be modelled and removed from the weak lensing measurement. For the three-year HSC weak lensing science, the systematics are required to be less significant than $0.5\,\sigma_{\mathrm{stat}}$ to ensure that the systematic residuals are subdominant. Note, such a requirement is on the systematic residuals after the removal of known biases that are expected to be calibrated before the use of a catalog.

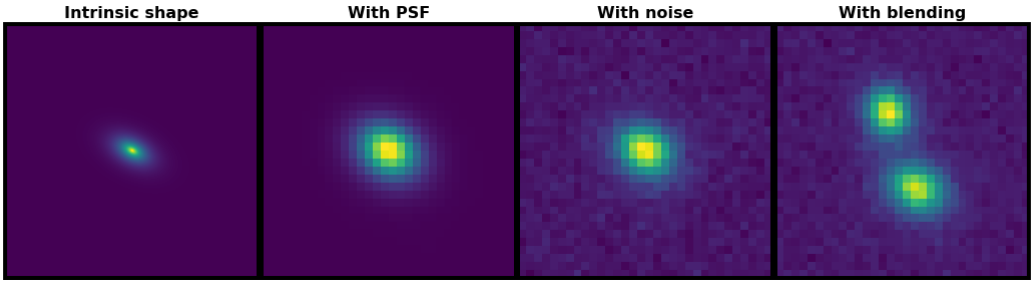

FIGURE 2.3: The changes in the galaxy profile by the systematics. The intrinsic galaxy shape (*leftmost*), PSF smear added (*middle-left*), photon noise added (*middle-right*), blending added (*rightmost*).

The requirements are assessed in terms of residuals on multiplicative and fractional additive bias (i.e., δm and δa, respectively) in shear estimation. Multiplicative bias and fractional additive bias are defined in Equation (2.1).

Cosmic shear (Hamana et al., 2020) and galaxy-galaxy lensing (Prat et al., 2018) are two of the most important weak lensing cosmological analysis based on the shear catalog. Since the requirements on control of systematic residuals for galaxy-galaxy lensing are comparable with that for cosmic shear, the requirements on systematic residuals are determined only using the expected covariance of the cosmic shear measurements, i.e., the shear-shear correlation functions. The covariance is estimated by rescaling the covariance matrix, denoted as $\mathbf{C}$, of the first-year shear-shear correlations, which is estimated with mock galaxy catalogs (e.g., Shirasaki et al., 2019), by the inverse-square of the galaxy number ratio between the three-year catalog versus the first-year catalog.

The shear-shear two-point correlation functions are defined as

$$\xi_{\pm}(\theta) = \langle \hat{g}_{+}(\vec{r})\hat{g}_{+}(\vec{r}+\vec{\theta})\rangle \pm \langle \hat{g}_{\times}(\vec{r})\hat{g}_{\times}(\vec{r}+\vec{\theta})\rangle \,, \tag{2.2}$$

where the per-object shear estimates $\hat{g}$ for pairs of galaxies are decomposed into the tangential ($\hat{g}_{+}$) and cross component ($\hat{g}_{\times}$). TreeCorr[8] (Jarvis et al., 2004), a public package for fast measurements of correlation functions using a ball tree method (similar to a k-d tree), is used to compute the correlation functions.

Mandelbaum et al. (2018b) used a covariance matrix measured from mock catalogs (Shirasaki et al., 2017) to estimate the SNR for a cosmic shear measurement without tomographic binning. The estimated SNR is 12.6 for angular scales $5' < \theta < 285'$. Cosmic shear analyses have been conducted using the first-year HSC shear catalog in both configuration space (Hamana et al., 2020) and Fourier space (Hikage et al.,

[8]https://github.com/rmjarvis/TreeCorr/

2019) with a tomographic binning into four redshift ranges. The SNRs of 15.6 and 18.4 were achieved with a fiducial multi-pole range $300 < l < 1900$ and an angular range $4' < \theta < 50'$ using the first-year HSC mock galaxy catalogs (Shirasaki et al., 2019), respectively. The differences in the SNR measurements are mostly accounted for by the different angular (multi-pole) ranges, tomographic setups and cosmological models adopted by these studies. An average of them are calculated and then rescaled according to the increase in galaxy number thanks to to the increase of survey area in the three-year shear catalog. The resulting SNR for the three-year HSC cosmic shear measurements is $\mathrm{SNR}_{s-s} = 27$. Although tomographic SNR measurements are used when deriving SNR_{s-s}, a non-tomographic formalism is adopted when deriving the requirements in the following context for simplicity.

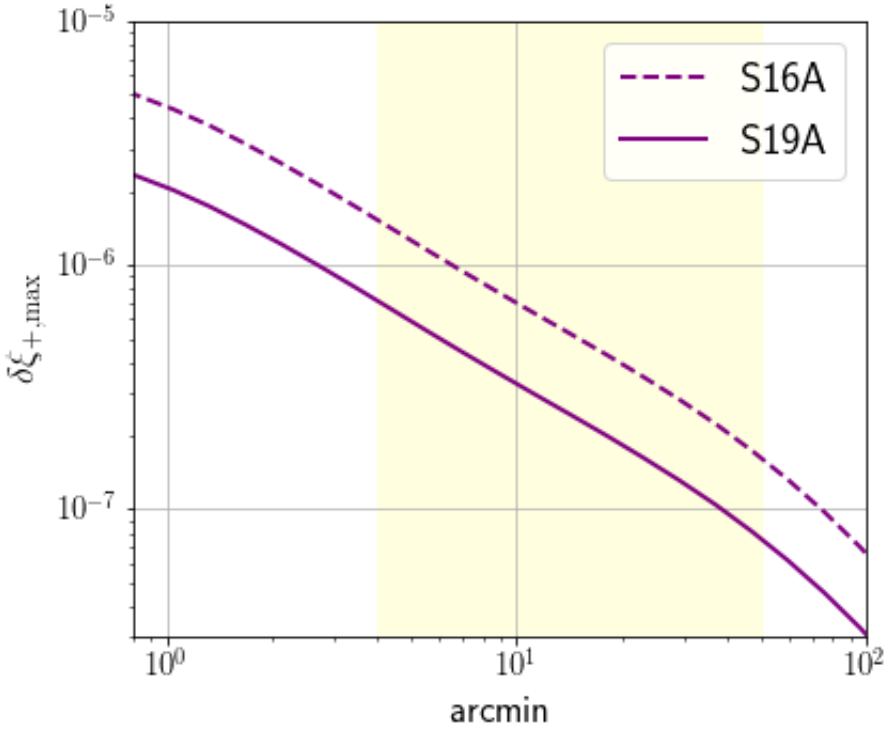

FIGURE 2.4: The dashed (solid) line demonstrates the maximum amplitude of the systematic residuals on the shear-shear correlation function as a function of angular scale required by the S16A (S19A) HSC weak-lensing science. The light-yellow area refers to the angular scales used for the cosmic shear measurements.

This SNR is used to derive the upper-limit of the amplitude of systematic residuals on the cosmic shear as

$$\delta\xi_{\pm,\mathrm{max}}(\theta) = \frac{\xi_{\pm}(\theta)}{2\,\mathrm{SNR}_{s-s}}\,. \tag{2.3}$$

This upper-limit of the systematics, which is demonstrated in Figure 2.4, has a sta-

tistical significance of 0.5σ since

$$\vec{\delta\xi}^{T}_{\pm,\max} \cdot \mathbf{C}^{-1} \cdot \vec{\delta\xi}_{\pm,\max} = 0.25\,. \tag{2.4}$$

That is, the amplitude of the systematic residuals originated from any sources on the cosmic shear measurement is required as

$$|\delta\xi_{\pm}| < \delta\xi_{\pm,\max}\,. \tag{2.5}$$

2.2.1 Multiplicative bias residuals

First, I place a requirement on the overall residual of multiplicative shear bias (δm) by focusing on the condition that the additive bias is zero to focus on multiplicative bias residuals. After neglecting the high-order terms of δm with the assumption: $\delta m \ll 1$, the cosmic shear measurements are influenced by the multiplicative bias as follows:

$$\langle \hat{g}^{\dagger}\hat{g}\rangle \approx (1 + 2\,\delta m)\langle g^{\dagger}g\rangle, \tag{2.6}$$

where $g^{\dagger}$ refers to the complex conjugate of complex shear $g = g_1 + i\,g_2$. The resulting systematic residual on the correlation function due to the multiplicative bias residual is given by

$$\delta\xi_{+,\delta m} = 2\,\delta m\,\xi_{+}\,. \tag{2.7}$$

According to Equation (2.5), the requirement on the overall multiplicative bias is

$$|\delta m| \lesssim \frac{0.25}{\mathrm{SNR}_{\text{s-s}}} = 9.3 \times 10^{-3}\,. \tag{2.8}$$

Here the integrated SNR ($\mathrm{SNR}_{\text{s-s}} = 27$) for cosmic shear is adopted. Not that, this requirement is a factor $\sim \sqrt{3}$ more stringent compared to the first-year requirement on the overall multiplicative bias.

2.2.2 Additive bias residuals

Then I place a requirement on the correlation of the overall additive shear bias residual (δc), which can originate from, e.g., an inadequate removal of systematics related to PSF in the shear estimation and PSF model shape errors. Similar to Section 2.2.1, I focus on the additive bias residual (δc) and assume that $\delta m = 0$. The additive bias (c) propagates into an additive term in the cosmic shear measurements via

$$\langle \hat{g}^{\dagger}\hat{g}\rangle = \langle g^{\dagger}g\rangle + \langle \delta c^{\dagger}\delta c\rangle\,. \tag{2.9}$$

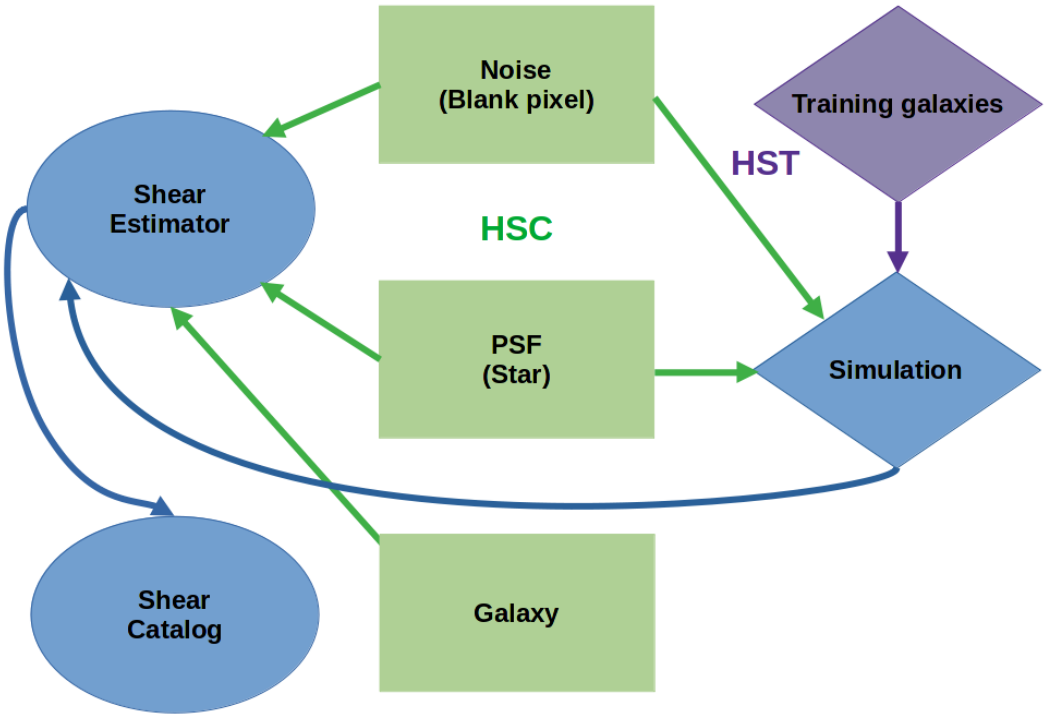

FIGURE 2.5: Basic outline of the weak lensing shear estimation process.

The systematic residuals on the cosmic shear estimations that originate from additive bias residuals are hence given by

$$\delta\xi_{+,\delta c} = \langle \delta c^{\dagger} \delta c \rangle \,. \tag{2.10}$$

According to Equation (2.5) and the conservative integrated SNR ($\mathrm{SNR}_{\text{s-s}} = 27$), the requirement on the correlation of fractional additive bias is given by

$$\begin{aligned} \langle \delta c^{\dagger} \delta c \rangle &< \frac{\xi_{+}(\theta)}{2\mathrm{SNR}_{\text{s-s}}} \\ &= \frac{\xi_{+}(\theta)}{54}. \end{aligned} \tag{2.11}$$

From the relation $\delta c = \delta a e_{\mathrm{PSF}}$, the requirement on $\langle \delta c^{\dagger} \delta c \rangle$ is transformed into the requirement on $\langle \delta a \delta a \rangle$:

$$\langle \delta a \delta a \rangle < \frac{\xi_{+}(\theta)}{54 \langle e^{\dagger}_{\mathrm{PSF}} e_{\mathrm{PSF}} \rangle (\theta)}. \tag{2.12}$$

The cosmic shear measurements are influenced by the baryonic effects at small

scales, and the measurements suffer from systematics related to PSF at large scale (Hamana et al., 2020). Therefore, I only consider the ξ_+ measurements on scales from $4'$ to $50'$ following Hamana et al. (2020). The quantity $\langle \delta a \delta a \rangle$ declines as a function of length scale, ranging from $\sim 2.0 \times 10^{-4}$ at the minimum scale of $\theta = 4'$ to $\sim 4.3 \times 10^{-5}$ at $\theta = 50'$ since the scale-dependence of the PSF-PSF shape correlation is much flatter than that of the cosmic shear correlation function. The geometric mean of these values is used to set the requirement on the fractional additive bias, requiring $|\delta a|^2 < 9.4 \times 10^{-5}$, or $|\delta a| < 9.7 \times 10^{-3}$. Since the conservative integrated SNR is used in this equation, it is not necessary to use the lowest $\langle \delta a \delta a \rangle$ value as well.

2.3 HSC pipeline

The HSC pipeline (Bosch et al., 2018) is built upon the prototype pipeline that will be finally applied to processing the LSST images (Bosch et al., 2019). The pipeline first detects sources from CCD images, and conducts source properties (e.g., centroid, flux, size and shapes) measurements. Then it performs astrometry and photometry calibration. After that, single exposure CCD images covering the same region on the transverse plane are resampled onto a common grid, and the resulting image is called coadded image. Finally, source detection and source property measurements are run again on the coadded images.

Here I introduce the catalog production (i.e., source detection and source property measurements) in Section 2.3.1. The coadding algorithm introduced in Section 2.3.2, and the background subtraction algorithm is introduced in Section 2.3.3. Note, the summary presented here is based on `hscPipe` v7, which is used to process the S19A internal data release. Readers can check the HSC pipeline paper and the latest HSC data release paper for the histories and latest updates of the pipeline (e.g., Bosch et al., 2018; Aihara et al., 2019).

2.3.1 Source detection and property measurement

2.3.1.1 Detecting source from background

The HSC pipeline first performs a maximum likelihood detection with a 50σ threshold from images. Each detected peak is regarded as a source object, and the connected neighboring region above the threshold is identified as the footprint of the source. Then the pipeline performs a background estimation using the undetected pixels, and the estimated background is subtracted from CCD images with a Chebyshev

fitting. After that, the pipeline run a deeper detection with a 5σ threshold. Finally, background are estimated from the undetected pixels (with respected to the deep source detection) and subtracted from CCD images. We note that the bad pixels (e.g., saturated pixels, pixels with cosmic rays) are also identified and labelled at the source detection stage.

2.3.1.2 Deblending

Under the condition that one footprint contains multiple number of peaks, we use the deblender of the HSC pipeline to apportions the flux to different peaks. The HSC pipeline adopts the SDSS deblender (Lupton et al., 2001) to isolate blended objects. It takes each peak in the footprint as a "child" source. With the assumption that each object is 180° rotational symmetric with respect to its peak, a template $T_i(\vec{x})$ for each "child" source is given by

$$T_i(\vec{x}) = \min(f(\vec{x}), f(2\vec{p}_i - \vec{x})), \tag{2.13}$$

where $\vec{p}_i$ is the peak of the "child" source indexed by i, $\vec{x}$ and $2\vec{p}_i - \vec{x}$ are symmetric with reference to the peak $\vec{p}_i$. Then scaling parameters c_i are determined by fitting the templates to the whole footprint. The final deblended 'child' source is given by

$$f_i^D(\vec{x}) = \frac{c_i T_i(\vec{x})}{\sum_j c_j T_j(\vec{x})} f(\vec{x})\,.$$

When measuring the properties of each source, the HSC pipeline replaces the footprints of other sources with uncorrelated white noise. Shape of every source object is measured after the noise replacement.

The source properties measurement includes galaxy star classification, centroid, flux estimation, size estimation and shape estimation, which will be introduced in the following parts of this subsection.

2.3.1.3 Centroid

The HSC pipeline adopts an approximate maximum-likelihood algorithm first developed for the SDSS Photo Pipeline (Lupton et al., 2001). Under the circumstance that the noise variance is dominated by the background photon noise, the maximum-likelihood estimate of the position of a star is the peak of the image smoothed by the PSF image. The pipeline uses parabolic interpolation in this smoothed image to find the position of peak of the likelihood. If the object is significantly larger than the smoothing filter, the HSC pipeline bins the original image and re-smooth, and

the re-smoothing is repeated until the effective smoothing scale roughly matches the object size.

2.3.1.4 Shape and size

The HSC pipeline uses the `GalSim` (an open source package for galaxy image simulation and measurements) implementation of the Re-Gaussianization (`reGauss`; Hirata & Seljak (2003)) algorithm, which is a moments based method including PSF correction (with assumptions on galaxy morphology). `reGauss` has been developed and used extensively using data from the Sloan Digital Sky Survey (SDSS; Mandelbaum et al., 2005, 2013). `reGauss` estimator provides galaxy shape estimation by measuring the ellipticity that is given by

$$(e_1, e_2) = \frac{1-(b/a)^2}{1+(b/a)^2}(\cos 2\phi, \sin 2\phi), \tag{2.14}$$

where b/a is the axis ratio, and ϕ is the position angle of the major axis with respect to sky coordinates – with north being $+y$ and east being $+x$.

The `reGauss` algorithm also measures the resolution factor R_2 that is defined with the trace of the second moments of the PSF ($T_{\rm PSF}$) and those of the observed galaxy image ($T_{\rm gal}$) as

$$R_2 = 1 - \frac{T_{\rm PSF}}{T_{\rm gal}}, \tag{2.15}$$

is another important output. It is used to quantify how well the galaxy is resolved compared to the PSF.

2.3.1.5 Flux

The HSC pipeline provides a group of flux estimations with different algorithms. Here I introduce a few most important flux estimations and refer readers to Bosch et al. (2018) for more detailed descriptions on all the flux estimation algorithms.

- **PSF flux:** The HSC pipeline uses a matched-filter estimation of PSF flux (see Equation (28) of Bosch et al. (2018)—it multiplies the source with a l^2-normalized PSF model centered at the source's centroid to estimate the PSF flux. Lanczos interpolation is applied to shift the image of PSF model to the centroid of the source.

- **Aperture flux:** The HSC pipeline measures several aperture fluxes with different radii ranging from 1–23 arcsec in diameter in logarithmically-spaced sequence. For small radii, the aperture fluxes are integrals, not simple sums—the

method of Bickerton & Lupton (2013) is applied to exactly integrate over sub-pixel regions.

- **cModel flux:** The HSC pipeline measures the cModel flux (Lupton et al., 2001) by fitting multiple PSF-convolved galaxy models in a sequence designed to approximate a bulge-disk decomposition or Sersic model (Sérsic, 1963) fit.

2.3.2 From single exposure to coadded images

The CCD images are first resampled on a common pixel grid using 3rd-order Lanczos interpolation, and the coadded images are generated as a weighted average of the resampled CCD images. The inverse of the mean variance of each input CCD images is used to set the weights to improve the SNR of the coadded images.

The PSF model are determined as a function of position on focal plane for each exposure at the CCD image level by interpolating star images. The effective PSF on coadded images are reconstructed as follows: For the coadded image data, we store the combination weights, WCS transforms, PSF models, and boundaries of the input CCD images contributing to the pixel. When an image of the effective PSF model on coadds is requested at a position on the coadded image, the pipeline transforms the point to the coordinate system of each input CCDs contributing to the coadd at position of source on coadds, evaluates their PSF models at the point, resample the PSF models to the common grid, and finally combine them with appropriate weights to generate an image of the effective coadd PSF. The PSF model is cached at a single point so that repeated revaluation does not need additional computation.

2.3.3 Background subtraction

The pipeline estimate and subtract background after the source detection procedure at both the CCD image level and the coadded image level. First, the pipeline divide image into several bins, average over pixels in bins ignoring any pixels belonging to detected objects, and the variance is also computed in each bin. Then the pipeline fits a 6th-order 2D Chebyshev polynomial to the average pixel values over the image, using the average position of the non-masked pixels as the center of a bin. Each bin is weighted by the inverse variance to ensure that the heavily-masked bins do not heavily influence the fitting.

At the single exposure level, the pipeline performs a global joint estimation of the background using all the CCDs across the focal plane with a 4k $\times$ 4k pixel-mesh (namely, $11' \times 11'$). The pipeline performs a 128×128 (local) pixel-mesh (namely,

$\sim 22\,\mathrm{arcsec} \times 22\,\mathrm{arcsec}$) is applied on coadds. Readers can refer to Aihara et al. (2019) for more details.

2.4 Galaxy Image Simulations

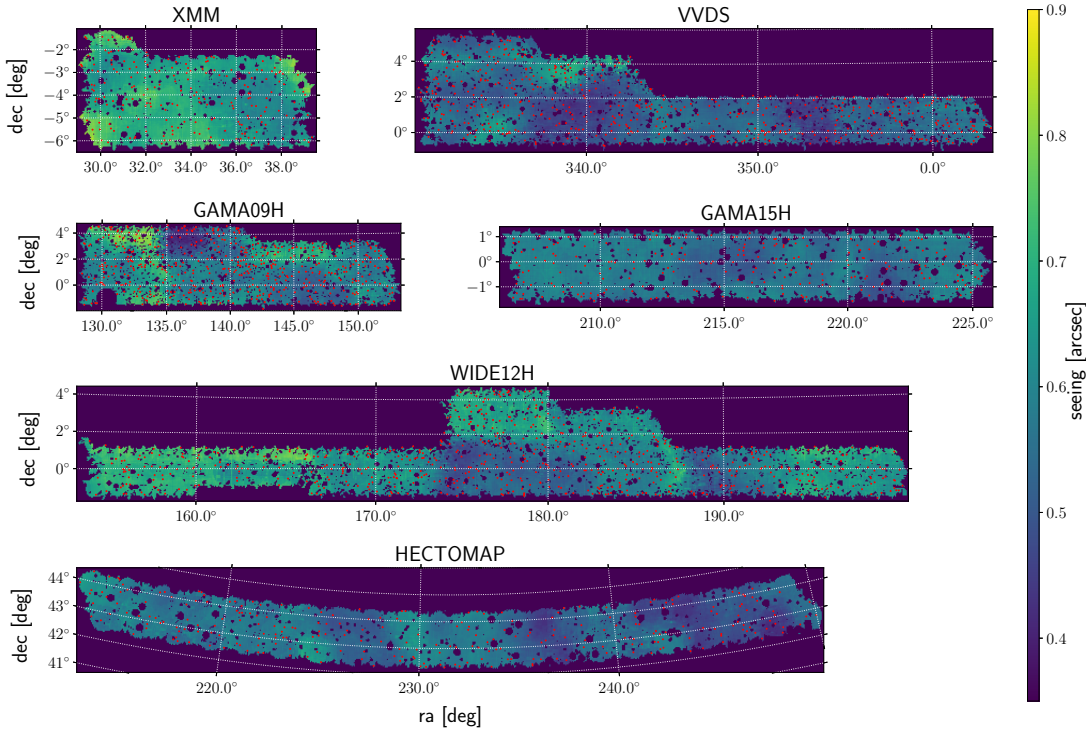

FIGURE 2.6: Map of the i-band PSF FWHM across each field. The red dots are the sampling positions for PSFs and noise properties that will be used in the HSC-like image simulation in Section 2.4. The mean seeing over all of the fields is 0.″59. The circular region centered near (RA=130.43°, DEC=−1.02°) of the GAMA09H field is masked out due to the tracking error on the exposure visit 104934 .

This section serves to introduce the galaxy image simulations that are used to test shear measurements for the three-year HSC weak lensing science. Calibration on the shear estimation is conducted is biases are discovered. The work flow of the shear calibration is summarized in Figure 2.5.

The galaxy image simulations are divided into 2500 subfields; each subfield contains 10^4 postage stamps; each postage stamp is composed of 64×64 pixels. The pixel scale is set to 0.168 arcsec to match the HSC pixel scale.

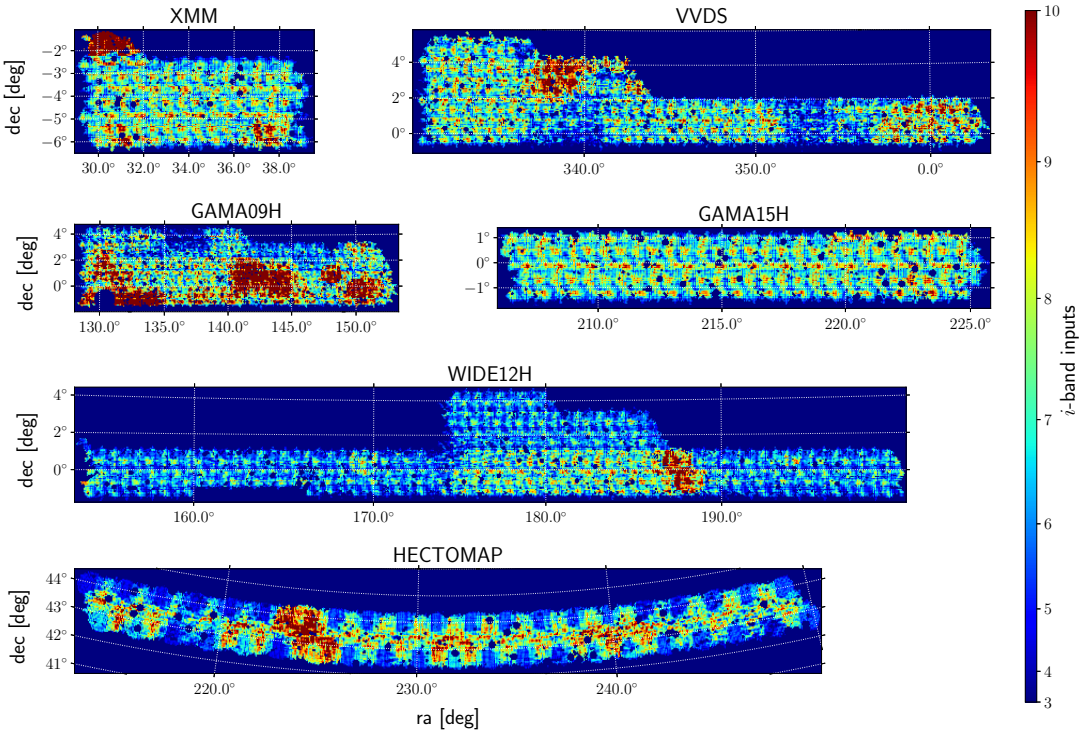

FIGURE 2.7: Number of input visits contributing to the coadded images in the i-band across each field. The mean number of input visits is 6.95 over all of the fields. The way the visits are tiled across each visit area results in the repeated pattern of overlap regions with more than the typical input number (for the tiling strategy, see Aihara et al., 2018a).

2.4.1 Input noise and PSF

The noise properties, including variance and spatial correlations, and PSF models are sampled from a set of random positions on the HSC coadded images as demonstrated as red points in Figure 2.6. Those quantities are the same in each subfield while they vary between different subfields.

The fifth-order Lanczos kernel used to warp single exposures during the coadding process (Bosch et al., 2018) results in correlated noise on coadded images. The noise correlations are sampled from the blank pixels near the random sampling positions (red dots in Figure 2.6). As the sampled noise correlations are noisy on the individual level, I randomly divide them into eight groups, and stack the correlations in each group to create eight different noise correlation functions with high signal-to-noise ratio (SNR).

The measured noise variance from blank pixels are in general greater than the input noise variance due to the neighboring and undetected sources. In order to mitigate the difference between the input noise variance and the measured noise variance,

I adopt a two-step process in the simulation: First, I use the sampled noise variance of each subfield as the input noise variance for the preliminary simulations. After populating galaxy images into each subfield, I measure the noise variance from blank (undetected) pixels on the preliminary simulations and record the ratio between the measured noise variance and the input noise variance for each subfield; Second, I divide the sampled noise variance by this ratio for each subfield and use the rescaled variances as the inputs of the fiducial simulations. By this rescaling, the noise variances measured from the simulations are matched to those measured from the HSC coadded images consistently. In contrast, this rescaling was not performed in the first-year HSC-like image simulations Mandelbaum et al. (2018a) that matched the input noise variances in the simulation to the measured noise variances in the S16A HSC data.

To mitigate the differences between the observational conditions for the simulations and the HSC data due to the finite noise and PSF sampling, I reweight each subfield in the simulations to make sure the seeing and noise variance histograms match the real data well. Note that the simulations are not reweighted according to any properties of the input galaxies. In addition, the three-year HSC shear catalog is divided into six fields (i.e., XMM, GAMA09H, WIDE12H, GAMA15H, VVDS, HECTOMAP), and the reweighting is conducted separately for each field. The seeing (PSF FWHM) histograms and noise variance histograms for the observations and the simulations are demonstrated in Figs. 2.8 and 2.9, respectively.

2.4.2 Input galaxy

I use the galaxy training sample created by Mandelbaum et al. (2018a) as input galaxies. Mandelbaum et al. (2018a) select galaxies with cModel magnitudes less than 25.2 in the COSMOS region from the HSC Wide-depth catalogs detected from three stacks (i.e., with typical seeings of $0\farcs5$, $0\farcs7$, and $1\farcs0$) of the HSC Deep/Ultra-deep images (Aihara et al., 2018b). After that, the centroids of these galaxies are determined on the images of the COSMOS HST Advanced Camera for Surveys (ACS) field (Koekemoer et al., 2007) in the F814W band. Postage stamps centered at the galaxy centroids are subsequently cut-out from the HST images. I use the training sample selected from the stack with the best seeing ($0\farcs5$) as it should be the most complete sample among the three thanks to the best seeing.

`GalSim` (Rowe et al., 2015), an open-source package for galaxy image simulations, is used to simulate HSC-like images with the COSMOS HST training images. The original HST PSF is deconvolved from each input HST postage stamp and then the image is rotated with a random angle, sheared by a known input shear distortion,

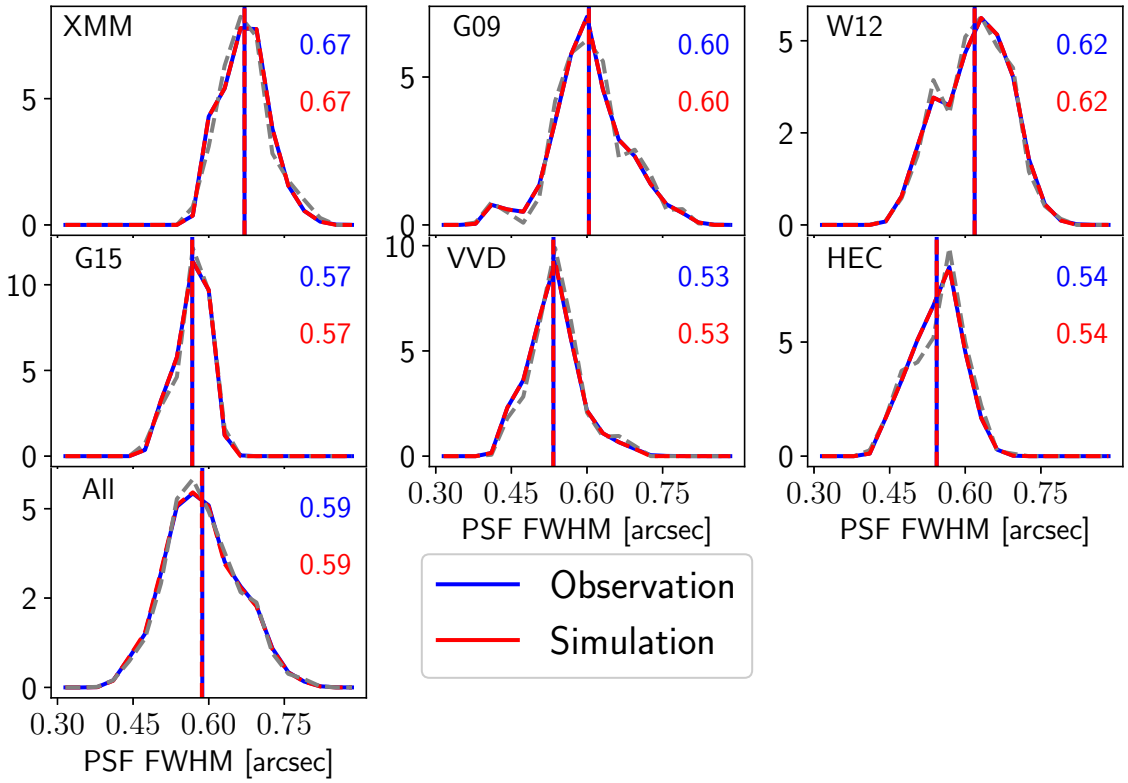

FIGURE 2.8: The first 6 panels show the normalized number histograms of PSF FWHM for the galaxies in 6 HSC fields. The last panel is the histogram for galaxies in all fields. The blue solid (red dashed) lines are for the HSC data (simulation). The blue (red) text and vertical lines indicate the mean averages of the HSC data (simulation).

convolved with an HSC PSF, sampled at the HSC pixel scale, and downgraded to an HSC noise level. The noises and PSFs used in the simulations are those sampled from the positions of the red dots in Figure 2.6. For illustration purposes, one input HST postage stamp and the corresponding simulated HSC postage stamp is shown in Figure 2.10.

In the simulations, each subfield includes 90° rotated (galaxies are intrinsically orthogonal to each other) galaxy pairs that will be used to nearly cancel out shape noise (Massey et al., 2007). By keeping track of the object ids of each orthogonal pairs, the analysis framework provides options to apply this cancellation or not. In the following analyses, the orthogonal pairs will also be used to estimate shape estimation error due to photon noise, weight bias, and selection bias in the shear estimation.

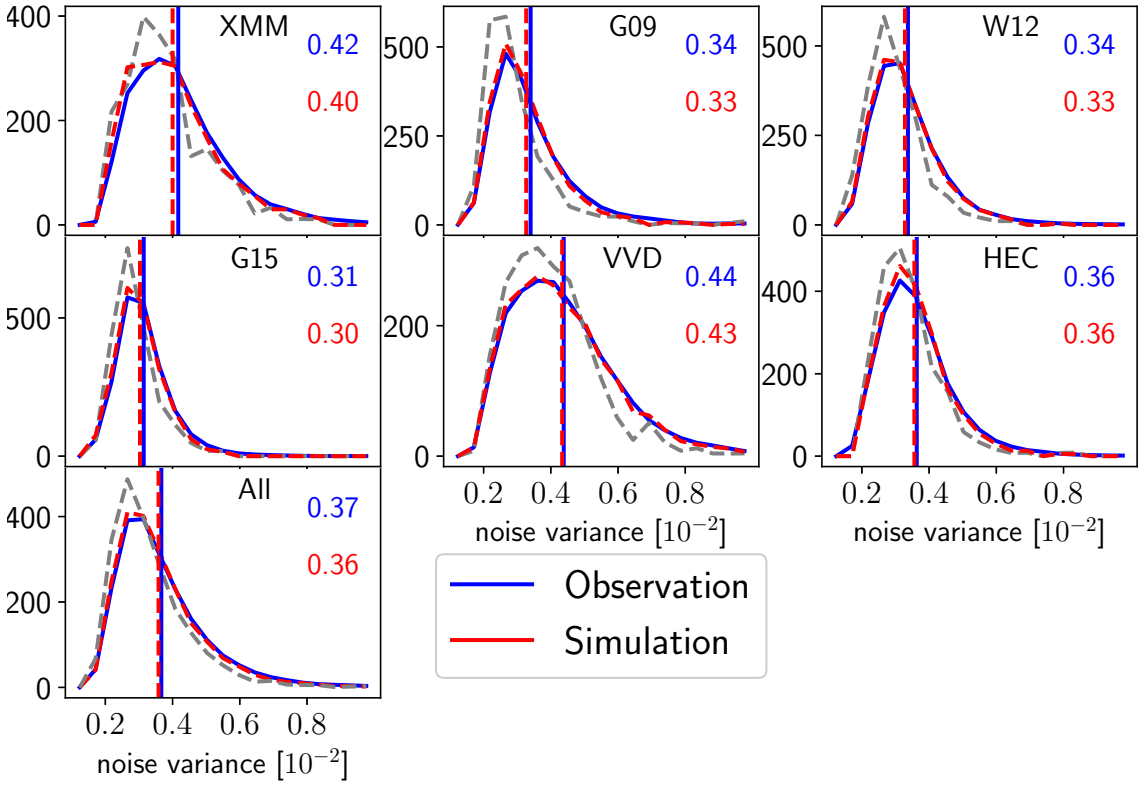

FIGURE 2.9: Same as Figure 2.8, but for noise variance.

2.4.3 Weak lensing galaxy sample

2.4.3.1 Galaxy selection

`hscPipe` v7, the pipeline used to process the HSC S19A data with the same configurations, is run on the simulations for source detection, deblending, and basic measurements (e.g, size, flux, and shape measurements).

For the analyses that will be conducted in the following context based on the image simulations, a basic set of flag cuts shown in the "Basic flag cuts" section of Table 2.1 are first imposed. Note that only the following flags actually influence the source selection in the simulations – `i_detect_isprimary`, `i_sdsscentroid_flag`, and `i_extendedness_value`. This is because the simulations do not include image artifacts (e.g., cosmic rays, bad pixels). Following Mandelbaum et al. (2018a), only the detected source nearest to the postage stamp center for each postage stamp is kept in the weak lensing catalog. Additionally, It is required that the nearest source should have a centroid that is at most 5 pixels away from the postage stamp center in order to eliminate stamps where the detection nearest to the center was not the

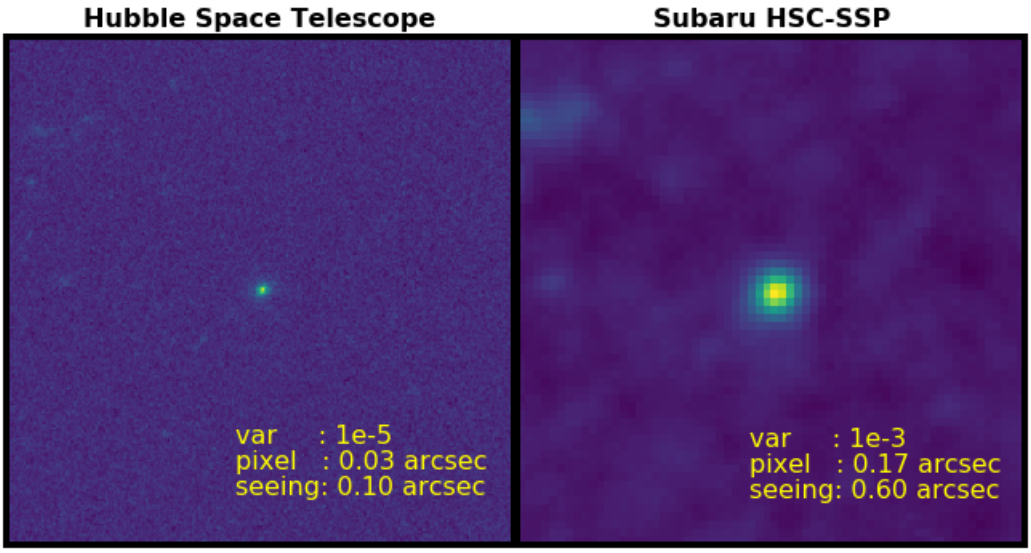

FIGURE 2.10: The input galaxy postage stamp from HST F814W band (*left panel*) is transformed to the HSC-SSP postage stamp (*right panel*). The yellow texts show the normalized noise variance, pixel scale and PSF FWHM for HST and HST.

intended central object.

Since the input HST training sample is limited by an i-band magnitude of ~ 25.2, the image simulations built upon the training sample are not complete, especially at the faint end. In addition, the simulations do not include realistic large-scale background light, while background light residuals are likely to influence the galaxy measurements of galaxy properties, especially on faint galaxies. The background residuals can also lead to fake detections that cannot be reproduced in the simulations. To mitigate the influences of the incompleteness of the training sample and the absence of realistic sky background residuals in the simulations, a set of cuts on galaxy properties measured with the pipeline are applied in both the simulations and the HSC S19A data to select a well-resolved, high-SNR galaxy sample for the weak lensing science. Furthermore, this weak lensing cuts are useful to remove fake detections that dilute the measurement. The i-band cuts, applied to both the observations and the simulations, are summarized in Table 2.1.

The `i_extendedness_value` cut is used to eliminate stellar contamination in the weak lensing galaxy catalog. The stellar contamination fraction, the number fraction of misclassified stars in the weak lensing galaxy sample even after this cut, is estimated using as a reference the galaxy-star classification performed on HST COSMOS data by Leauthaud et al. (2007). Since the HST images have a lower noise level and higher resolution than the HSC images, the HST galaxy-star separation is regarded as the ground truth.

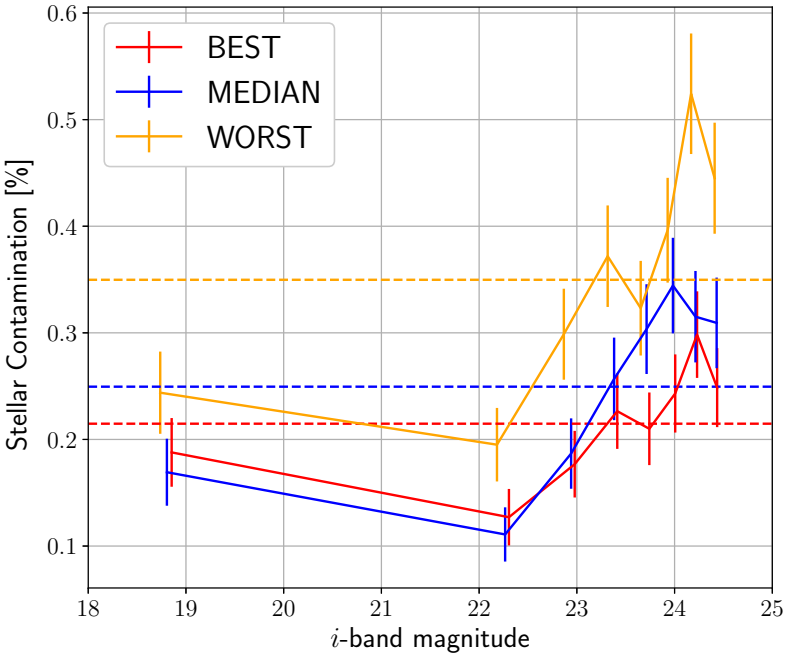

FIGURE 2.11: The stellar contamination fraction due to the incorrect classification by `hscPipe` v7, estimated after application of the weak lensing cuts in Table 2.1. Solid lines show the stellar contamination fraction as a function of i-band cModel magnitude for three different seeing conditions (i.e., BEST, MEDIAN, and WORST) estimated with reference to COSMOS HST star-galaxy classifications used as an estimate of ground truth. Errorbars show the Poisson uncertainties. Dashed lines show the stellar contamination fractions for all magnitude bins in the corresponding seeing samples.

Figure 2.11 demonstrates the stellar contamination fractions as a function of magnitude for the catalogs selected using the weak lensing cuts in the COSMOS region on the Deep/Ultradeep data consisting of multiple exposures in the COSMOS region. Three different Wide-depth stacks of the HSC S19A images have been constructed, which correspond to the exposures with the best (0.″5), median (0.″7), and worst (1.″0) seeing size (Aihara et al., 2018b). As shown, even in the worst seeing conditions, the stellar contamination fraction is below 0.2% for galaxies with i-band magnitudes brighter than 22, increasing to 0.5% at the faintest end of the shear catalog with i-band magnitudes close to 24.5. In conclusion, as the fraction of misclassified stars is less than 0.5%, the shear estimation biases from the misclassification of stars as galaxies is negligible.

In order to ensure that there are enough color information to compute photo-z, a multi-band detection cut is also imposed. The multi-band cut requires at least two other bands (out of $grzy$-bands) to have at least a 5σ cModel detection significance, which is laid out in Table 2.2. The multi-band detection cut is applied only on the

HSC S19A data but not on the simulations due to the lack of multi-band image simulations. This multi-band detection cut removes a very small fraction ($< 1\%$) of galaxies passing other selection thresholds. Therefore, the influence of the multi-band detection cut on the shear measurement is expected to be negligible.

Note, when simply imposing the HSC first-year i-band cuts shown in Table 4 of Mandelbaum et al. (2018b) a mismatch in the SNR-R_2 2D histograms between the S19A HSC data and the simulations at the faint end is found. Specifically, there are more extended faint detections that are very likely to be fake detections in the HSC S19A data than in the simulations. Compared to the S16A data, the S19A data is processed with a "global-local" background subtraction scheme, which results in an under-subtraction of sky background. It is found that this background under-subtraction increases the cModel flux estimation near bright objects, which makes cuts on cModel flux inefficient at removing the galaxies beyond the HST magnitude limit and the fake detections from background light residuals in the observations. In order to remove the aforementioned detections that cannot be reproduced in the simulations, an additional cut on the i-band 1 arcsec-diameter-aperture magnitudes (mag_A) at 25.5 is imposed to define the weak lensing sample. This aperture magnitude cut removes 3.9% galaxies that pass the other selection cuts. Section 2.5.8 quantifies the selection bias due to the cuts.

TABLE 2.1: Weak lensing cuts: The i-band selection criteria that are applied to both the simulations and the HSC data.

Cut	Meaning
Basic flag cuts	
`i_detect_isprimary` == True	Identify unique detections only
`i_deblend_skipped` == False	Deblender skipped this group of objects
`i_sdsscentroid_flag` == False	Centroid measurement failed
`i_pixelflags_edge` == False	Object too close to image boundary for reliable measurements
`i_pixelflags_interpolatedcenter` == False	A pixel flagged as interpolated is close to object center
`i_pixelflags_saturatedcenter` == False	A pixel flagged as saturated is close to object center
`i_pixelflags_crcenter`== False	A pixel flagged as a cosmic ray hit is close to object center
`i_pixelflags_bad`== False	A pixel flagged as otherwise bad is close to object center
`i_pixelflags_suspectcenter` == False	A pixel flagged as near saturation is close to object center
`i_pixelflags_clipped` == False	Source footprint includes clipped pixels
`i_hsmshaperegauss_flag` == False	Error code returned by shape measurement code
`i_hsmshaperegauss_sigma` $!=$ NaN	Shape measurement uncertainty should not be NaN
`i_extendedness_value` $!= 0$	Extended object
Galaxy property cuts	
`i_cmodel_flux`/`i_cmodel_fluxerr` ≥ 10	Galaxy has high enough SNR in i band
`i_hsmshaperegauss_resolution` ≥ 0.3	Galaxy is sufficiently resolved
$(\texttt{i\_hsmshaperegauss\_e1}^2+\texttt{i\_hsmshaperegauss\_e2}^2)^{1/2} < 2$	Total distortion cut
$0 \leq$`i_hsmshaperegauss_sigma` ≤ 0.4	Estimated shape measurement error is reasonable
`i_cmodel_mag` $-$ `a_i` ≤ 24.5	cModel Magnitude cut
`i_apertureflux_10_mag` ≤ 25.5	Aperture (1 arcsec diameter) magnitude cut
`i_blendedness_abs` $< 10^{-0.38}$	Avoid spurious detections and those contaminated by blends

TABLE 2.2: Weak lensing cuts: The multi-band detection cut applied to the HSC data.

Require that at least two of the following four cuts be passed (not all)	
Cut	Meaning
`g_cmodel_flux/g_cmodel_fluxerr` ≥ 5	Galaxy has high enough SNR in g band
`r_cmodel_flux/r_cmodel_fluxerr` ≥ 5	Galaxy has high enough SNR in r band
`z_cmodel_flux/z_cmodel_fluxerr` ≥ 5	Galaxy has high enough SNR in z band
`y_cmodel_flux/y_cmodel_fluxerr` ≥ 5	Galaxy has high enough SNR in y band

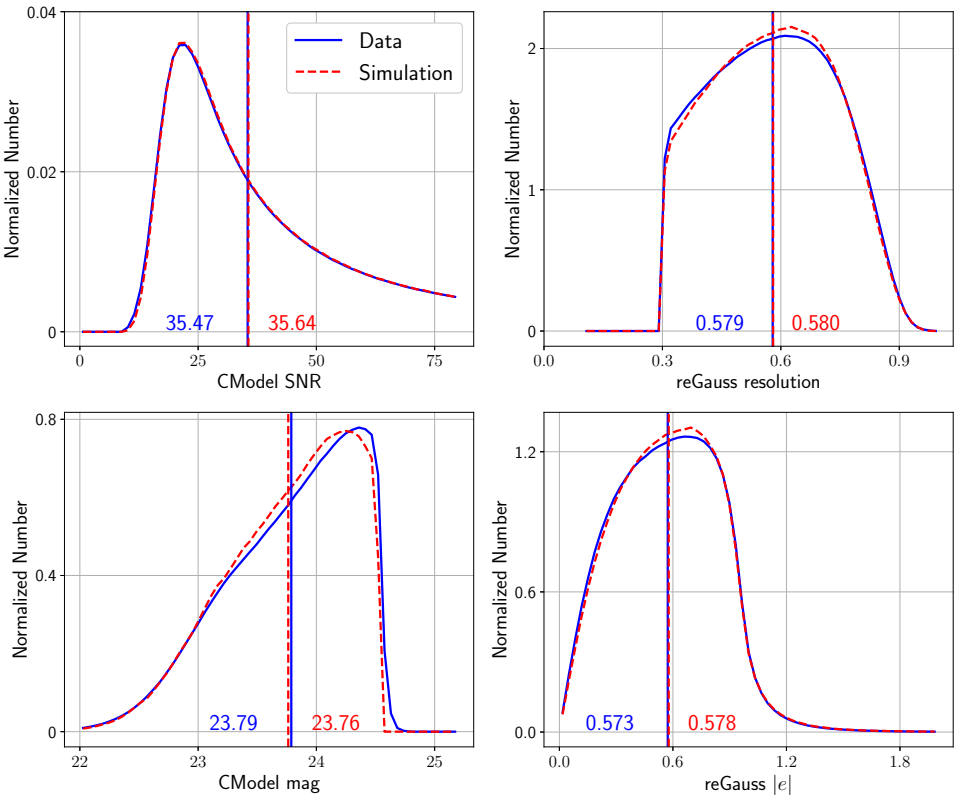

FIGURE 2.12: The normalized number histograms of i-band properties, which include cModel SNR (upper-left), `reGauss` resolution (upper-right), cModel magnitude (lower-left), and `reGauss` distortion magnitude (lower-right), for galaxies in all fields combined. The blue solid (red dashed) lines are for the HSC data (simulation). The blue (red) text and vertical lines indicate the mean averages of the HSC data (simulation).

In order to study the influence of the selection property of source detector of `hscPipe` v7 on the galaxy sample, one detection – with its peak at the center of the stamp – is artificially inserted if no object is detected within 5 pixels from the center of a simulated postage stamp. Flux, size and shape measurements are subsequently

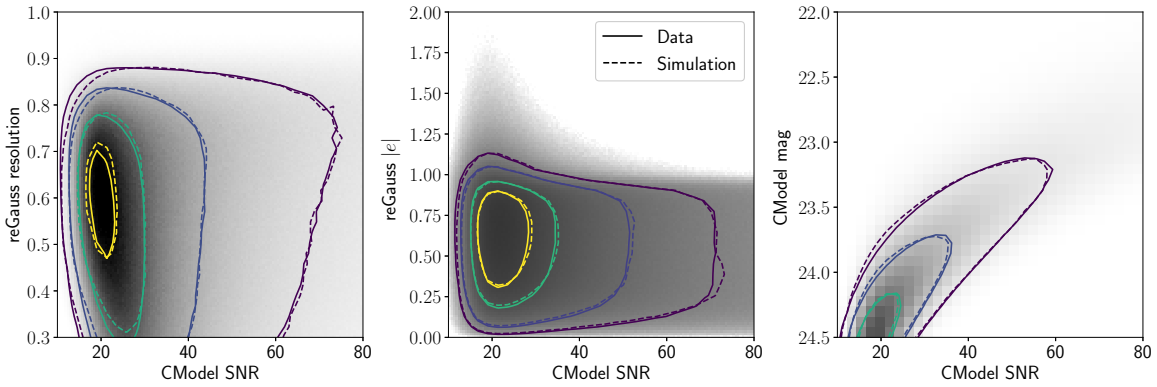

FIGURE 2.13: The 2D histograms for the HSC data and the simulations. The panels from left to right show the (SNR, R_2), (SNR, $|e|$) and (SNR, cModel magnitude) histograms, respectively. The solid (dashed) lines show the contours for the HSC data (simulation) and the color maps are the 2D histograms for the HSC data. The color maps are the 2D histograms for the HSC data.

conducted on the inserted detections. It is found that the number of these forced detections that enter the weak lensing sample after the weak lensing cuts are applied is far less than 0.1% of the total galaxy number in the weak lensing sample. Therefore, the selection function of the source detector has a negligible influence on the weak lensing sample, and the selection bias from the source detector is negligible. This is aligned with the expectations: Since the 5σ detection limit for point sources is 26.2 mag in i-band, and the weak lensing galaxy sample is selected with an i-band magnitude cut at 24.5, far brighter than the detection limit. However, it is important to note that that several defects from real data (e.g., sky background residuals, optical ghosts, very bright stars, etc.) that can affect the object detection are not included in the simulations.

2.4.3.2 Galaxy properties

The 1D normalized number histograms for i-band galaxy properties (i.e., cModel SNR, `reGauss` resolution, cModel magnitude, `reGauss` distortion magnitude defined as $|e| = \sqrt{e_1^2 + e_2^2}$), of the HSC S19A data and the simulations are shown in Figure 2.12. When plotting the histograms, the same upper-limit on the i-band cModel SNR (SNR$<$ 80) as Mandelbaum et al. (2018a) is applied in order to compare this results with those of the HSC first-year image simulation paper. As shown, there are no significant discrepancies in the shapes of the number histograms between the HSC data and the simulations. The relative difference of the mean values averaged across all of the fields for these properties between the data and the simulations are 0.5% (cModel SNR), 0.2% (`reGauss` resolution) 0.1% (cModel mag) and 0.8% ($|e|$). The

matching is impressive that all of relative difference are less than 1%. Finally, the 2D joint histograms of these galaxy properties are demonstrated in Figure 2.13.

Compared to the first-year HSC-like image simulations (see Figure 8 of Mandelbaum et al., 2018a), the three-year HSC-like simulations presented here have a better match to the HSC galaxy properties in the SNR histogram. The average SNR over all fields was relatively less than the observed SNR by $\sim 5\%$ in Mandelbaum et al. (2018a), while the discrepancy decreases to $\sim 0.5\%$ for the for the current image simulations. The match in SNR distribution improves since the sampled noise variance is rescaled for a consistent match between the measured noise variances from the simulations and those from the real data (as was discussed in Section 2.4.1). Moreover, the matches between the 2D histograms are visually better than those of the first-year HSC simulations demonstrated in Figure 9 of (Mandelbaum et al., 2018a), which is primarily due to the improved match of the SNR histograms.

Additionally, compared to the state-of-art image simulations in other weak lensing surveys, e.g., Figure 9 in Kannawadi et al. (2019) from the KiDS survey and Figure 3 in MacCrann et al. (2020) from the DES survey, the simulations generally have better matches to the histograms of the observed galaxy properties (i.e., galaxy brightness, size and shape)

2.5 Calibration

I first introduce a classic shear estimator and calibrate the intrinsic shape measurement. Then I use the image simulations introduced in Section 2.4 to estimate, model, and then remove the shear calibration bias. The selection bias in the shear estimation is left to be discussed in Section 2.5.8.

2.5.1 `reGauss` Shear Estimator

Re-Gaussianization (`reGauss`), a moments based method including PSF correction (with assumptions on galaxy morphology), has been developed and used extensively using data from the Sloan Digital Sky Survey (SDSS; Mandelbaum et al., 2005, 2013). The outputs of the `reGauss` estimator are the galaxy ellipticity

$$(e_1, e_2) = \frac{1-(b/a)^2}{1+(b/a)^2}(\cos 2\phi, \sin 2\phi), \tag{2.16}$$

where b/a is the axis ratio, and ϕ is the position angle of the major axis with respect to sky coordinates – with north being $+y$ and east being $+x$.

For a group of galaxies that are distorted by a constant lensing shear, the lensing shear can be estimated with a weighted average of the ellipticity of all galaxies as

$$\hat{g}_\alpha = \frac{1}{2\mathcal{R}} \langle e_\alpha \rangle \,, \tag{2.17}$$

where the shear response, denoted as $\mathcal{R}$, is the response of the weighted mean ellipticity to a small shear distortion (Kaiser et al., 1995; Bernstein & Jarvis, 2002); $\alpha = 1, 2$ are the indices for the two components of the ellipticity; w is the galaxy shape (inverse variance) weights to be used to calculate the derive average, which is defined as

$$w = \frac{1}{\sigma_e^2 + e_{\rm RMS}^2}, \tag{2.18}$$

where σ_e and $e_{\rm RMS}$ are the per-component root-mean-squares (`RMSs`) of the shape estimation error (due to the sky variance) and of the galaxy intrinsic shape, respectively. σ_e and $e_{\rm RMS}$ are modeled and estimated for each galaxy using image simulations, as will be shown in Section 2.5.2. The response for the source galaxy population is given by

$$\mathcal{R} = 1 - \frac{\sum_i w_i e_{{\rm RMS};i}^2}{\sum_i w_i}, \tag{2.19}$$

where i is the index of galaxies.

The response for PSFs is approximately one since the PSFs are nearly round. Based on this approximation, shear distortion for a PSF image is defined as $g_{{\rm PSF},\alpha} = e_{{\rm PSF},\alpha}/2$, where $e_{{\rm PSF},\alpha}$ are the two components ($\alpha = 1, 2$) of PSF ellipticity defined with the second moments of the PSF measured by `reGauss`.

It is known that the `reGauss` algorithm is subject to certain forms of shear estimation bias (e.g., model bias, noise bias, selection bias etc.), and the calibrated form of the `reGauss` shear estimator for a galaxy ensemble is given by

$$\hat{g}_\alpha = \frac{\sum_i w_i e_{\alpha;i}}{2\mathcal{R}(1+\hat{m})\sum_i w_i} - \frac{\hat{c}_\alpha}{1+\hat{m}}, \tag{2.20}$$

where the multiplicative bias and fractional additive bias (defined in Equation (2.1)) for galaxy with index i are denoted as m_i and a_i, respectively, the multiplicative bias and the additive bias for the galaxy ensemble are

$$\begin{aligned} \hat{m} &= \frac{\sum_i w_i m_i}{\sum_i w_i}, \\ \hat{c}_\alpha &= \frac{\sum_i w_i a_i e_{{\rm PSF},\alpha;i}}{\sum_i w_i}, \end{aligned} \tag{2.21}$$

respectively.

The estimation, modelling and calibration of the shear estimation biases as a function of galaxy properties (i.e., SNR, R_2, and galaxy photometric redshift) are shown in Sections 2.5.3–2.5.8.

2.5.2 Shape measurement errors and intrinsic shape dispersion

This section estimates and model the statistical uncertainties from the sky variance (namely, shape measurement error) and intrinsic shape noise (namely, intrinsic shape dispersion) as functions of galaxy properties, respectively. Based on the estimated uncertainties, the optimal (inverse variance) weight for the shear estimation is subsequently determined.

First, the galaxy image simulations are used to estimate the 1σ per-component shape uncertainty due to photon noise (σ_e) and model it as a function of galaxy properties (i.e., SNR and R_2) following the formalism given in Appendix A of Mandelbaum et al. (2018a). The estimation uses the orthogonal (90°-rotated) galaxy pairs to nearly eliminate shape noise and measure the statistical error due to the sky variance. A sliding window in the 2D SNR-R_2 plane is defined with an equal-number binning scheme and σ_e is estimated in window, the result of which is demonstrated in the left panel of Figure 2.14. A power-law of $\sigma_e(\mathrm{SNR}, R_2)$ is fitted to the estimated σ_e on individual galaxy level, which is given by

$$\sigma_e = 0.268 \left(\frac{\mathrm{SNR}}{20}\right)^{-0.942} \left(\frac{R_2}{0.5}\right)^{-0.954} . \tag{2.22}$$

The difference between the power-law and the estimation is mitigated by linearly interpolate the ratio of the estimated values to the fitted power-law as a function of $\log_{10}(\mathrm{SNR})$ and R_2 .

Using galaxies in the real HSC shear catalog, the per-component intrinsic shape dispersion (e_{RMS}) is estimated by subtracting off (in quadrature) the shape measurement error from the shape dispersion:

$$e_{\mathrm{RMS}} = \sqrt{\frac{\sum_i \left(e_{1;i}^2 + e_{2;i}^2 - 2\sigma_e^2(\mathrm{SNR}_i, R_{2;i})\right)}{2N_{\mathrm{gal}}}}, \tag{2.23}$$

where i refers to the galaxy index; N_{gal} is the total galaxy number in the galaxy ensemble. This estimation is computed in each sliding window, and the estimated intrinsic shape dispersion as a function of SNR and R_2 is demonstrated in the right panel of Figure 2.14. As shown, the shape dispersion is relatively flat with a value

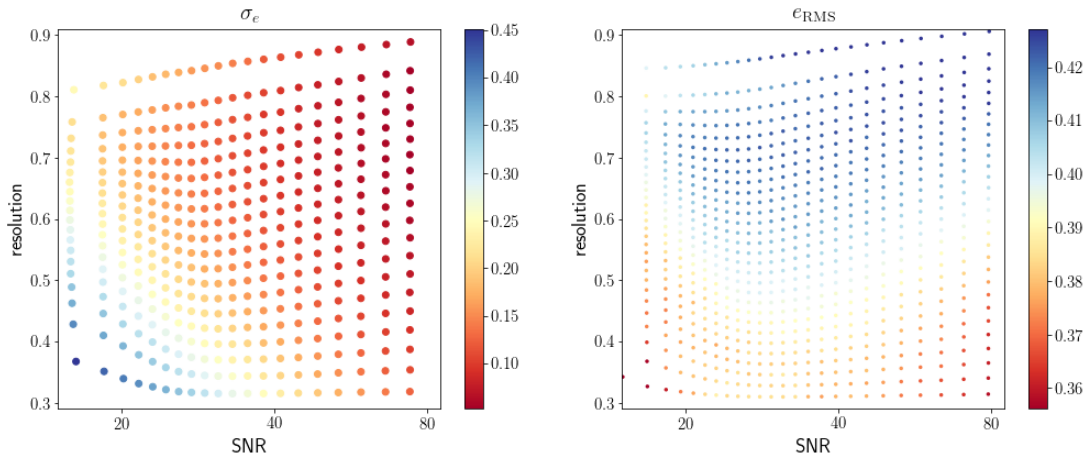

FIGURE 2.14: The *left panel* (*right panel*) shows the estimated per-component shape measurement uncertainty σ_e (intrinsic shape dispersion $e_{\rm RMS}$) estimated with the simulations in different SNR-R_2 bins.

close to 0.4. Therefore, a linear interpolation is performed in the 2D SNR-R_2 plane to model $e_{\rm RMS}$ on the individual galaxy level.

After that, the optimal shape weight (according to the inverse-variance weighting scheme) is determined with σ_e and $e_{\rm RMS}$ following Equation (2.18), and the shear response is determined following Equation (2.19).

2.5.3 Baseline calibration

In order to determine the baseline shear calibration bias in the absence of selection bias, both galaxies in each 90°-rotated pair is kept in the galaxy ensemble by imposing the weak lensing cuts on only one randomly chosen galaxy in the pair. Additionally, both galaxies in each pair are forced to use the same shape weight of the randomly chosen galaxy to avoid weight bias due to the correlation of shape weight with shear. By doing so, it is ensured that both the weighting and selection processes do not correlate with the input shear, and the bias of these correlations is calibrated in Section 2.5.4 and Section 2.5.8, respectively.

The upper-left panel of Figure 2.15 shows the baseline multiplicative bias as a function of SNR and R_2 with an equal-number binning scheme estimated from the overall simulation. An unspecified constant value is added to the multiplicative bias to blind the shear analysis. The lower-left panel shows the standard deviation of the multiplicative bias estimation in the upper-left panel as a reference. Similarly to Section 2.5.2, I fit $m(\mathrm{SNR}, R_2)$ to a power-law in both parameters (including a constant offset), and interpolate a correction to the power-law based on the ratio

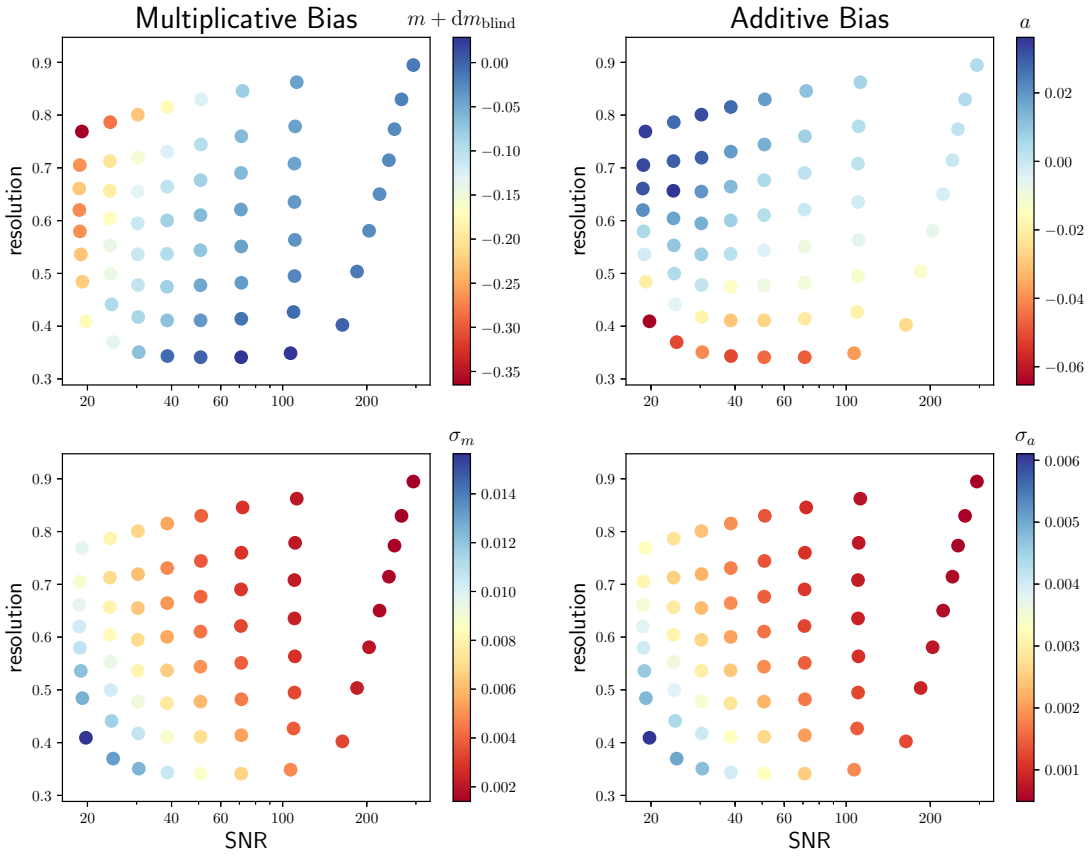

FIGURE 2.15: The left panels show the multiplicative bias (upper-left) and its standard deviation (lower-left) estimated in the SNR-R_2 plane using the image simulations. The right panels are for the fractional additive bias. Note that the multiplicative bias is blinded by adding a shift dm_{blind}.

between the multiplicative bias estimation and the power-law. The best-fit power-law is

$$m(\mathrm{SNR}, R_2) + \mathrm{const.} \propto \left(\frac{R_2}{0.5}\right)^{1.66} \left(\frac{\mathrm{SNR}}{20}\right)^{-1.24} . \tag{2.24}$$

The upper-right panel of Figure 2.15 shows the baseline fractional additive bias as a function SNR and R_2 with an equal-number binning scheme estimated from the overall simulation. The lower-right panel shows the standard deviation of the additive bias estimation in the upper-left panel as a reference. Similarly to the modelling of the baseline multiplicative bias, the estimated baseline fractional additive bias is fit to the model proposed in Mandelbaum et al. (2018a). The best-fit model is

$$a(\mathrm{SNR}, R_2) \propto (R_2 - 0.61) \left(\frac{\mathrm{SNR}}{20}\right)^{-0.94} . \tag{2.25}$$

Similarly, I interpolate a correction to the model based on the difference between the

fractional additive bias estimation and the model.

2.5.4 Weight bias

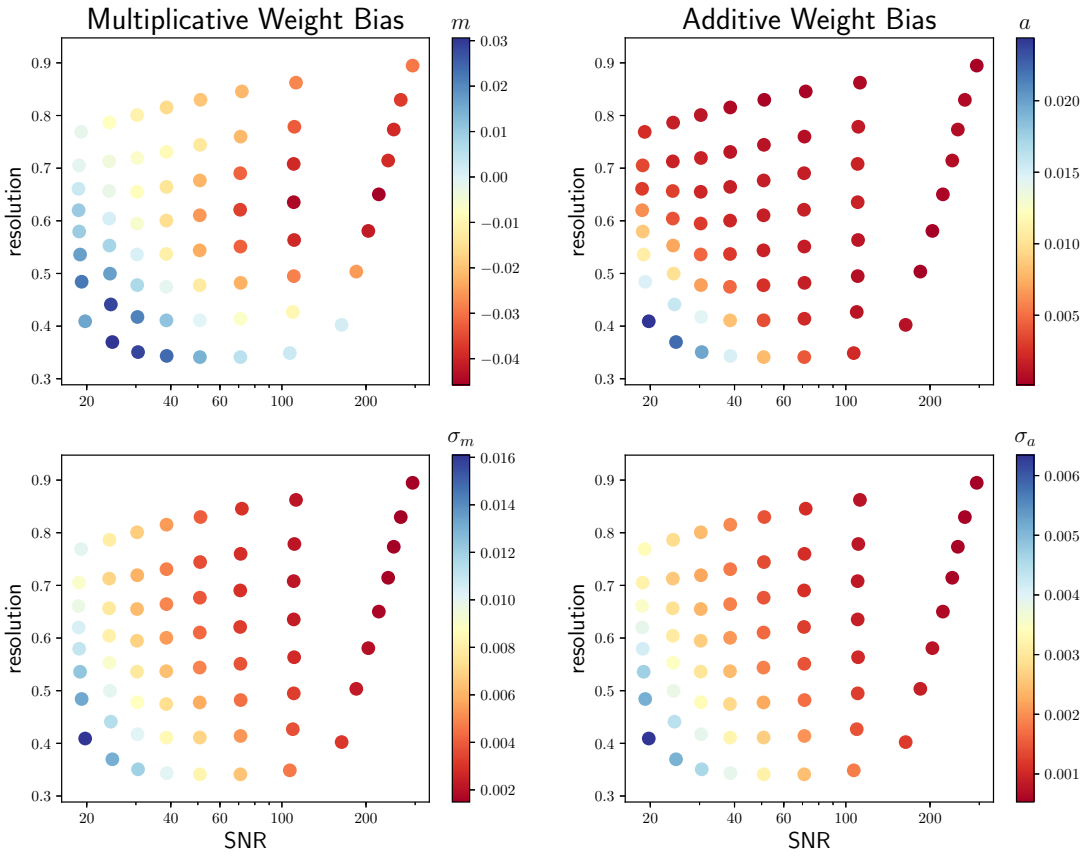

FIGURE 2.16: The left panels show the multiplicative weight bias (upper-left) and the standard deviation (lower-left) of the multiplicative bias estimated in the SNR-R_2 plane using the simulation. The right panels show the fractional additive weight bias.

Weight bias refers to the shear estimation bias caused by a correlation between the adopted shape weight and the true lensing shear, and it can also be regarded as the bias from a shear-dependent smooth selection since weighting is effectively a smooth selection (Mandelbaum et al., 2018a).

This section estimates the weight bias for the optimal weight using image simulations containing 90° rotated pairs (Mandelbaum et al., 2018a) by comparing the shear bias estimate with and without enforcing the same shape weight for each galaxy in an 90-degree rotated galaxy pair. Figure 2.16 shows the multiplicative weight bias (left panel) and the fractional additive weight bias (right panel) with a equal-number binning scheme in the 2D SNR-R_2 plane. As shown, this bias is positive and reaches

a maximum amplitude of 0.03 at low SNR and R_2, whereas it is negative and reaches a maximum amplitude of -0.045 at high SNR and R_2. A small additive weight bias with $\lesssim 5\sigma$ significance is also found, which reaches its maximum of 0.025 at low SNR and R_2, and it decreases as SNR and R_2 increase. Considering that the weight biases are dependent on the location in the 2D SNR-R_2 plane, the same process as Section 2.5.3 is used to model and interpolate the weight biases as functions SNR and R_2 .

2.5.5 Redshift dependence

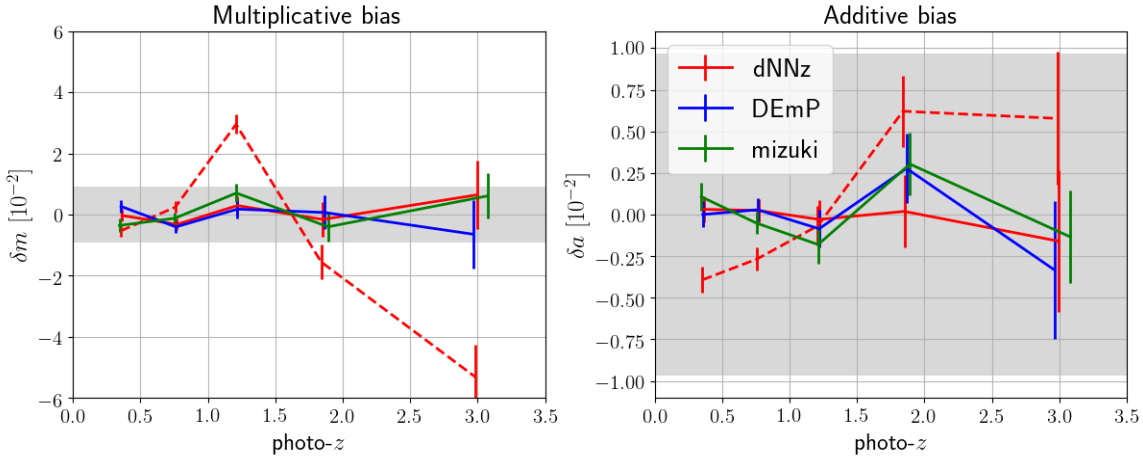

FIGURE 2.17: The left (right) panel shows the redshift-dependent multiplicative (fractional additive) bias. The red lines are for `dNNz` photo-z, the blue lines are for `DEmP` photo-z, and the green lines are for `mizuki` photo-z. The dashed lines are the results before removing the redshift-dependent bias, whereas the solid lines are the results after modelling and calibrating the redshift-dependent bias with `dNNz` photo-z. The gray regions indicate the requirements on calibration residuals defined in Section 2.2.

Since the weak lensing analyses often use photometric weights that is dependent on photo-z (see, e.g., Murata et al., 2019; Miyatake et al., 2019), or divide the galaxy sample into different photometric redshift (photo-z) bins (see, e.g., Hikage et al., 2019; Hamana et al., 2020), it is of crucial importance to quantify and calibrate the redshift-dependent shear calibration biases. Although some redshift-dependent biases are already partially accounted for in the calibrations in Sections 2.5.3 and 2.5.4, which model the calibration biases as functions of R_2 and SNR, this section looks into the remaining redshift dependence of the shear estimation biases after accounting for those effects.

Currently, there are only realistic simulations for i-band images since the input

galaxy sample are from the single-band F814W HST exposures; therefore, photo-z cannot be directly derived from the simulated images. Li et al. (2020) proposed to use the photo-z estimates of the input galaxies as a proxy of the measured redshift in the simulations to study the shear estimation biases that depend on redshift. Specifically, the input COSMOS galaxies are matched to the HSC S19A photo-z catalog (Nishizawa et al., 2020) in the Wide layer according to the angular position of the input galaxies, and each galaxy in the simulations is assigned with the estimated redshift of the matched galaxy in the HSC photo-z catalog. For cross validation, three different HSC photo-z estimates – the Deep Neural Net Photometric Redshift (`dNNz`; Nishizawa et al., in prep.), Direct Empirical Photometric code (`DEmP`; Hsieh & Yee, 2014), and Mizuki photometric redshift (`mizuki`; Tanaka, 2015), which are based on neural network, empirical polynomial fitting, and Bayesian template fitting, respectively. Here, calibration biases are estimated and removed as a function of `dNNz` photo-z. Finally, `DEmP` photo-z and `mizuki` photo-z are used for cross-validation tests.

To quantify the redshift-dependent residual of the shear estimation not captured in the calibrations of Sections 2.5.3 and 2.5.4, the simulations are divided into different `dNNz` photo-z bins following an equal-number binning scheme (with selection bias cancellation), and the multiplicative and additive bias for each bin is estimated. The estimated biases are subsequently estimated with the predicted biases using the calibration model derived in Sections 2.5.3 and 2.5.4. Here, the shape noise cancellation is adopted by using orthogonal galaxy pairs to cancel out selection bias due to galaxy cuts, whereas the shape weights are not forced to be equal in each galaxy pairs to cancel out weight bias as it has been calibrated in Section 2.5.4.

The dashed red lines in Figure 2.17 show the residuals of multiplicative bias (left panel) and additive bias (right panel) as a function of `dNNz` redshift, and the redshift-dependent biases are modelled by linearly interpolating the bias residuals across the redshift bins. The redshift-dependent multiplicative bias (left panel) has negative value of $\sim -1\%$ and positive value of $\sim 3\%$ for galaxies in the photo-z range $[0, 1]$ and $[1, 1.5]$, respectively. The redshift-dependent fractional additive bias (right panel) is within the three-year systematic error requirements even before the correction.

2.5.6 Combined estimates of calibration bias

The final multiplicative bias and additive bias estimates the galaxies in the catalog are the sum of the baseline bias modeled in Section 2.5.3, weight bias modeled in Section 2.5.4, and residual redshift-dependent bias modeled in Section 2.5.5. The outputs of the calibration are summarized in Table 2.3.

TABLE 2.3: The outputs from the analyses based on the image simulations. The first three outputs are derived to optimize the shear estimation (for precision) as shown in Section 2.5.2. The last three outputs are derived to calibrate the shear estimation (for accuracy) as shown in Section 2.5.3, Section 2.5.4, and Section 2.5.5.

Output properties	Meaning
Optimization	
`i_hsmshaperegauss_derived_sigma_e`	Measurement error from photon noise
`i_hsmshaperegauss_derived_rms_e`	Shape noise dispersion
`i_hsmshaperegauss_derived_weight`	Weak lensing shape weight
Calibration	
`i_hsmshaperegauss_derived_shear_bias_m`	Multiplicative bias
`i_hsmshaperegauss_derived_shear_bias_c1`	The first component of additive bias
`i_hsmshaperegauss_derived_shear_bias_c2`	The second component of additive bias

2.5.7 Ensemble calibration uncertainties

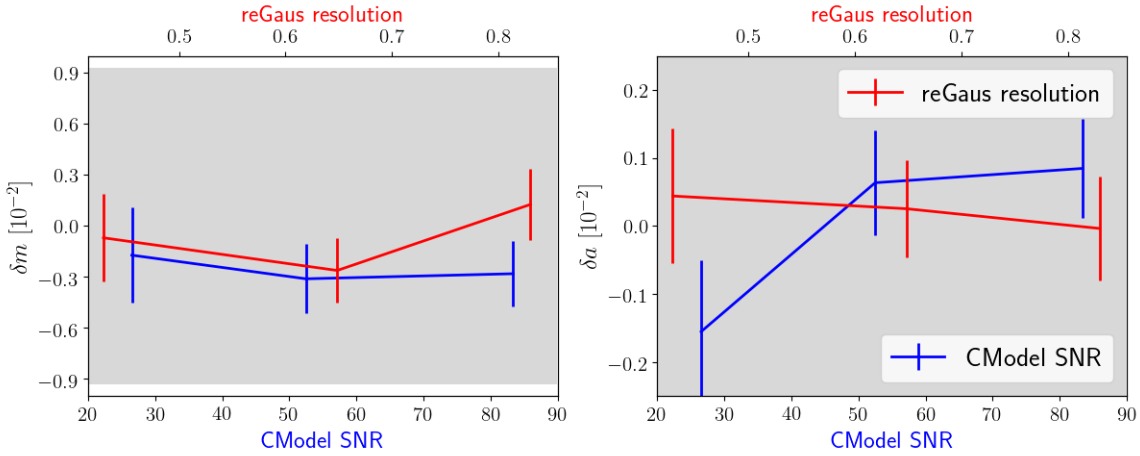

FIGURE 2.18: The calibration residuals for subsamples binned by two modeled galaxy properties (i.e., R_2 and SNR). The left (right) panel shows the multiplicative (fractional additive) bias. The red (blue) lines show the results for R_2 (SNR) binning. The gray regions indicate the requirements on calibration residuals defined in Section 2.2.

This section demonstrates the validity and robustness of the calibration of the multiplicative bias and additive bias derived in Sections 2.5.3–2.5.5, and assign a systematic uncertainty to the calibration at the ensemble level. The calibration bias residuals include multiplicative bias residuals (denoted as δm) and fractional additive bias residual (denoted as δa), which are the remaining bias after the shear calibrations. Note that the selection bias is not taken into account here, and the shape noise

cancellation is adopted by using orthogonal galaxy pairs to cancel out selection bias due to the galaxy binning.

First, the simulations are divided into several subsamples following an equal-number binning scheme by the galaxy properties, which include those used for modeling shear biases (i.e., cModel SNR, `reGauss` resolution, and `dNNz` photo-z) and those that are marginalized (not explicitly taken into account) in the shear calibration biases estimation (i.e., cModel magnitude, seeing, `DEmP` and `mizuki` photo-z). Shear is subsequently estimated for each subsample in each subfield (of 800 subfields) using the calibrated shear estimator. Finally, the bias residuals for each property-binned subsample are determined using Equation (2.1).

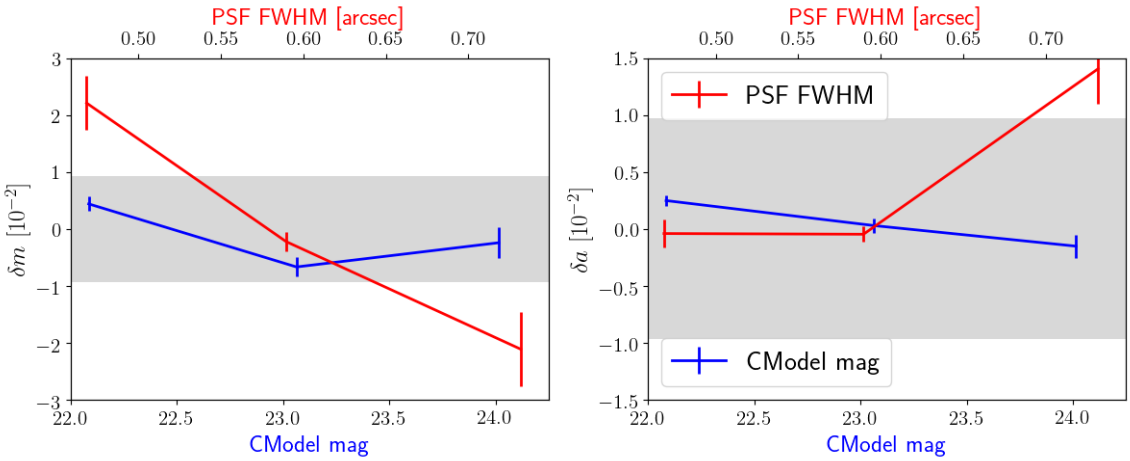

FIGURE 2.19: The dependence of calibration residuals on two marginalized galaxy properties. The left (right) panel shows the multiplicative (fractional additive) bias. The blue (red) lines show the results for cModel magnitude (seeing size). The gray regions are for the requirements on calibration residuals defined in Section 2.2.

The dependence of the bias residuals on the modelled properties are subsequently tested. The red solid lines in Figure 2.17 show the bias residuals with `dNNz` photo-z binning; Figure 2.18 shows the calibration bias residuals when binning the simulations with SNR or R_2. As shown, the amplitude of multiplicative bias residual (δm) is less than 0.5%, the fractional additive bias residual (δa) is less than defined in Section 2.2. These bias residuals are expected to be consistent with zero as expected since these galaxies properties were used to model the calibration bias calibration.

The dependence of the bias residuals on the marginalized properties are subsequently tested. Figure 2.17 demonstrates the bias residuals when binning galaxies by `DEmP` and `mizuki` photo-z; Figure 2.19 shows the bias residuals when binning the simulations with cModel magnitude and seeing size. As shown, when binning by seeing size, the amplitudes of the multiplicative bias residuals exceed the requirements

for the best and worst seeing bins, and the amplitudes of the fractional additive bias residuals exceed the requirement for the worst seeing bin. This binning corresponds to an extreme case of splitting up the survey based on regions with specific PSF FWHM. The finding, which is consistent with Mandelbaum et al. (2018a), implies that weak lensing analyses with strict region cuts should evaluate the seeing size distribution after the cuts, and then evaluate whether additional shear calibrations are required for such region cuts. Calibration bias residuals are within the requirement limits for the other aforementioned binning schemes.

2.5.8 Selection bias

Selection bias refers to the multiplicative bias or the additive bias induced by a selection that correlating with the lensing shear and/or the PSF ellipticity. The result of the anisotropic selection is that the selected galaxies, which are close enough to the edge of the cut, coherently align in a direction that is correlated with the lensing shear and/or the PSF ellipticity. Given that the amplitudes of the lensing shear and the PSF anisotropy are small, the anisotropic selection has little influence on the galaxies that are far away from the selection edge.

The selection bias is estimated by comparing the shear estimation of the overall sample with/without forcing the inclusion of 90° rotated pairs. It is found that the selection biases for other cuts on i-band galaxy properties (e.g., cModel SNR, cModel Magnitude) are consistent with zero, and the selection bias for the multi-band detection cut is negligible since the cut removes less than one percent of the galaxies from the parent sample; therefore, this section focuses on the selection bias due to the resolution and aperture magnitude cuts. The upper panels of Figure 2.20 show the estimated selection biases for the resolution cut ($R_2 > 0.3$) and the aperture magnitude cut ($\mathrm{mag}_A < 25.5$) in Table 2.1, respectively, while changing the upper (lower) limit of resolution (aperture magnitude) to change the galaxy ensemble.

As shown, the multiplicative bias for the resolution (magnitude) cut is constantly positive (negative), whereas the fractional additive bias for the resolution cut is constantly positive. The fractional additive bias for the aperture magnitude cut is consistent with zero within 2σ and is within the three-year HSC science requirement. The magnitude of the biases decrease when the sizes of the corresponding galaxy ensembles increase since the fractions (the number of which do not change) of the galaxies that are close enough to the selection edges and influenced by the anisotropic selections decrease.

The method proposed by Mandelbaum et al. (2018a) is adopted to empirically estimate and remove the selection bias for any galaxy sample due to the two afore-

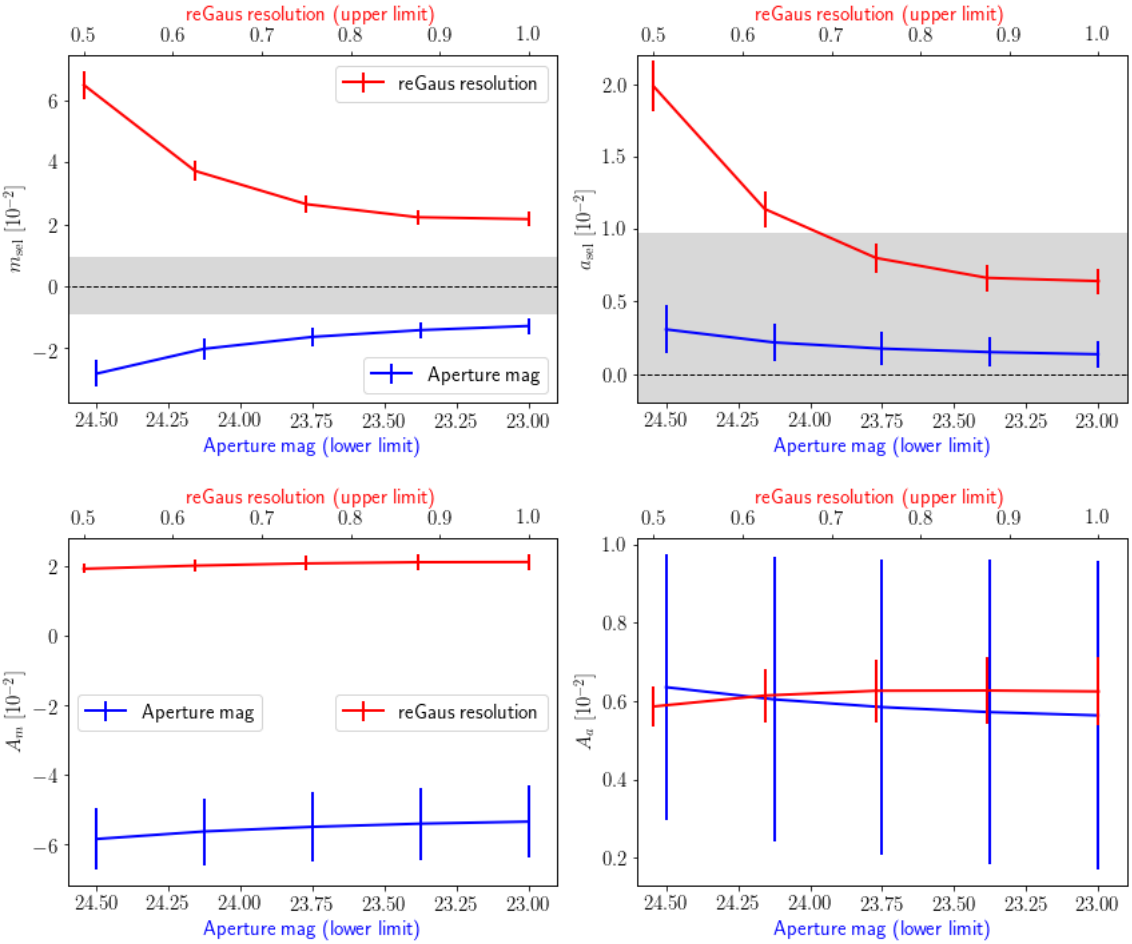

FIGURE 2.20: The upper-left (upper-right) panel shows the multiplicative (fractional additive) bias due to cuts on resolution (R_2) and aperture magnitude (mag_A). The gray regions indicate the requirements on calibration residuals defined in Section 2.2, and the horizontal dashed lines are $y = 0$. The lower-left (lower-right) panel shows the multiplicative (fractional additive) bias ratio of the cuts on resolution (R_2) and aperture magnitude (mag_A). For resolution (aperture magnitude), the lower (upper) limit is fixed while changing the upper (lower) limit. For each selection cut, errorbars are correlated between the points since at least a fraction of the same simulated galaxies are used for the calculations.

mentioned cuts. The premise is that, for a galaxy sample, the ratio between the selection biases, from a cut on galaxy observable (X), versus the marginal galaxy number density at the edge of the cut ($P(X)\,|_{\rm edge}$) is approximately constant. The ratios are referred to as selection bias ratios and defined as

$$\begin{aligned} A_m(X) &= \frac{m_{\rm sel}\,(X)}{P\,(X)\,|_{\rm edge}}, \\ A_a(X) &= \frac{a_{\rm sel}\,(X)}{P\,(X)\,|_{\rm edge}}. \end{aligned} \tag{2.26}$$

The lower panels of Figure 2.20 demonstrate the selection bias ratios for R_2 and mag_A. Here, the lower limit of resolution is fixed at $R_2 = 0.3$ and the upper limit of aperture magnitude is fixed at $\mathrm{mag}_A = 25.5$, respectively, and the upper limit of R_2 and the lower limit of mag_A are adjusted to change the galaxy sample.

As demonstrated by the lower panels of Figure 2.20, the selection bias ratios for these two cuts vary slowly when changing of the galaxy sample. The bias ratios are hence taken as constants and used to estimate selection biases for any galaxy sample by multiplying the marginal galaxy number density at the edge of the corresponding selection cuts, the resulting multiplicative and fractional additive selection biases of which are given by

$$m_{\mathrm{sel}} = -0.05854P\left(\mathrm{mag}_A = 25.5\right) + 0.01919P\left(R_2 = 0.3\right),$$
$$a_{\mathrm{sel}} = 0.00635P\left(\mathrm{mag}_A = 25.5\right) + 0.00627P\left(R_2 = 0.3\right),$$

respectively.

2.6 Internal Null Tests

2.6.1 Mock galaxy catalogs

To asses the errors of measurements including both uncertainties on shear estimation and cosmic variance, N-body simulations are used to generate mock shear catalogs. Errors are dominated by shape noise (from galaxy intrinsic shape) and shape measurement uncertainties (from the sky variance) on small scales because of the limited galaxy number whereas errors are dominated by cosmic variance on large scales. To be specific, 200 realizations of mock catalogs are generated following the method described in Oguri et al. (2018) (see also Shirasaki et al., 2019), which adopts ray-tracing results of Takahashi et al. (2017).

2.6.2 Property-dependent bias

The weighted mean shear $\langle g_1 \rangle$ and $\langle g_2 \rangle$ within each of the six observational fields is firstly calculated. These mean shear values are derived in the sky coordinates, which are quite close to the coordinates of coadded images in most cases. With the errors, the p values for a fit to zero signal for the weighted mean values are calculated. It is found that only one of the 12 p values is below a nominal threshold of 0.05, with the smallest p value of 0.024 being slightly smaller than threshold. In summary, the mean shear values indicate no sign of systematic errors.

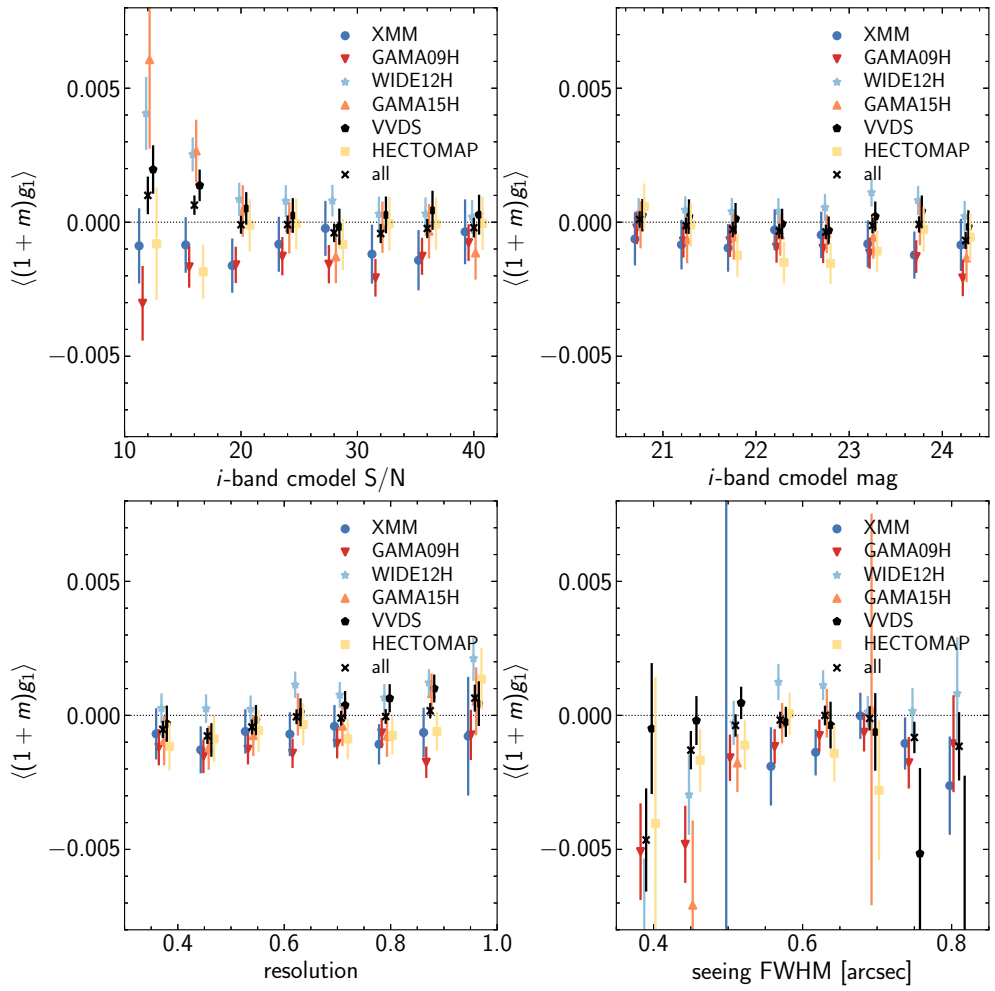

FIGURE 2.21: Weighted mean shear values $\langle g_1 \rangle$ as a function of i-band cModel SNR (*upper-left*), i-band cModel magnitude (*upper-right*), the `reGauss`resolution factor corresponding to galaxy size (*lower-left*), and PSF FWHM (*lower-right*). Errors are from mock shear catalogs and thus include cosmic shear.

The weighted mean shear values $\langle g_1 \rangle$ as a function of four i-band galaxy properties (i.e. cModel SNR, cModel magnitude, the `reGauss` resolution, and PSF FWHM) are subsequently calcualted. Results for the all fields shown in Figure 2.21 indicate that most of mean shear values are consistent with zero within 2σ. In addition, the average shear values do not show strong dependence on these galaxy properties. The average shear values for some single fields are persistently positive or negative in almost all galaxy property bins, which are very likely due to the cosmic variance.

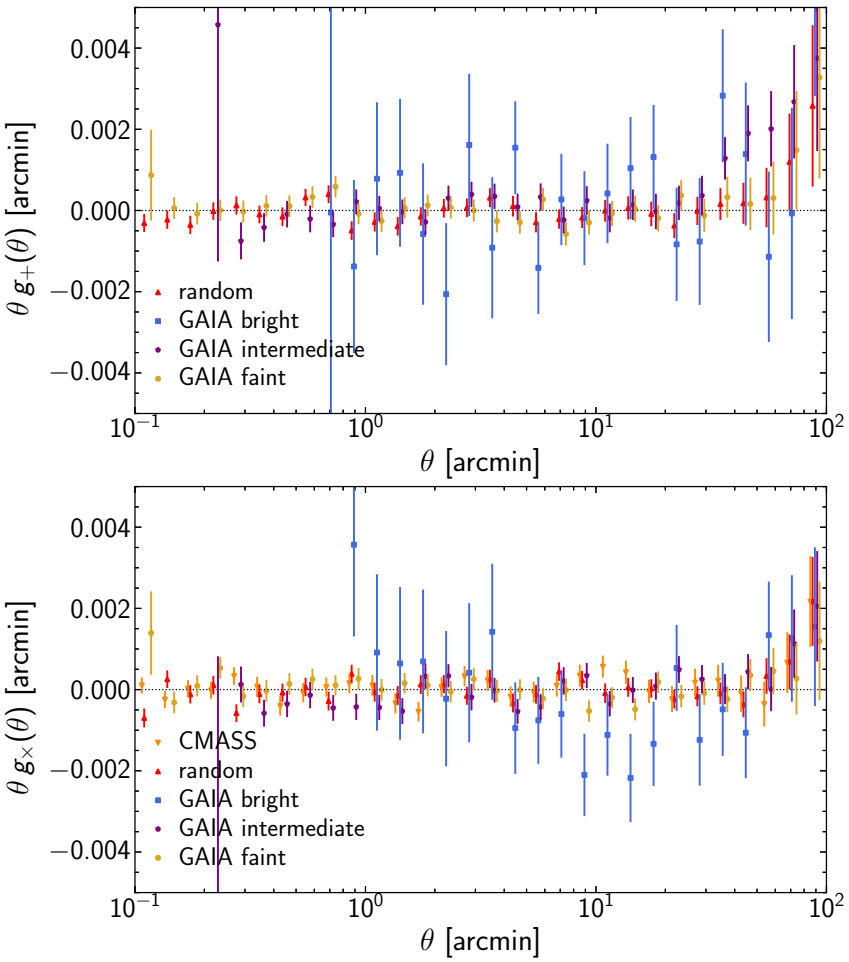

FIGURE 2.22: Stacked tangential (*upper*) and cross (*lower*) shear profiles, averaged over the entire survey, around the CMASS galaxy sample (*inverted triangles*), random points (*triangles*), bright GAIA stars with $G < 10$ (*squares*), intermediate GAIA stars with $13 < G < 14$ (*pentagons*), and faint GAIA stars with $18 < G < 18.2$ (*circles*). Only cross shear profiles are shown for stacking around CMASS galaxies. Errors are estimated from mock shear catalogs including cosmic shear. The χ^2 and p values are summarized in Tables 2.4 and 2.5.

2.6.3 Bias related to galaxy-galaxy lensing

This section conducts null tests diagnosing biases related to galaxy-galaxy lensing using stack shear signals, including both the tangential and the cross component, around different reference catalogs. The stacked cross shear signals are supposed to disappear and therefore can be used for additional null tests because of symmetry, and the stacked tangential shear signals around objects that do not induce any weak

TABLE 2.4: The χ^2 and p values for null hypothesis of stacked tangential shear profiles.

Field	Random χ^2 (p value)	GAIA bright χ^2 (p value)	GAIA intermediate χ^2 (p value)	GAIA faint χ^2 (p value)
XMM	24.76 (0.74)	17.26 (0.75)	27.01 (0.46)	48.97 (0.02)
GAMA09H	40.85 (0.09)	21.67 (0.48)	24.91 (0.58)	25.01 (0.72)
WIDE12H	27.79 (0.58)	27.78 (0.18)	26.60 (0.48)	27.50 (0.60)
GAMA15H	25.60 (0.70)	22.42 (0.43)	28.70 (0.38)	25.41 (0.70)
VVDS	29.38 (0.50)	11.92 (0.96)	25.57 (0.49)	24.56 (0.75)
HECTOMAP	22.72 (0.83)	28.51 (0.16)	30.54 (0.29)	26.49 (0.65)
ALL	28.86 (0.53)	18.28 (0.69)	25.81 (0.53)	21.96 (0.86)

TABLE 2.5: The χ^2 and p values for null hypothesis of stacked cross shear profiles.

Field	CMASS χ^2 (p value)	Random χ^2 (p value)	GAIA bright χ^2 (p value)	GAIA intermediate χ^2 (p value)	GAIA faint χ^2 (p value)
XMM	26.85 (0.63)	26.29 (0.66)	23.85 (0.35)	33.63 (0.18)	29.85 (0.47)
GAMA09H	32.07 (0.36)	27.32 (0.61)	17.65 (0.73)	44.73 (0.02)	17.96 (0.96)
WIDE12H	28.25 (0.56)	24.68 (0.74)	19.98 (0.58)	17.25 (0.93)	32.28 (0.35)
GAMA15H	25.64 (0.69)	29.51 (0.49)	18.46 (0.68)	23.69 (0.65)	39.82 (0.11)
VVDS	27.22 (0.61)	29.93 (0.47)	22.66 (0.42)	47.86 (0.01)	19.91 (0.92)
HECTOMAP	17.60 (0.96)	29.60 (0.49)	19.96 (0.58)	14.85 (0.97)	15.34 (0.99)
ALL	31.88 (0.37)	48.70 (0.02)	25.35 (0.28)	32.02 (0.23)	22.67 (0.83)

lensing signals (e.g., random positions, stars) can also be used for null tests. Here the stacked shear signals around the following catalogs are explored.

(i) Stacked shear signals are computed around the CMASS galaxy sample of the SDSS-III Baryon Oscillation Spectroscopic Survey (BOSS) Data Release 12 (DR12) (Reid et al., 2016) with an additional redshift cut of $0.4 < z < 0.7$. The galaxy density is ~ 90 deg^{-2}. Since the tangential shear profiles around the CMASS galaxies have clear positive signals, only the cross shear profiles are used for the null tests.

(ii) Stacked shear signals are conducted around random points in the HSC-SSP footprint with a target density of 100 deg^{-2}. Both tangential and cross shear profiles are used for the null tests.

(iii) Stack shear signals are computed around star catalogs from the GAIA Data Release 2 (DR2) data (Gaia Collaboration et al., 2018). The GAIA stars

are divided into three categories (i.e., the bright, intermediate, and faint star catalogs), which consist of GAIA stars with the G-band magnitude $G < 10$, $13 < G < 14$, and $18 < G < 18.2$, respectively.

Figure 2.22 summarizes results of the null tests from stacked shear signals averaged over the entire survey field. As shown, shear profiles are mostly consistent with zero, which suggest no evidence of any significant detection of systematic effects. In Tables 2.4 and 2.5, χ^2 and p values are shown for the null hypothesis of the stacked shear signals for six individual fields and the all field combined, which quantify the significance. The correlations between different radial bins, which are caused by the cosmic variance, are taking into account by deriving the full covariance matrix of the error using the 200 realizations of the mock shear catalog mentioned above. The correction factor of Hartlap et al. (2007) for an unbiased estimate of the inverse covariance matrix is incorporated. Only 4 out of 63 p values fall below a nominal threshold of 0.05, which is consistent with statistical fluctuations. In conclusion, these stacked shear signal tests show no significant evidence for significant systematics in the shear catalogs.

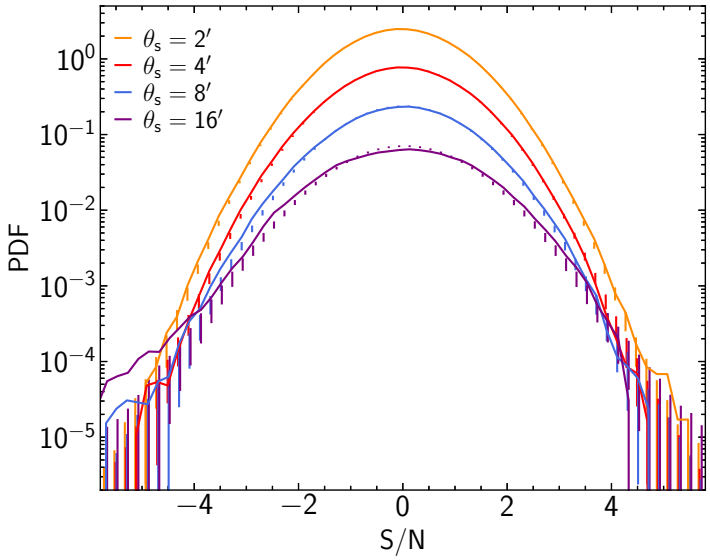

FIGURE 2.23: Observed B-mode kappa map probability distribution functions (PDFs) for different smoothing length θ_s, which are shown by solid lines, are compared to those from mock shear catalogs with errors shown by bars. For illustrative purpose, results for $\theta_s = 2'$, $4'$, and $8'$ are shifted upward by 1.5 dex, 1 dex, and 0.5 dex, respectively.

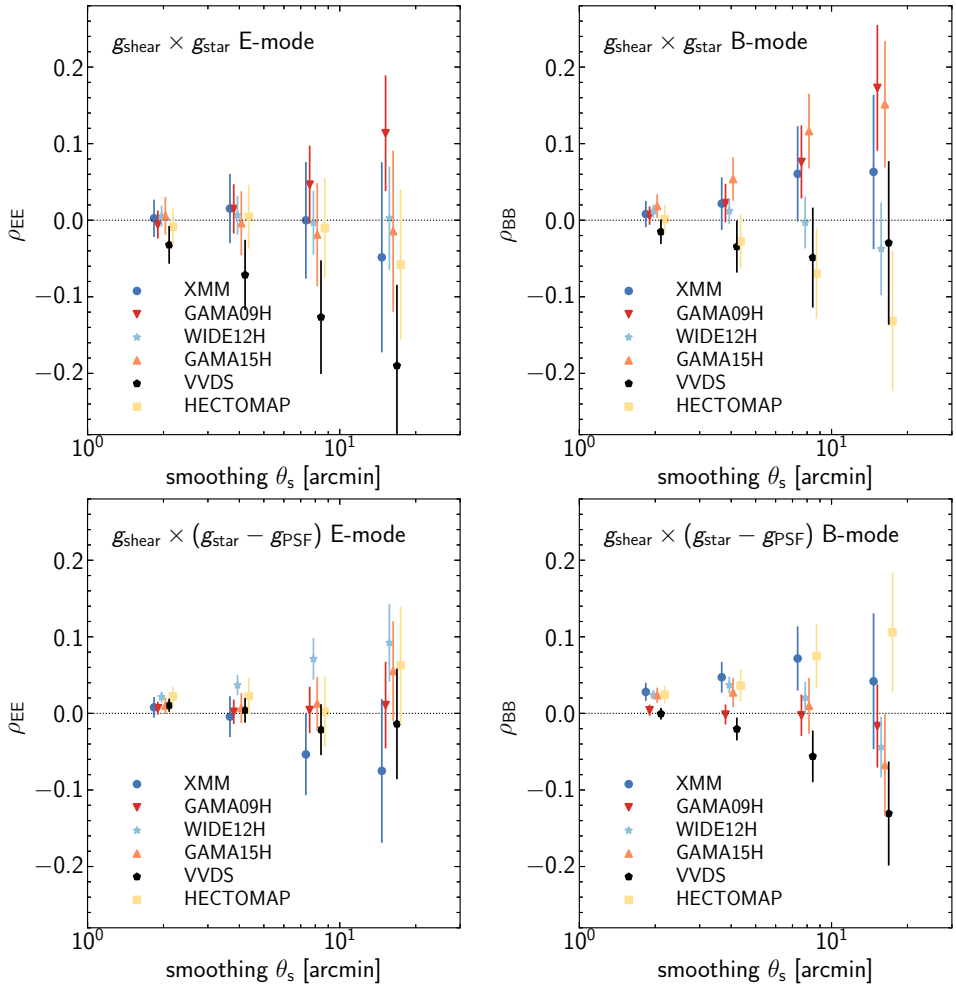

FIGURE 2.24: Pearson cross-correlation coefficients of E- (*left panels*) and B-mode (*right panels*) kappa maps and star kappa maps constructed using star ellipticities. Two cases are consider – (*lower panels*) and without *upper panels*) the PSF correction for star kappa maps. Pearson cross-correlation coefficients are shown as a function of the smoothing length of kappa maps. Different symbols show results for different observational fields. Errors are estimated from mock shear catalogs including cosmic shear.

2.6.4 Bias related to kappa maps

The observed shear field can be converted to the kappa field (projected density field)(Kaiser & Squires, 1993). "B-mode" kappa fields can be used as an additional null tests since weak lensing produces mostly "E-mode" convergence fields (Crittenden et al., 2002; Schneider et al., 2002).

For the purpose of "B-mode" null tests, the Gaussian-smoothed convergence maps are constructed by adopting four different Gaussian smoothing lengths, following the methodology detailed in Oguri et al. (2018). Figure 2.23 shows the probability distribution functions (PDFs) of the B-mode kappa maps for four different smoothing lengths and compare them to the average PDFs from mock shear catalogs that correctly capture effects of the survey boundary and bright star mask that mix E- and B-modes. It is found that the PDFs of the B-mode kappa maps roughly follow a Gaussian distribution, and they are roughly consistent with those from mock shear catalogs. The small deviations from mock results, which were also seen in the first-year HSC-SSP shear catalog (Mandelbaum et al., 2018b), are likely to originate from PSF leakage or PSF modelling errors.

As discussed in Mandelbaum et al. (2018b), kappa maps can be used for a complementary check of the PSF leakage and PSF modelling errors. Specifically, the Peason correlation coefficient $\rho_{\kappa_1\kappa_2}$ between the $E(B)$-mode kappa map and the $E(B)$-mode star kappa map is used to quantify the systematics. The star kappa maps refers to the smoothed (with Gaussian kernel) kappa map created using star ellipticities. Here two types of star ellipticities are considered, one is star ellipticities, which is used to check the PSF leakage, and the other is star ellipticities after the PSF correction, which is used to check PSF modelling errors.

In this analysis, the reserved stars that are not used for modelling the PSF are used. Figure 2.24 finds that correlations between the galaxy kappa maps and star kappa maps without the PSF correction are consistent with zero within $\sim 2\sigma$, which indicates no sign of the PSF leakage. On the other hand, small deviations from zero are found for the case of star kappa maps with the PSF correction, which suggests that PSF modelling errors may be a source of small deviations of the B-mode kappa map PDFs from mock results as shown in Figure 2.23. As done in Hikage et al. (2019) and Hamana et al. (2020), those PSF effects should be taken into account for careful cosmological analyses.

2.6.5 Bias related to cosmic shear

This section presents results of an empirical test for the possible impact of either PSF modelling errors or residual PSF anisotropy in galaxy shapes on cosmic shear two-point correlation functions. The star-galaxy cross correlation and the star auto-correlation are computed as

$$\xi_{\rm sys} = \frac{\langle g_*^\dagger \hat{g}_{\rm gal}\rangle^2}{\langle g_*^\dagger \hat{g}_*\rangle}. \tag{2.27}$$

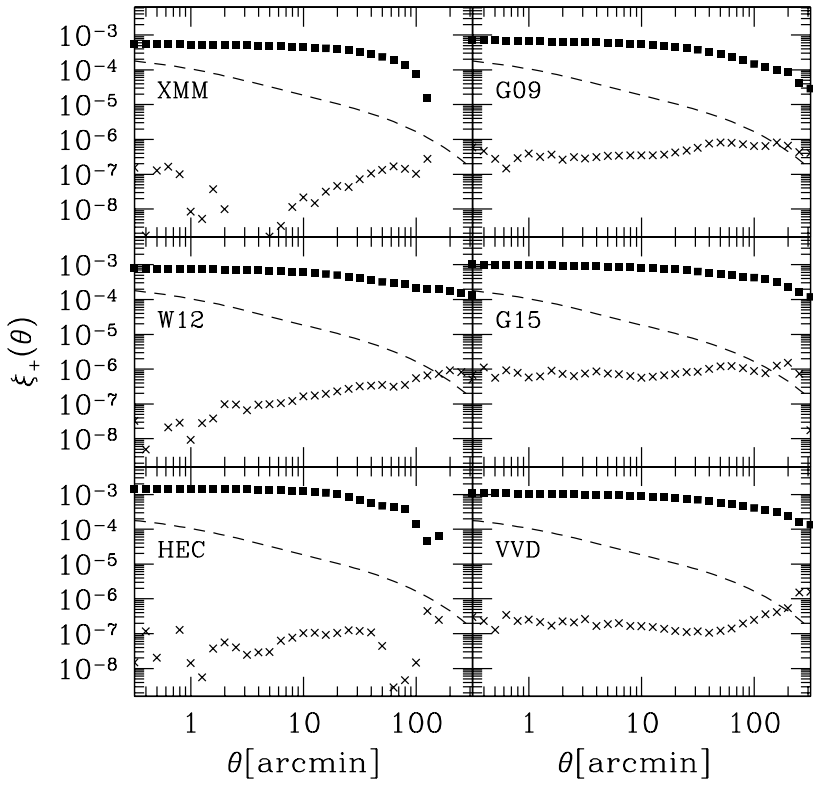

FIGURE 2.25: The shape-shape correlation function $\xi_+(\theta)$ for PSF stars is shown as points; the predicted cosmic shear correlation function (including photo-z errors) is shown as dashed lines; and the systematic correlation function $\xi_{\rm sys}$ defined in Equation (2.27) is shown as crosses.

Adopting the prescription given in section 2.2.2, these correlations give an estimate of a residual correlation caused by PSF anisotropy leakage to the galaxy-galaxy correlation function: $\Delta\langle g^\dagger g\rangle \sim a^2\langle g_*^\dagger g_*\rangle$. In addition, $\xi_{\rm sys}$ can also detect additive PSF modelling errors that contribute to $\langle g^\dagger g\rangle$. Figure 2.25 shows $\xi_{\rm sys}$ for each observational field along with the standard ΛCDM prediction of the cosmic shear correlation function ξ_+. In summary, the amplitudes and shapes of $\xi_{\rm sys}$ are similar to those of the first-year shear catalog (see Figure 18 of Mandelbaum et al. (2018b)). The amplitude of $\xi_{\rm sys}$ varies among fields and can be comparable to $\langle g^\dagger g\rangle$ on degree scales. The results indicate that a careful choice of angular (multi-pole) scales used in cosmic shear analyses and a correction for the PSF systematics are required as was done in Hikage et al. (2019); Hamana et al. (2020).

2.7 Summary

In this chapter, I present the galaxy shear catalog measured from the i-band image of the three-year HSC data. The galaxy shapes are calibrated with HSC-like image

simulations transferring the high-resolution galaxy images from COSMOS HST to the HSC observing conditions. It is confirmed that the simulated galaxy sample has the same distributions of galaxy properties as the real HSC data. The simulation is subsequently used to calibrate the galaxy property-dependent shear estimation bias, including redshift-dependent bias. The shear calibration residuals is estimated by applying the calibrated shear estimator to sub-samples of the simulation divided by several different galaxy properties. The selection bias was removed empirically from ensemble shear estimates using the simulation.

The resulting galaxy shear catalog covers an area of 433.48 deg^2 of the northern sky, split into six observational fields, with a mean i-band seeing of 0.59 arcsec. With conservative galaxy selection criteria, the raw galaxy number density is 22.9 arcmin^{-2} and the effective galaxy number density is 19.9 arcmin^{-2}. The galaxy catalog has a depth of 24.5th magnitude. In addition, the requirements for cosmological weak-lensing science for this shear catalog are defined, and quantified potential systematics in the catalog using a series of internal null tests for problems related to shear estimation.

In conclusion, for the systematics that can be characterized with the image simulations and null tests, the shear catalogs presented here meet the requirements for the HSC three-year weak lensing science.

The three-year HSC weak-lensing shear catalog is the first step to the HSC three-year weak-lensing science. There are many applications of the shear catalog, including non-cosmology analyses, e.g., mass mapping (e.g., Oguri et al., 2018) and cluster galaxy lensing, and cosmology analyses, e.g., cosmic shear (e.g., Hikage et al., 2019; Hamana et al., 2020) and galaxy-galaxy lensing (e.g., Prat et al., 2018).

3

Towards calibration-free shear estimators

As discussed in the image simulation section of Chapter 2, the calibration of shear estimation bias based on galaxy image simulations is limited by the depth of the input training galaxy sample. It is reasonable to ask: Is it possible to analytically derive a shear estimator that is able to control the systematic bias to subpercent level for any galaxy sample without relying on any calibration with image simulations.

This section proposes the Fourier power function shapelets method (`FPFS`; see Section 3.1), the multiplicative bias of which is below 1% for isolated galaxies. However the novel method still requires calibrations from external simulations for blended galaxies. The method is tests with image simulations in Section 3.2, and compared to the `reGauss` shape catalog on galaxy-galaxy lensing in Section 3.3.

3.1 `FPFS` shear estimator

3.1.1 Fourier power function

For a galaxy image, the Fourier power function is the power of its Fourier transform, which is defined as

$$\tilde{f}(\vec{k}) = \int f(\vec{x}) e^{-i\vec{k}\vec{x}} d^2x,$$
$$\tilde{F}(\vec{k}) = |\tilde{f}(\vec{k})|^2,$$

where $\tilde{f}(\vec{k})$ is the Fourier transform and $\tilde{F}(\vec{k})$ is the Fourier power function of the galaxy image.

In real observations, a boundary is defined for each galaxy, and the pixels outside

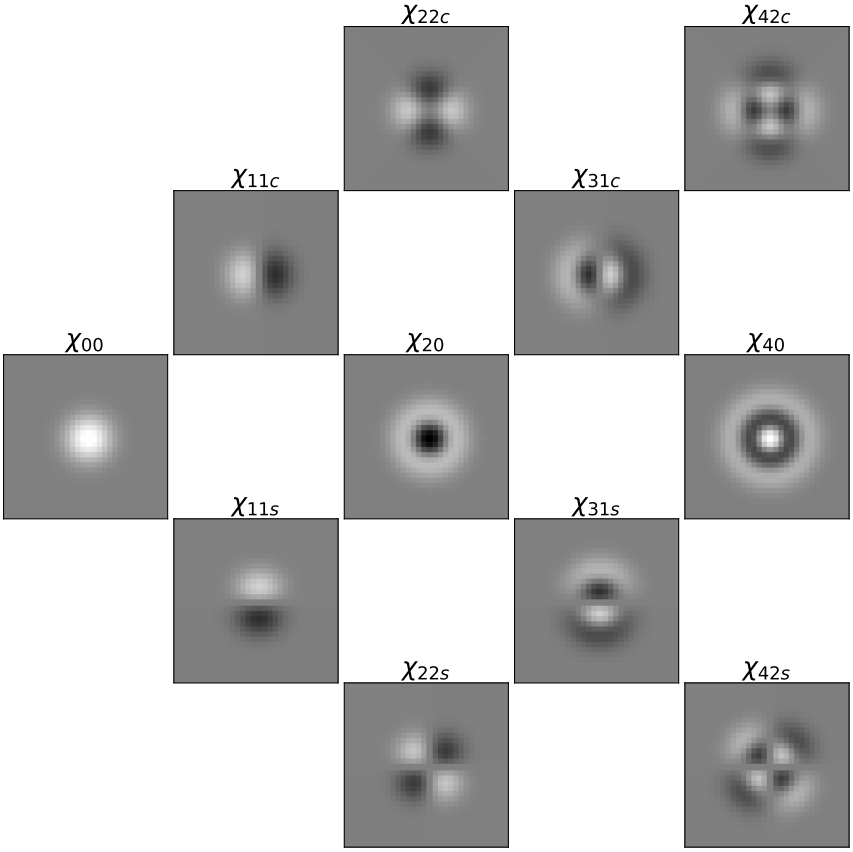

FIGURE 3.1: The shapelet basis vectors: χ_{nmc} and χ_{nms}.

the boundary are masked with zero to ensure the stability of Fourier transform. Li & Zhang (2016) proposed to use a top-hat aperture around the centroid of galaxies to define the cut off boundaries. The top-hat aperture is defined as

$$T(\vec{x}) = \begin{cases} 1, & |\vec{x} - \vec{x}_c| < r_{\rm cut} \\ 0, & |\vec{x} - \vec{x}_c| \geq r_{\rm cut} \end{cases}, \tag{3.1}$$

where $\vec{x}_c$ is the galaxy centroid and $r_{\rm cut}$ is the aperture radius.

The ratio between the aperture radius $r_{\rm cut}$ and trace radius of galaxy $r_{\rm g}$ (defined with the second-order `reGauss` moments matrix) is referred to as the aperture ratio, which is defined as

$$\alpha = \frac{r_{\rm cut}}{r_g}\,.$$

By denoting the second-order moments matrix as $\mathbf{Q}$, the trace radius is given by

$$r_g = \sqrt{\frac{tr(\mathbf{Q})}{2}}\,. \tag{3.2}$$

The aperture ratio should neither be too small to steeply cut on the galaxy's light profile, nor too big so that the measurement is heavily influenced by noise and neighboring objects' light. The accuracy of the FPFS shear estimator as a function of α will be discussed in Section 3.2.1 for isolated galaxies.

The reason for transforming to Fourier space is that the systematics from PSF effect can be removed by dividing the PSF Fourier power function $\tilde{G}$ from the observed galaxy Fourier power function $\tilde{F}_o$ as follows:

$$\tilde{F}(\vec{k}) = \frac{\tilde{F}_o(\vec{k})}{\tilde{G}(\vec{k})}, \tag{3.3}$$

where $\tilde{F}_o$ refers to the Fourier power function of the observed galaxy.

The reason for using the power function of Fourier transform is that the centroid of the Fourier power function is well defined even for a noisy faint galaxy. To be more specific, the Fourier power function of galaxies are always symmetric around its $\vec{k} = \vec{0}$ (Zhang & Komatsu, 2011), since galaxy images are real and their Fourier transforms enjoy Hermitian symmetry. Therefore, shear estimation based on Fourier power functions will not be influenced by the anisotropy from off-centering when calculating spin-2 properties (e.g., M_{22c}, M_{22s}).

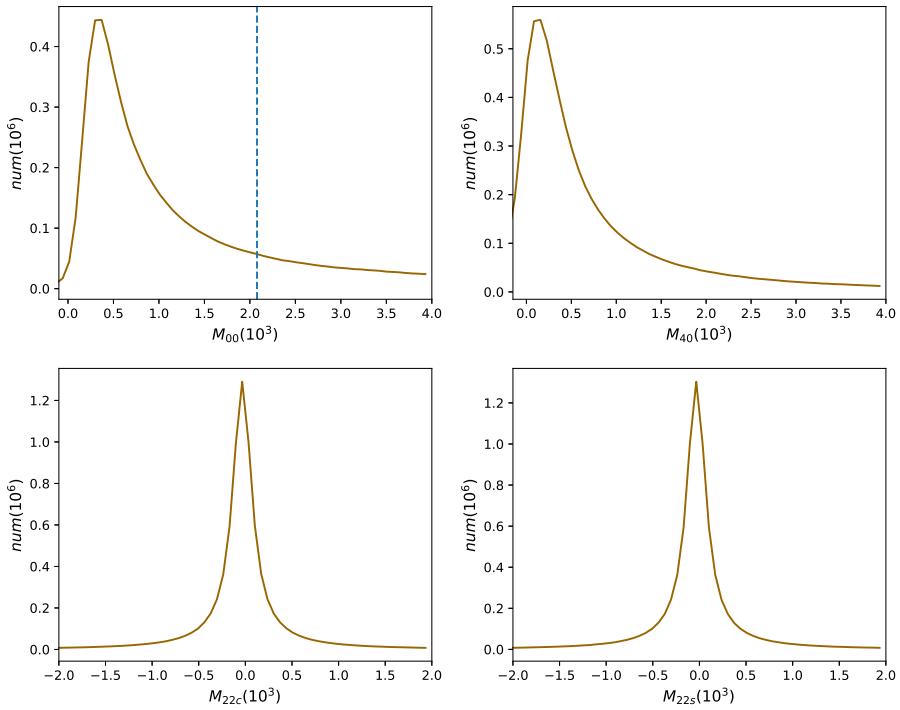

FIGURE 3.2: The number histograms of the shapelet modes M_{nm} measured from the HSC-like parametric galaxy image simulation. The dashed line in the upper-left panel shows the value of Δ used to normalize weighting parameter C as shown in Equation (3.9). The aperture ratio and shapelets scale ratio are kept to $\alpha = 4$, and $\beta = 0.85$, respectively.

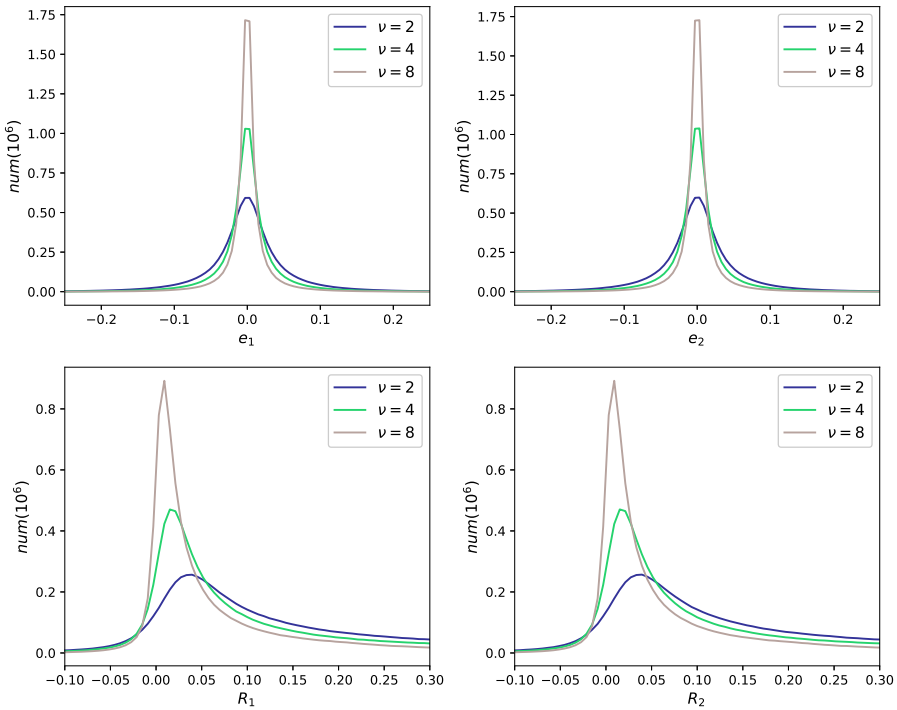

FIGURE 3.3: The number histograms of the FPFS ellipticity (*top panels*) and response (*lower panels*) with different ν (indicated by colors). The hyper parameters are set to $\alpha = 4$ and $\beta = 0.85$. These observables are measured from the parametric the HSC-like galaxy image simulation.

3.1.2 Unnormalized estimator

The weak lensing shear signal can be estimated from the Fourier power function of galaxies after PSF deconvolution by projecting the deconvolved galaxy Fourier power function onto four polar shapelet basis vectors. The polar shapelet basis vectors (Massey & Refregier, 2005) are defined as

$$\chi_{nm}(r,\theta) = \frac{(-1)^{(n-|m|)/2}}{\sigma^{|m|+1}} \left\{ \frac{[(n-|m|)/2]!}{\pi[(n+|m|)/2]!} \right\}^{\frac{1}{2}} \times r^{|m|} L^{|m|}_{\frac{n-|m|}{2}} \left(\frac{r^2}{\sigma^2} \right) e^{-r^2/2\sigma^2} e^{-im\theta},$$

where L^p_q are the Laguerre Polynomials, n is termed the radial number m is termed the spin number, and σ is the scale radius parameter of shapelet functions. The ratio between σ and the scale radius of PSF Fourier power function $r_{\rm pp}$ is denoted as

$$\beta = \frac{\sigma}{r_{\rm pp}}, \tag{3.4}$$

and referred to as shapelets scale ratio here. $r_{\rm pp}$ is measured from the noiseless PSF model in the same way as Li & Zhang (2016). Here $r_{\rm pp}$ is measured as

$$r_{\rm pp} = \sqrt{\frac{A}{\pi}},$$

where A is the area of pixels with greater values than $e^{-0.5}$ of the maximum of the PSF power function. β should be less than one to ensure that the PSF deconvolution in Fourier space does not amplify the noise at small scale (large wave numbers). The hyper parameters α and β determine the scales in real space and Fourier space, respectively. Section 3.2.1 demonstrates the accuracy of the `FPFS` shear estimator with different choices of α and β using the modelled galaxy sample of the HSC-like simulations.

The resulting projection factors M_{nm}, which is referred to as shapelet modes in this thesis, are given by

$$M_{nm} = \int \chi^*_{nm} \tilde{F}(r,\theta) r dr d\theta \,. \tag{3.5}$$

When $m > 0$, shapelet modes are complex, and M_{nmc} (M_{nms}) is used to denote their real (imaginary) part. Due to the Hermitian symmetry of power function, all of the shapelet modes with an odd spin number vanish. The corresponding shapelet basis vectors χ_{nmc} and χ_{nms} are demonstrated in Figure 3.1.

Four shapelet modes are used to construct the FPFS ellipticity, the histograms of which are measured from the parametric galaxies with HSC-like observational condition are shown in Figure 3.2. As shown by the vertical dashed line in the figure of M_{00}, the value of M_{00} at which its histogram drops below 1/8 of its maximum is denoted as Δ to quantify the spread of M_{00},

The transform formulas of the shapelet modes influenced by a shear distortion have been given by Massey & Refregier (2005), which are laid out as follows:

$$\begin{aligned}
M_{22c} &= \bar{M}_{22c} - \frac{\sqrt{2}}{2} g_1 (\bar{M}_{00} - \bar{M}_{40}) \\
&\quad + \sqrt{3} g_1 \bar{M}_{44c} + \sqrt{3} g_2 \bar{M}_{44s}, \\
M_{22s} &= \bar{M}_{22s} - \frac{\sqrt{2}}{2} g_2 (\bar{M}_{00} - \bar{M}_{40}) \\
&\quad - \sqrt{3} g_2 \bar{M}_{44c} + \sqrt{3} g_1 \bar{M}_{44s}, \\
M_{00} &= \bar{M}_{00} + \sqrt{2}(g_1 \bar{M}_{22c} + g_2 \bar{M}_{22s}), \\
M_{40} &= \bar{M}_{40} - \sqrt{2}(g_1 \bar{M}_{22c} + g_2 \bar{M}_{22s}) \\
&\quad + 2\sqrt{3}(g_1 \bar{M}_{62c} + g_2 \bar{M}_{62s}),
\end{aligned} \tag{3.6}$$

where $\bar{M}_{nm}$ denotes the shapelet modes of intrinsic galaxies, i.e., before shear distortions, whereas M_{nm} denotes the distorted shapelet modes. What we can learn from these formulas is that it is possible to measure shear signal by taking the expectation values on the both sides of Equation (3.6).

With the assumption that the galaxy ensemble is randomly selected without preference on any specific direction, the expectations of intrinsic spin-2 and spin-4 shapelet modes on the right hand side of Equation (3.6) reduce to zero, and the population variances of the intrinsic quantities lead to the shape noise. The shear estimator is given by

$$g_1 = -\frac{\left\langle \sqrt{2} M_{22c} \right\rangle}{\langle M_{00} - M_{40} \rangle}, \qquad g_2 = -\frac{\left\langle \sqrt{2} M_{22s} \right\rangle}{\langle M_{00} - M_{40} \rangle}. \tag{3.7}$$

However, such shear estimator is heavily influenced by the shape noise on bright galaxies since bright galaxies are significantly overweighted in the shear estimation compared to faint galaxies. As a result, this estimator is suboptimal. A weighting scheme is in demand to reduce the shape noise in the shear estimation.

3.1.3 Normalized estimator

A novel normalization scheme with these four shapelet modes is introduced here. First, the dimensionless `FPFS` ellipticity is defined as

$$e_1 = \frac{M_{22c}}{M_{00}+C}, \qquad e_2 = \frac{M_{22s}}{M_{00}+C}\,. \tag{3.8}$$

Here the constant parameter C is used to adjust the relative weight between galaxies with different luminosities, which is referred to as weighting parameter. The weighting parameter is normalized by Δ, and the resulting normalized weighting parameter is denoted as ν, which is given by

$$\nu = \frac{C}{\Delta}\,. \tag{3.9}$$

With the definition of the shear response as

$$\mathcal{R}_i = \frac{\sqrt{2}}{2}\frac{M_{00}-M_{40}}{M_{00}+C} + \sqrt{2}e_i^2, \tag{3.10}$$

the transform of the `FPFS` ellipticity after a shear distortion is subsequently given by

$$\begin{aligned} e_1 &= \bar{e}_1 - g_1\bar{\mathcal{R}}_1 + \sqrt{3}g_1\frac{\bar{M}_{44c}}{\bar{M}_{00}+C} + \sqrt{3}g_2\frac{\bar{M}_{44s}}{\bar{M}_{00}+C}, \\ e_2 &= \bar{e}_2 - g_2\bar{\mathcal{R}}_2 - \sqrt{3}g_2\frac{\bar{M}_{44c}}{\bar{M}_{00}+C} + \sqrt{3}g_1\frac{\bar{M}_{44s}}{\bar{M}_{00}+C}\,. \end{aligned} \tag{3.11}$$

Figure 3.3 shows the histograms of $e_{1,2}$ and $\mathcal{R}_{1,2}$ for different setups of parameter ν.

For galaxies distorted by a constant shear, the lensing shear can be measured as the ratio between the expectation of the ellipticities versus that of the shear response. Assuming that the galaxies are randomly oriented, the expectation value of the spin-2 and spin-4 quantities in Equation (3.11) reduces to zero and the population variance of these quantities on the right-hand-side of Equation (3.11) lead to the shape noise. In addition, the expectation of the intrinsic response ($\langle\bar{\mathcal{R}}_{1,2}\rangle$) is the same as that of the observed response ($\langle\mathcal{R}_{1,2}\rangle$). The shear estimator is hence constructed as

$$g_i = -\langle e_i\rangle \,/\, \langle\mathcal{R}_i\rangle\ . \tag{3.12}$$

For the shear estimator, the intrinsic response ($\bar{\mathcal{R}}_{1,2}$) acts as a weight on each galaxy. As shown in the left panel of Figure 3.8, more weight is added to brighter galaxies as ν increases. Taking the limit that $\nu\to\infty$, the shear estimator reduces to Equation (3.7). In summary, the precision of the shear estimation is dependent on the value of ν, which will be detailed in Section 3.2.1. ν can be set to any positive

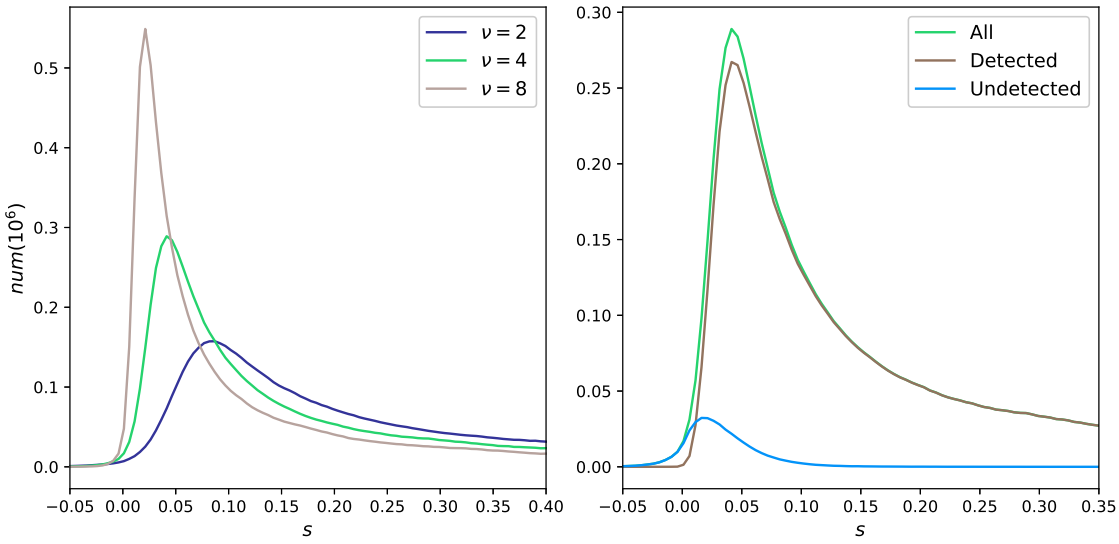

FIGURE 3.4: *Left panel:* The number histograms of the FPFS flux ratios defined in Equation (3.14). Lines with different colors refer to different values of ν. *Right panel:* The histograms of detected galaxies, undetected galaxies, and all galaxies.

value in the absence of photon noises. However, in the presence of noise, the accuracy of the shear estimation is dependent on the value of ν, which will be detailed in Section 3.1.4 and Section 3.2.1.

3.1.4 Noise bias

Photon noise due to the sky variance include the contributions from the source galaxy (galaxy Poisson noise) and those from the sky background (background noise). Photon noise does *not* correlate with the surface brightness distributions of galaxies, even after the coaddition process, since its realization is independent on galaxy surface bright field. Based on this premise, the averaged contamination of photon noise on the power function can be removed by subtracting the Fourier power function of noise from the Fourier power function of galaxy (for details, see Zhang et al., 2015).

At the single exposure level, photon noise is found to be not correlated across CCD pixels (see Zhang et al., 2015); therefore, the power spectrum of noise is flat. The expectation of power function of photon noise for each galaxy can be estimated using its value at large wave number in Fourier space. The estimated noise power function is subsequently subtracted from the galaxy Fourier power function (Zhang et al., 2015) to remove the bias from it.

At the coadded image level, the coaddition process correlates photon noise across pixels and leads to a decaying profile in the noise power spectrum. It is necessary

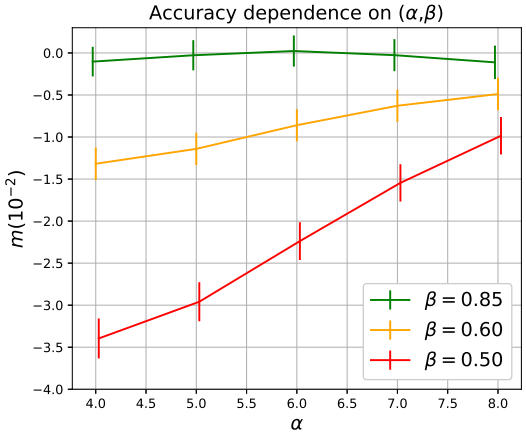

FIGURE 3.5: Multiplicative bias in the FPFS shear estimator for different setups of α and β. Each line shows the bias as a function of α, the color of which indicate the value of β. The test is conducted on HSC-like parametric galaxy image simulations with the weighting parameter ν set to 4.

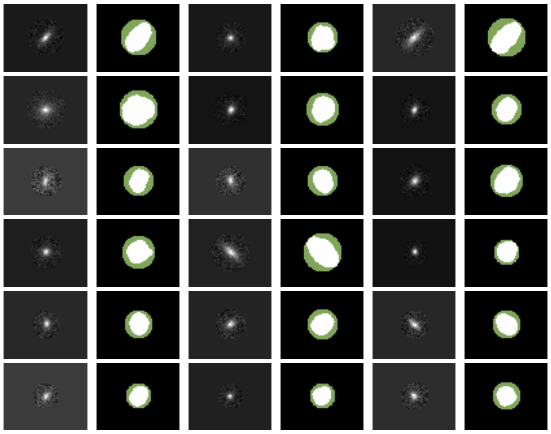

FIGURE 3.6: The galaxy images (first, third, fifth columns) and masks (second, fourth, sixth columns) from parametric galaxy image simulations where the aperture ratio α is set to 4. In the mask images, the white pixels show the detected footprints, and the gray pixels show the area within the aperture radius.

to estimate the profile of the expectation of noise power spectrum from blank pixels to remove the influence of noise on average from each galaxies. The profile of Fourier power function of noise can be estimated from the noise correlation function of blank pixels (Li et al., 2018), assuming that the correlation function of noise remains the same between blank pixels and the pixels containing detected sources, and the influence from undetected sources is negligible.

After subtracting the expectation of noise power function, noise residual, the expectation of which is zero, is left on the Fourier power function of the galaxy. The shapelet modes of the noise residual are denoted as N_{nm}. The expectation value of these shapelet modes is zero. Taking an example of the case that $\nu = 0$, the noise residual leads to noise bias due to the nonlinear form of the FPFS ellipticity and the response. For $\langle e_1 \rangle$, the expectation value of e_1 changes to

$$\langle e_1 \rangle = \left\langle \frac{M_{22c} + N_{22c}}{M_{00} + N_{00}} \right\rangle \neq \left\langle \frac{M_{22c}}{M_{00}} \right\rangle,$$

which is biased from the noiseless ellipticity. In order to reduce the noise bias originating from the nonlinearity of the ellipticity, ν is increased to ensure that

$M_{00} + C \gg N_{00}$, and the resulting expectation value of e_1 changes to

$$\langle e_1 \rangle = \left\langle \frac{M_{22c}}{M_{00} + C}(1 + O(\epsilon^2)) \right\rangle , \tag{3.13}$$

where

$$\epsilon = \frac{N_{00}}{M_{00} + C} \ll 1 .$$

In summary, the noise bias is proportional to ϵ^2. The expectation values of e_2 and $\mathcal{R}_{1,2}$ have similar form as Equation (3.13). Noise bias reduces as ν increases; however, we note that the value of ν cannot be too large otherwise the bright galaxies are significantly overweighted and the shear estimation is dominated by the shape noise of bright galaxies. The accuracy and precision as a function of ν are shown in Section 3.2.1 using the parametric galaxy simulation with the HSC-like observational condition.

3.1.5 Selection bias

This section discusses the selection bias caused by an anisotropic selection of galaxies. To complete a selection of a galaxy ensemble, one need to define a selection property and its corresponding selection threshold. After that, a galaxy is counted as a member of the galaxy ensemble if the selection property fall within the selection threshold. In order to avoid the systematic bias due to an anisotropic selection, the selection property should be an isotropic (spin-0) quantity on the *intrinsic plane* so that the expectation of the intrinsic shape noise due reduces to zero.

To be more specific, let's define the `FPFS` flux ratio:

$$s = \frac{M_{00}}{M_{00} + C}, \tag{3.14}$$

and select a galaxy ensemble with the `FPFS` flux ratio. The left panel of Figure 3.4 shows the histograms of s with different setups of ν. The `FPFS` flux ratio is influenced by the shear and the relationship between the sheared `FPFS` flux ratio (s) and the intrinsic `FPFS` flux ratio ($\bar{s}$) is given by

$$s = \bar{s} + \sqrt{2} g_1 \bar{e}_1 (1 - \bar{s}) + \sqrt{2} g_2 \bar{e}_2 (1 - \bar{s}) . \tag{3.15}$$

As shown by Equation (3.14) and (3.15), although $\bar{s}$ is an isotropic property on the intrinsic plane, s is not since shear entangle $\bar{s}$ with the galaxy shapes. Therefore, the selection process with a direct cut on s does not perform an isotropic selection

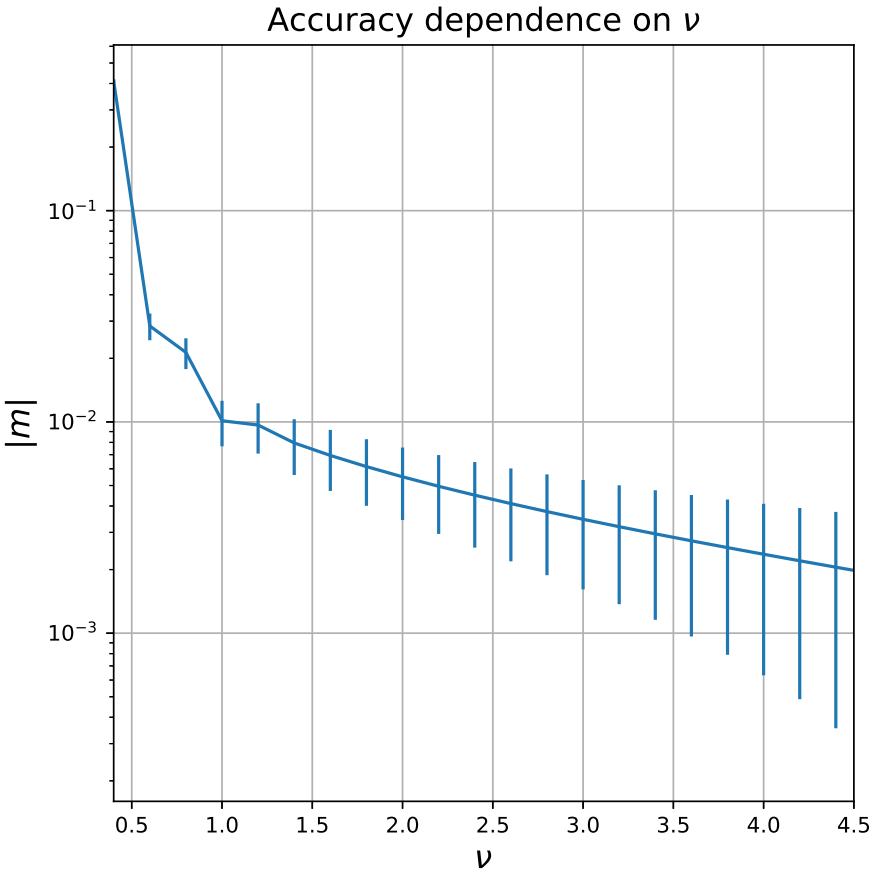

FIGURE 3.7: Multiplicative bias as a function of the hyper parameter ν. The other hyper parameters are set to the default values, namely $\alpha = 4$, $\beta = 0.85$.

on the intrinsic plane. Such selection hence does not align with the premise that the intrinsic galaxies have isotropic orientations statistically and result in a selection bias. An iterative method is proposed in (Li et al., 2018) to reduce the selection bias:

(i) Estimate shear with selection $L < s < U$, the result of which is denoted as $\hat{g}^A_{1,2}$.

(ii) Transform the observed selection property s into s_R with $\hat{g}^A_{1,2}$ according to Equation (3.15).

(iii) Redo shear estimation of (i), but with selection: $L < s_R < U$ and update the estimated shear.

In addition, the galaxy detection process also act as a selection which could depend on shear and thus cause selection bias. The histogram of s ($\nu = 4$) for the undetected galaxies is shown on the right panel of Figure 3.4, which suggests that most of the undetected galaxies populate in the range: $s < 0.1$. The result indicates that as long as the cut on s is set to be greater than 0.1, the bias from the detection

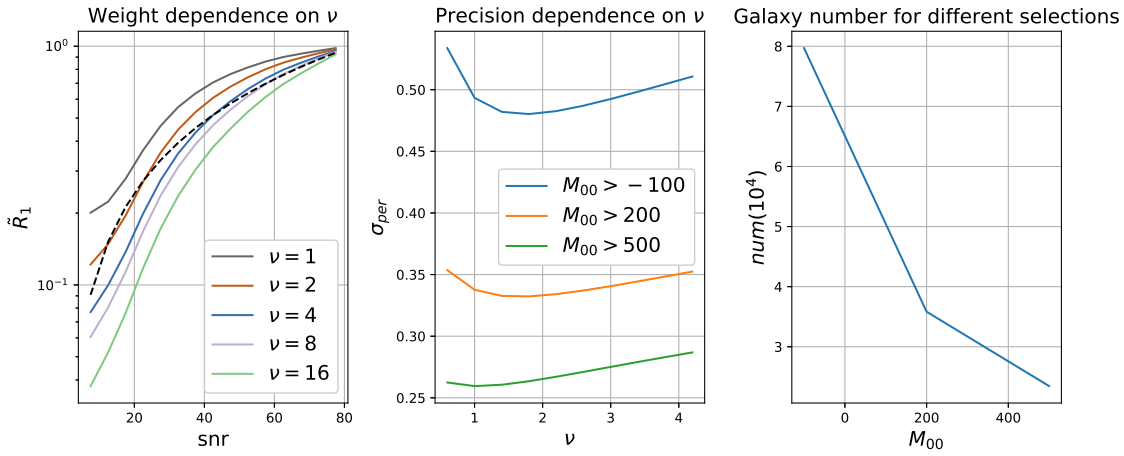

FIGURE 3.8: *Left panel:* The relative weight between galaxies as a function of SNR for different setups of ν. The x-axis is the SNR bins and the y-axis is the averaged R_1 normalized by the averaged R_1 of the bin at $75 < S/N < 80$. The solid lines are for different ν; whereas the dashed line shows weight ratio is proportional to the SNR as a reference. *Middle panel:* The precision of the estimator as a function of ν for galaxy sample selected with different lower limits on M_{00}. The x-axis is the weighting parameter (ν) and the y-axis is the shear measurement error per galaxy per component. Lines with different colors represent different lower selection threshold on M_{00}. *Right panel:* The galaxy number as a function of the lower lower limit on M_{00}. The default setup is $\alpha = 4, \beta = 0.85$.

process is negligible since the detection does not influence the selected galaxy sample significantly.

3.2 Test on image simulations

This section serves to test the `FPFS` shear estimator using the HSC-like galaxy image simulations presented in Mandelbaum et al. (2018a). Mandelbaum et al. (2018a) provide four samples of postage stamp-based galaxy image simulations. Sample 1 and sample 2 are composed of isolated galaxies, where sample 1 uses HST galaxies from Leauthaud et al. (2007); and sample 2 uses parametric galaxy models fitted to the HST galaxies. On the other hand, sample 3 and sample 4 include also blended galaxies, which are more realistic. Sample 3 cuts out the HST images near the HST galaxy detections, the cut out widths are in general smaller than the width of postage stamps. Sample 4 matches the HSC galaxy detections to the HST image coordinates, and cut out the images near the matched positions with a cut off width equals width of postage stamp. These four samples of image simulations are summarized in Table 1 of Mandelbaum et al. (2018a).

3.2.1 Hyper parameters

The FPFS shear estimator includes three free hyper parameters, i.e., α,β,ν. α (β) determines the measurement scale in real (Fourier) space, whereas, ν determines the relative weight between galaxies with different brightness and reduces noise bias. This section serves to determine the accuracy and precision of the shear estimator as a function of these hyper parameters.

Li & Zhang (2016) looked into the influence of α on the accuracy of the shear estimator of Zhang & Komatsu (2011), which corresponds to the case of $\nu = +\infty$ for this FPFS estimator. They kept $\beta = 0.5$ as a constant and did not consider the dependence of the accuracy on β. Here the accuracy of the FPFS estimator as a joint function of α and β is studied. After that, Li et al. (2018) studied the accuracy as a function of α and β. The result of multiplicative bias is shown in Figure 3.5; whereas, the additive bias is not shown here since it is at the level of 10^{-4}.

This test is conducted on HSC-like parametric galaxy image simulations, and the hyper parameter ν is fixed to 4 to focus on the accuracy dependence on α and β. Galaxies are selected with intrinsic SNR (measured before the shear distortion) greater than 5. As shown, for $\beta = 0.5$, the multiplicative bias reaches 1% when the aperture ratio drops to 8. This is consistent with Li & Zhang (2016). It is worth noting that, when β is set to 0.85, the multiplicative bias is consistent with zero even though α drops to 4 . In summary, the region extended to four times of each galaxy's half light radius is required for an accurate shear measurement given that α is kept to 0.85. For illustrative purposes, the galaxy images and the corresponding mask image in the HSC-like parametric galaxy image simulations is shown in Figure 3.6. The connected white pixels on the mask planes show the footprints of galaxies and the circular regions with gray pixels on the mask planes are the top-hat aperture with $\alpha = 4$. According to the results, these two hyper parameters are fixed to $\beta = 0.85$ and $\alpha = 4$ as the fiducial setup in the following content.

Li et al. (2018) also studied the accuracy of the FPFS shear estimation as a function of ν. In the corresponding tests, shear measurements are conducted with different ν on the HSC-like parametric galaxy simulation. The multiplicative bias is shown in Figure 3.7 as a function of ν; whereas, the additive bias is not shown here since it is only a few parts in 10^4. As shown, in order to ensure the multiplicative bias is reduced below one percent, ν should be at least greater than 1 .

Li et al. (2018) also studied the dependence of the precision on the value of ν. ν influence the precision of the shear estimation by changing the relative weights between galaxies with different SNR. In order to demonstrate how ν changes the relative weights, galaxies are separated into different intrinsic SNR bins. The averages

sample & setup	$m_1(10^{-2})$	$c_1(10^{-4})$	$m_2(10^{-2})$	$c_2(10^{-4})$
S3-ND	-0.25 ± 0.22	0.75 ± 0.56	0.03 ± 0.23	-0.71 ± 0.59
S3-D	-5.71 ± 0.24	3.33 ± 0.60	-5.59 ± 0.24	-1.06 ± 0.60
S4-ND	-1.68 ± 0.27	0.24 ± 0.71	-1.11 ± 0.23	0.19 ± 0.57
S4-D	-5.83 ± 0.41	1.27 ± 1.06	-5.59 ± 0.30	-0.71 ± 0.75

TABLE 3.1: Accuracy of the `FPFS` algorithm tested on sample 3 and sample 4 with two different setups. The column 'sample & setup' indicates the sample and the setup. The hyper parameters are set to $\alpha = 4$, $\beta = 0.85$, and $\nu = 4$) .

of R_1 as functions of the intrinsic SNR for different setups of ν are shown in the left panel of Figure 3.8. The case where weight ratio is proportional to intrinsic SNR is also shown in the left panel of Figure 3.8 as a reference.

Shear measurement error refers to the uncertainty in the shear estimation, which includes shape estimation uncertainties (i.e., the uncertainties in galaxy shape estimation) and shape noise (i.e., the uncertainties due to the random orientations of galaxies). The shear measurement error as a function of ν is studied by randomly rotating 8×10^4 parametric galaxies selected from the 25.2 magnitude limited COSMOS HST catalog.

The estimated shear measurement errors per galaxy per shear component for different ν and different selection thresholds on M_{00} are shown in the *middle panel* of Figure 3.8. The *right panel* of Figure 3.8 shows the corresponding galaxy number for different M_{00} cuts at the lower end. As shown in the *middle panel* of Figure 3.8, an optimal setup of ν is between the range of $\nu = 1 - -2$, which slightly overweight bright galaxies since the shape estimation uncertainties on faint galaxies are larger compared to bright galaxies since bright galaxies are less influenced by noise.

As shown in Li et al. (2018), in the presence of blending, the `FPFS` shear estimator need to be calibrated for blending bias due to the imperfections in the HSC deblending algorithms used to isolate blended sources from each other. The bias due to blending for faint galaxies is much larger compared to bright galaxies. Therefore, ν is set to 4.0 as the fiducial setup, with the intent to put more weight to bright galaxies. Moreover, such setup also ensures that noise bias is adequately reduced below 1%.

3.2.2 Isolated galaxies

This section show the results of the `FPFS` shear estimator tested with the HSC-like parametric galaxy (sample 2) and realistic galaxy images (sample 1) of Mandelbaum et al. (2018a) in the absence of blending. Shear distortions are measured from these galaxy images with different selection selections, namely different selection properties and selection cuts. The selection properties that are tested include intrinsic SNR,

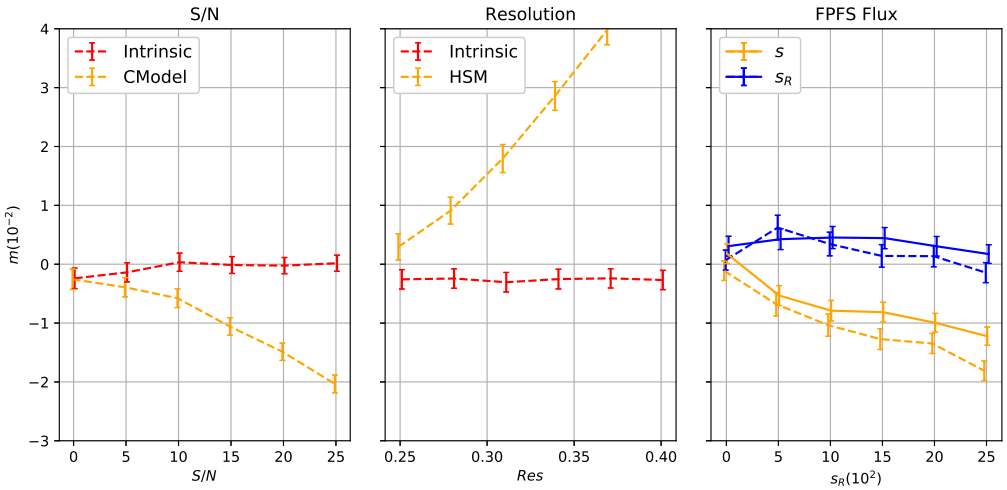

FIGURE 3.9: *Left panel:* Multiplicative bias as a function of the lower limits intrinsic SNR (red line) and cModel SNR (yellow line). *Middle panel:* Multiplicative bias as a function the lower limits of intrinsic `reGauss` resolution (red line) and resolution measured by the HSM algorithm (yellow line). *Right panel:* Multiplicative bias as a function of the lower limits the observed `FPFS` flux ratio (yellow lines) and the revised `FPFS` flux ratio (blue lines). The solid lines represent tests done on realistic galaxies and the dashed lines represent tests on parametric galaxies.

observed cModel SNR, intrinsic `reGauss` resolution, observed `reGauss` resolution, observed `FPFS` flux ratio, and revised `FPFS` flux ratio. The fiducial setup (i.e., $\alpha = 4$, $\beta = 0.85$, and $\nu = 4$) for the hyper parameters are adopted in these tests.

Figure 3.9 shows the multiplicative biases as functions of selection cut for different selection properties. As shown by the *left panel* (*middle panel*), the multiplicative biases are blow 0.5% when the intrinsic SNR (intrinsic `reGauss` resolution) are used to select galaxies. Note that the selections using these intrinsic properties do not lead to any multiplicative selection bias by construction. However, if the observed galaxy properties (e.g., cModel SNR or `reGauss` resolution) are used to select galaxies, selection bias is included into the resulting multiplicative bias. The right panel of Figure 3.9 shows the results for observed `FPFS` flux ratio and the revised `FPFS` flux ratio with the iterative correction method introduced in Section 3.1.5. As shown, the iterative method reduces selection bias below 1% .

In addition, as shown in the right panel of Figure 3.9, the results for realistic galaxies (sample 1) and parametric galaxies (sample 2) are consistent with each other even though the galaxy morphology in these two samples are different, which indicate that the `FPFS` shear estimation for isolated galaxies is not influenced by model bias.

The correlation between additive bias and PSF ellipticity $e_{1,2}^{\rm PSF}$ is tested on the HSC-like parametric galaxy simulations (sample 2). The ellipticity of PSF is obtained from the `reGauss` second-order moment matrix. Setting the fiducial multiplicative

bias to zero, the PSF ellipticity is fitted to the shear residual by

$$\delta g_{1,2} = \hat{g}_{1,2} - g_{1,2} = a_{1,2} e^{\rm PSF}_{1,2}, \tag{3.16}$$

where $a_{1,2}$ is the fractional additive bias which describes the fraction of the PSF ellipticity leaking into the shear measurement (Mandelbaum et al., 2018a). The resulting fractional additive bias is 0.004 , which is far below the first-year HSC science requirements. In summary, the additive bias is almost not correlated with the PSF ellipticity for the `FPFS` shear estimator.

3.2.3 Blended galaxies

This section serves to test the accuracy of the `FPFS` shear estimator on galaxy samples that contain both isolated and blended galaxies. The detected footprints in these samples are processed with two different setups, namely 'Deblended' and 'Nondeblended'. For the 'Deblended' setup, the HSC deblender (Bosch et al., 2018) is run to isolate sources on a detected footprint if it contains multiple number of peaks before estimating the shapes of the sources. On the other hand, for the 'Nondeblended' setup, the deblender is not run on any footprint even though multiple peaks are detected in one footprint.

'S3-D' ('S3-ND') is used to denote the case that 'Deblended' ('Nondeblended') setup is applied to sample 3. Similarly, 'S4-ND' ('S4-ND') refers to the 'Deblended' ('Nondeblended') setup applied to sample 4. The fiducial setup (i.e., $\alpha = 4$, $\beta = 0.85$, and $\nu = 4$) of the hyper parameters is adopted, and the galaxy ensemble is selected with the cut: $s_R > 1.5\%$.

The results of these tests are laid out in Table 3.1. The additive bias is at the level of $\sim 4 \times 10^{-4}$; therefore, discussions will be focused on the multiplicative bias. For the 'Deblended' setup, a multiplicative bias at the level of $\sim 5.7\%$ arises if the HSC deblender is used to isolate blended sources. Compared to the multiplicative bias in isolated galaxy image simulations shown in Section 3.2.2, it is likely that the conclusion that the HSC deblender fails to recover the true galaxy light profiles precisely. The discrepancy between the deblended galaxies and the true galaxies causes the multiplicative bias. I list the possible origins of the discrepancy as follows:

(i) The current version of the HSC deblender assumes a 180° rotational symmetry around the detected peak.

(ii) The current version of the HSC deblender changes the correlations of photon noise across pixels in the source footprint.

The multiplicative bias for 'S3-ND' is below 1%; whereas, a multiplicative bias of $\sim$ 1.5% is found in 'S4-ND'. Taking into account the difference between the observational conditions between sample 3 and sample 4, this additional bias for 'S4-ND' should be caused by the contamination of light from the neighbouring objects in the footprint of the obect to measure. 'S3-ND' and 'S4-ND' indicate that it is possible to directly measure a 'parent' source in one piece without any deblending, if all of its 'child' sources are distorted by the same shear (e.g., they 'child' sources are located at the same redshift). The `FPFS` shear estimator works well on the 'parent' sources since it does not make any assumption on galaxy morphology and is not sensitive to the galaxy off-centerings. Note that, however, it is not straightforward to apply this strategy to real data since the 'child' sources of a 'parent' source could be located at different redshifts, resulting in different shears on these 'child' sources. As pointed out by MacCrann et al. (2020), this redshift-dependent shears changes the galaxy number distribution over redshift.

To further understand the multiplicative bias related to blending, galaxies are divided into different s_R bins, and the multiplicative bias is determined separately using the galaxies in each bin, the results of which are shown in Figure 3.10. As shown, for the setups of 'S3-ND' and 'S4-ND', the multiplicative biases converge to $\sim -1.8\%$ at the bright end. This $\sim -1.8\%$ multiplicative bias indicates that the default aperture ratio α determined in 3.2 would be too small for an accurate shear estimation from a 'parent' source containing multiple number of galaxies.

Since the estimator suffers from systematics related to blending, the blending bias need to be calibrated with the HSC-like simulations. Sample 4 is the fiducial simulation since it best matches the real observational conditions among the simulations provided in Mandelbaum et al. (2018a). The result for 'S4-D', which is demonstrated by the green line in Figure 3.10, is consistent with our expectation: the deblending algorithms should perform better on bright galaxies than on faint galaxies. A third-order polynomial fitting is conducted to fit the multiplicative bias for 'S4-D' as a function of the revised `FPFS` flux ratio.

After estimating and modeling the multiplicative bias as a function of the revised `FPFS` flux ratio, the calibration factor – $1 + m(s_R)$ – is multiplied to the response $\mathcal{R}_{1,2}$ to calibrate the bias in the shear estimation. Substituting the revised `FPFS` flux ratio s_R with the observed `FPFS` flux ratio s does not change the expectation value of calibrated response significantly. This is given out after substituting Equation 3.15 into the calibrated shear response:

$$\left\langle m(s)\mathcal{R}_{1,2}\right\rangle = \left\langle m(s_R)\mathcal{R}_{1,2}\right\rangle \ .$$

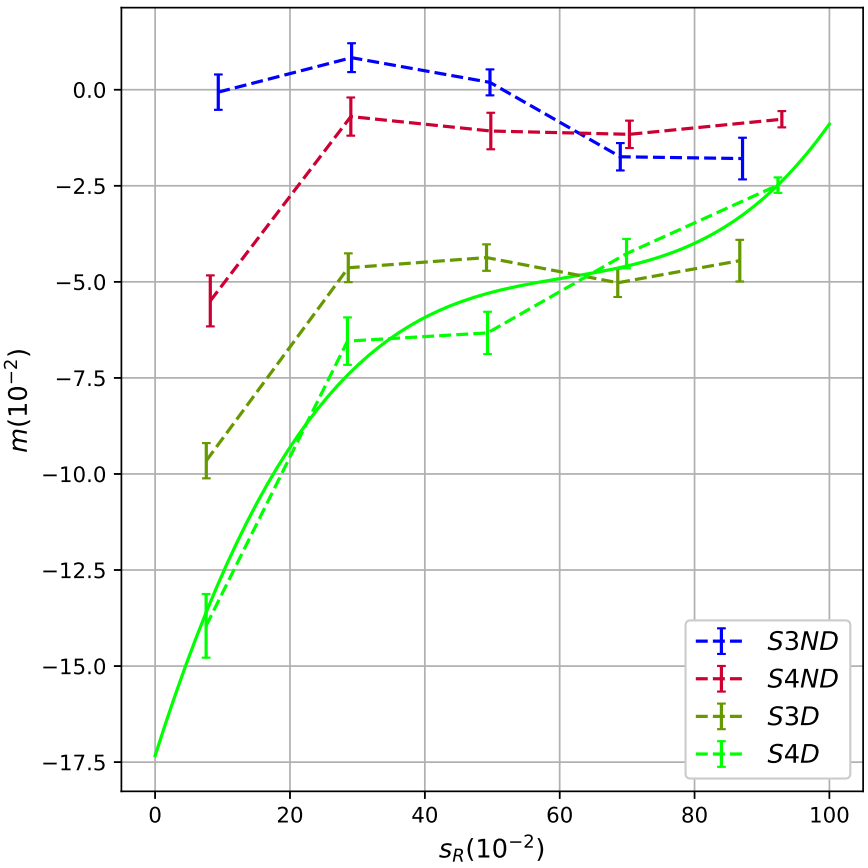

FIGURE 3.10: The multiplicative bias as a function of revised FPFS flux ratio. The solid lines are the third order polynomial fittings of the estimations that are denoted with points with errorbars. The hyper parameters are kept to the default values.

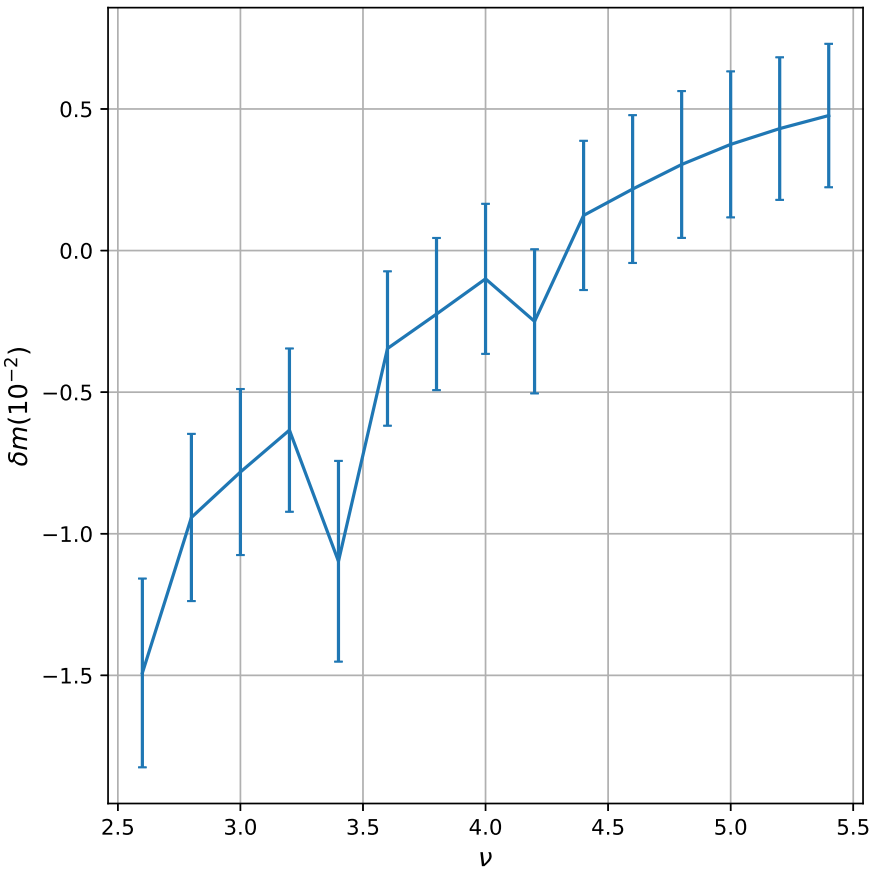

FIGURE 3.11: Calibration bias residual as a function of $\delta\ \nu$. The calibration factor obtained from the default setup ($\nu = 4$) is tested under conditions with setups deviate from the default setup. The x (y)-axis is the distortion of the hyper parameter (resulting bias residual).

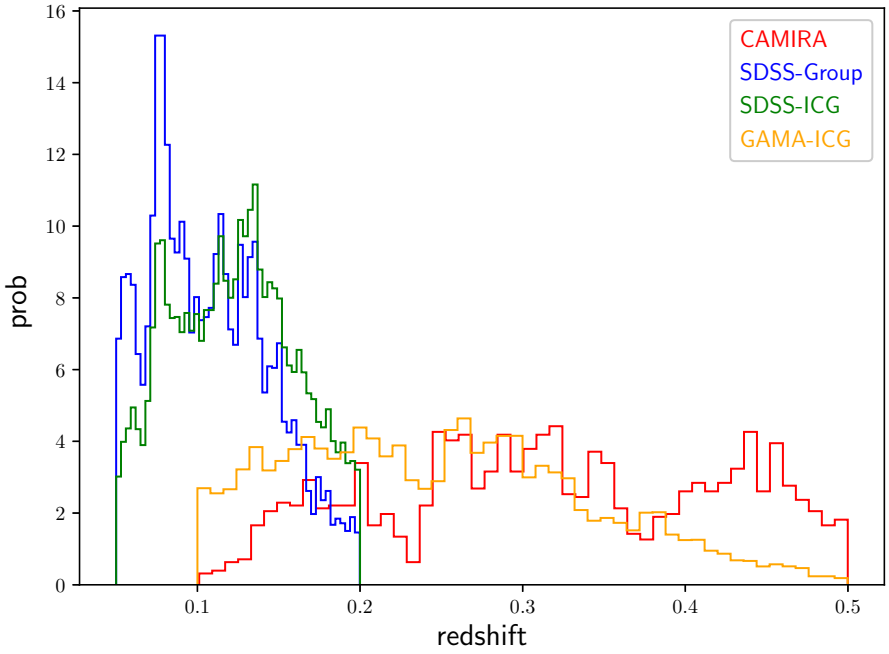

FIGURE 3.12: The redshift distribution of lens catalogs used for galaxy-galaxy lensing.

Note that here the noise bias is neglected since ν is set to a large number to make sure the noise bias is subdominant.

After the calibration, the final shear estimator is given by

$$\hat{g}_{1,2} = \frac{\langle e_{1,2} \rangle}{\langle (1 + m(s)) \mathcal{R}_{1,2} \rangle} \,. \tag{3.17}$$

3.3 Comparison with `reGauss`

This section serves to apply the calibrated `FPFS` shear estimator to the first-year HSC data, and compare with the first-year HSC shear catalog (`reGauss`) on the galaxy-galaxy measurements with different lens catalogs.

3.3.1 Lens Catalog

Observationally, a few different approaches have been adopted to select a sample of tracers of dark matter halos. The halo tracers include galaxy cluster catalogs detected with the red sequence cluster finder on photometric surveys (e.g. Oguri, 2014; Rykoff et al., 2014), galaxy group catalogs detected with halo-based group finder on spectroscopic/photometric data sets (e.g. Yang et al., 2007, 2021), and the isolated galaxies which are the locally brightest galaxies (ICG, e.g. Wang & White,

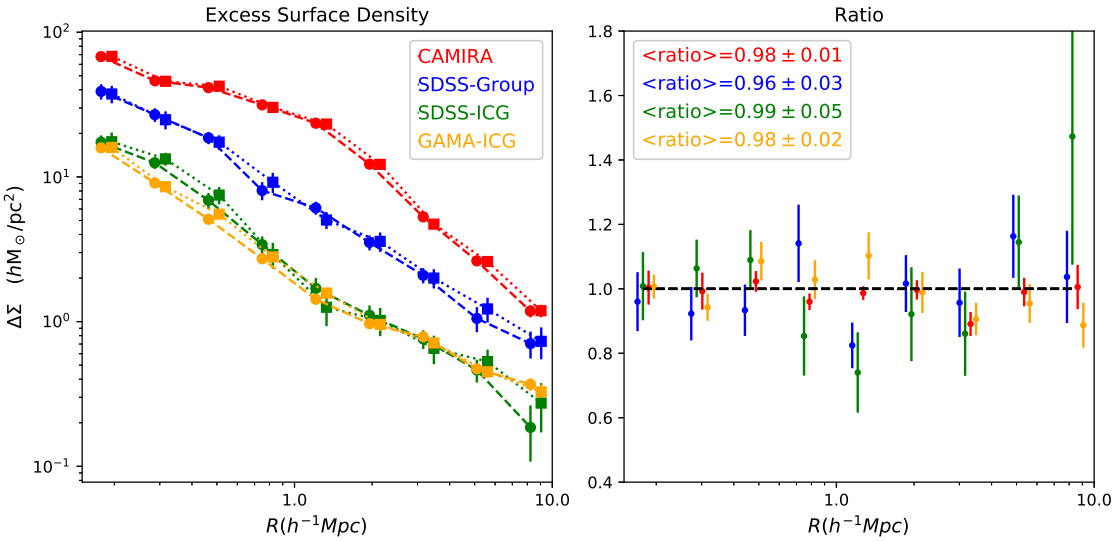

FIGURE 3.13: The left panel shows the ESDs measured by the `reGauss` shape catalog (dashed lines) and FPSF shape catalog (dotted lines) on different lens catalogs summarized in Section 3.3.1. The right panel shows the ratio between the ESDs measured by two shape catalogs.

2012; Wang et al., 2019).

In order to compare the `FPFS` shear catalog with the `reGauss` shear catalog (namely the fiducial HSC first-year shear catalog), galaxy-galaxy lensing measurements are conducted on different lens catalogs using both of the source galaxy shape catalogs. The lens catalogs include the SDSS ICG catalog (Wang & White, 2012), the GAMA (Driver et al., 2011) ICG catalog, the SDSS galaxy group catalog (Yang et al., 2007), and the HSC CAMIRA galaxy cluster catalog (Oguri et al., 2018). The selections of these four lens catalog are summarized follows:

- SDSS ICGs: Isolated central galaxies (ICGs) are defined as the brightest galaxy within an angular distance of 1 Mpc in transverse plane and 1000 km/s along the line-of-sight direction. The galaxies are selected from the NYU Value Added Galaxy Catalog (NYU-VAGC; Blanton et al., 2005), which is based on the 7the data release of the main spectroscopic galaxy sample of Sloan Digital Sky Survey (SDSS/DR7; Abazajian et al., 2009). In order to avoid mistakenly selecting galaxies with brighter physical companions, but the companions do not have proper spectroscopic redshift estimates due to the fiber collision, the photo-z catalog provided by Cunha et al. (2009) is used to compensate the selection. To be more specific, galaxy candidates are rejected if they have apparent companions within the aforementioned selection radius and with compatible photo-z compared to the candidate's spectroscopic redshift (for details, see Wang & White, 2012).

- GAMA ICGs: This galaxy sample is selected with the same selection criteria as SDSS ICGs, but the selection is applied to the public Galaxy And Mass Assembly (GAMA) DR3 spectroscopy catalog (Baldry et al., 2018), except that the further selection with photo-z is *not* applied since the effect of fiber collision in GAMA is less severe. Compared to the SDSS ICGs, the GAMA ICGs are about two magnitudes deeper.

- SDSS Group: The SDSS galaxy groups (Yang et al., 2007) are constructed with a halo-based group finder of Yang et al. (2005) on the spectroscopic galaxies in NYU-VAGC. This algorithm first identify potential group centers along with their group members with Friend-Of-Friend (FOF) algorithm (Davis et al., 1985). A characteristic luminosity for each tentative group is measured. By assuming a mass-to-light ratio, a tentative mass is subsequently assigned to each group. This assigned mass is used to estimate the size and velocity dispersion of the underlying halo hosting the galaxy group and update the group memberships. The group centers are iteratively updated as the group members are updated. The iteration continues until the galaxy group memberships do not change.

- HSC CAMIRA: The HSC CAMIRA galaxy clusters (Oguri et al., 2018) are identified with the CAMIRA algorithm of Oguri (2014) on the HSC first-year photometric galaxies (Aihara et al., 2018b). This algorithm is based on the Stellar Population Synthesis (SPS) model of Bruzual & Charlot (2003) to predict red-sequence galaxies' colors as a function of redshift for a set of bandpass filters. In order to improve the accuracy of the SPS model prediction, the prediction is calibrated using spectroscopic galaxies. The algorithm subsequently computes the likelihood for each galaxy of being in the red sequence as a function of redshift and construct a map of richness based on the computed likelihood. The CAMIRA clusters are identified as the peaks on the richness map. In addition, the center of the galaxy cluster is determined as the brightest cluster galaxy's center.

For SDSS group catalog and SDSS ICG catalog, lenses are selected in the redshift ranging from 0.05 to 0.2. GAMA ICGs and CAMIRA clusters are selected with $0.1 < z < 0.5$. The redshift distributions of these lens catalogs, after applying the redshift cuts, are shown in Figure 3.12.

TABLE 3.2: Selection of source galaxies according to photo-z .

photo-z cut	descriptions
mlz_std_best<3	The uncertainty of the best-fit photo-z estimate
mlz_conf_best>0.13	The confidence of the best-fit photo-z estimate
mlz_best<2.5	The best-fit photo-z estimate
$\int_{z_l+0.2}^{+\infty} P(z) > 0.95$	P(z) cut (e.g., Medezinski et al., 2018)

3.3.2 Excess Surface Density

A lens system with an excess surface density $\Delta\Sigma$ induces tangential shear distortions on background galaxy images, the signal of which at radius R to the lens center and redshift z_s is given by

$$\gamma_T(R, z_l, z_s) = \Delta\Sigma(R)\Sigma_{cr}^{-1}(z_l, z_s), \tag{3.18}$$

where the critical surface density Σ_{cr} is defined as

$$\Sigma_{cr}^{-1}(z_l, z_s) = \begin{cases} \frac{4\pi G}{c^2}(1+z_l)\frac{\chi_{ls}\chi_l}{\chi_s} & (z_l \leq z_s) \\ 0 & (z_l > z_s) \end{cases} . \tag{3.19}$$

Here χ denotes the comoving distance; G is the gravitational constant; and c is the speed of light. For simplicity, $\Sigma_{cr}^{-1}(z_l, z_s)$ is denoted as $\Sigma_{cr,ls}^{-1}$ in the following context. The probability density function (PDF) of the photometric redshifts $P(z_s)$, estimated with the `MLZ` algorithm (Tanaka et al., 2018), is used to calculate the expectation of $\Sigma_{cr,ls}^{-1}$, which is given by

$$\left\langle \Sigma_{cr,ls}^{-1} \right\rangle = \int_{z_l}^{+\infty} dz_s \Sigma_{cr}^{-1}(z_l, z_s) P(z_s) \, . \tag{3.20}$$

The relation between the expectation of tangential shear and the expectation of excess surface density (ESD) of lens is given by

$$\left\langle \gamma_T(R, z_l, z_s) \right\rangle = \left\langle \Delta\Sigma(R) \right\rangle \left\langle \Sigma_{cr}^{-1}(z_l, z_s) \right\rangle \, . \tag{3.21}$$

In the galaxy-galaxy lensing measurement, source galaxies are further selected according to their photometric redshift estimates following (Medezinski et al., 2018). The selection cuts on redshift estimates are summarized in Table 3.2.

The tangential ellipticity is defined as

$$e_T = -e_1 \cos(2\phi) - e_2 \sin(2\phi), \tag{3.22}$$

where ϕ is the angular position of the source galaxy respecting to the lens system' center in polar coordinates. After stacking a large number of lens systems in the lens catalog, the stacked ESD is can be estimated as

$$\left\langle \Delta\Sigma(R) \right\rangle = \frac{\sum_l \sum_s w_{ls} \left\langle \Sigma^{-1}_{cr,ls} \right\rangle^{-1} e_{T,s}}{\sum_l \sum_s (1+m_s) w_{ls} R_s}, \tag{3.23}$$

where w_{ls} is the weight for each lens-source pair. The optimal (inverse variance) weight is given by

$$w_{ls} = \left\langle \Sigma^{-1}_{cr}(z_l, z_s) \right\rangle^2 . \tag{3.24}$$

(Shirasaki & Takada, 2018)

Substituting equation (3.24) into equation (3.23), the estimator of ESDs is:

$$\left\langle \Delta\Sigma(R) \right\rangle = \frac{\sum_l \sum_s \left\langle \Sigma^{-1}_{cr,ls} \right\rangle e_{T,s}}{\sum_l \sum_s (1+m_s) \left\langle \Sigma^{-1}_{cr,ls} \right\rangle^2 R_s} . \tag{3.25}$$

The ESD estimates for the `reGauss` shear catalog and the `FPFS` shear catalog on these lens catalogs summarized in Section 3.3.1 are shown in Figure 3.13. The ESDs as functions of the comoving distance to the lens systems' centroids for two shear catalogs are shown in the *left panel* of Figure 3.13. The lower limit of the comoving radius is set to 0.1 Mpc/h since the measurement is very noisy because of the limited source galaxy number at the small scales. The error bars are estimated using 100 realizations of mock galaxy shear catalogs.

The right panel of Figure 3.13 shows the ratio between the measurements from the two shear catalogs. The ratio is defined as

$$\text{ratio} = \frac{\langle \Delta\Sigma_{FP} \rangle}{\langle \Delta\Sigma_{RG} \rangle}, \tag{3.26}$$

where $\langle \Delta\Sigma_{FP} \rangle$ and $\langle \Delta\Sigma_{RG} \rangle$ are the ESDs measured with the `FPFS` shear catalog and the `reGauss` shear catalog, respectively. The correlation between the ESDs measured with two shear catalogs is taken into account when assigning the statistical errors on the ratio estimations. This correlation is also estimated from the 100 realizations of mock galaxy shear catalogs for each lens catalog. In summary, the difference between two shear catalog on the galaxy-galaxy lensing is within the statistical uncertainty.

3.4 Summary

This section develops the Fourier Power Function Shapelet (FPFS) shear estimator, which reaches a sub-percent level accuracy when images of different galaxies do not overlap, namely in the absence of blending. The FPFS algorithm measures the polar shapelet modes (Massey & Refregier, 2005) on each galaxy image's Fourier power function after deconvolving the power function of point spread function (PSF). The scale of the Gaussian weighting kernel of the shapelet functions is set to be smaller than that of the PSF's Fourier power function to ensure that the noise on the large Fourier wave number is not boosted after projecting the deconvolved Fourier power function onto the shapelet function.

For deep ground-based cosmological surveys like Hyper Suprime-Cam (HSC), more than 50% of galaxies are blended. The FPFS shear estimator relies on external image simulations to calibrate a -5.8% multiplicative bias from blending. The FPFS shear estimator was applied to the first-year HSC coadds to create an independent shear catalog after calibrating the bias from blending on the FPFS shear estimator using the HSC-like image simulations Li et al. (2020). I found consistent results on galaxy-galaxy lensing with the `reGauss` shape catalog.

Several recently proposed algorithms have been proposed to reduce the multiplicative bias to a few parts in a thousand for isolated galaxies. Zhang et al. (2017); Li & Zhang (2021) show the latest development of `Fourier_Quad`. This method determines two components of shear by re-symmetrizing the PDF of two spin-2 moments which are measured from the power function of galaxy's Fourier transform. This re-symmetry method only uses linear observable measured from Fourier power function to construct shear estimator so it is not influenced by noise bias. However, `Fourier_Quad` has not provided solution to selection bias.

Bayesian Fourier Domain (`BFD`; Bernstein & Armstrong, 2014; Bernstein et al., 2016) uses Bayesian formalism to measure shear from the full Bayesian posterior so the formalism is not influenced by noise bias. `BFD` is the first method which provides solution to selection bias. `BFD` requires noiseless distribution of galaxy population over parameter space as a prior which should be constructed from deep exposures.

Metacalibration (Huff & Mandelbaum, 2017; Sheldon & Huff, 2017) proposes to find the shear response for ellipticity defined by any algorithm through adding artificial shear to each observed galaxy. Shear can be inferred by averaging over ellipticity and response of a large ensemble of galaxies. Metacalibration adds inversely sheared noise image to galaxy images to remove noise bias and it also provides solution to selection bias. Several galaxy image simulations using realistic galaxy images (Sheldon & Huff, 2017) have proved that the multiplicative bias, including both noise bias and selection

bias, for METACALIBRATION is below 1×10^{-3}. Moreover, METACALIBRATION has been successfully applied to DES survey (Zuntz et al., 2017). Therefore, METACALIBRATION is believed to be the most promising shear estimator in the weak lensing community.

Compared to these methods, the FPFS estimator does not involve complicated statistical procedure and it does not need prior information from deep exposures. Furthermore, FPFS shear estimator does not rely on heavy image manipulations. Since only four shapelet modes are required to construct the FPFS shear estimator, our algorithm is computationally much faster.

4

Three-dimensional (3D) Weak Lensing Mass Map

Contents

This chapter reconstructs three-dimensional (3D) mass map from weak lensing shear estimations observed from distant galaxy images that was discussed in Chapter 2.

First, the mass map inversion problem is summarized in Section 4.1. Second, a new method is proposed to reconstruct the mass maps in Section 4.2. The mass map is modelled as a summation of basis function in the model dictionary introduced in Section 4.2.1). In addition, sparsity prior is adopted in the mass map reconstruction (Section 4.2.2). Then, the new method is tested on halo simulations described in Section 4.3, and the results are shown in Section 4.4. We compare the newly proposed method with existing methods in Section 4.5

4.1 The 3D mass inversion problem

The lensing shear field γ observed from background galaxy images is related to the foreground density contrast field, defined as $\delta = \rho_{\rm m}/\bar{\rho_{\rm m}} - 1$ via a linear transform shown as follows:

$$\gamma = \mathbf{T} \cdot \delta + \epsilon, \tag{4.1}$$

where ϵ is the shear measurement error caused by the random orientation of galaxy shapes (shape noise) and the sky variance (photon noise). The matrix operator $\mathbf{T} = \mathbf{P}\cdot\mathbf{Q}$ includes both the physical lensing effect, which is denoted by a matrix operator $\mathbf{Q}$, and also the observational systematic effects, which is denoted by a matrix operator $\mathbf{P}$. The weak lensing operator $\mathbf{Q}$ will be given out in Section 4.1.1, and the systematics operator $\mathbf{P}$ will be given out in Section 4.1.2.

4.1.1 Weak gravitational lensing

The lensing transform operator, mapping the foreground density contrast field at z_l to the background lensing shear field at z_s, can be expressed as

$$\mathbf{Q} = \int_0^{z_s} dz_l \, K(z_l, z_s) \int d^2\theta' D(\vec{\theta} - \vec{\theta'}), \tag{4.2}$$

$K(z_l, z_s)$ is termed the lensing kernel (Bartelmann & Schneider, 2001), which is given by

$$K(z_l, z_s) = \begin{cases} \frac{3H_0\Omega_{\rm m}}{2c} \frac{\chi_l \chi_{sl}(1+z_l)}{\chi_s E(z_l)} & (z_s > z_l), \\ 0 & (z_s \leq z_l), \end{cases} \tag{4.3}$$

where $E(z)$ is the Hubble parameter as a function of redshift, in units of H_0;

$$D(\vec{\theta}) = -\frac{1}{\pi}(\theta_1 - i\theta_2)^{-2} \tag{4.4}$$

is the Kaiser-Squares kernel (Kaiser & Squires, 1993), which decays proportional to the inverse-square of the distance. Here $\theta_{1,2}$ are the two components of the angular position vector $\vec{\theta}$.

The *top panel* of Figure 4.1 shows the lensing kernels as a function of source redshift lens redshifts fixed as different values. The *bottom panel* of Figure 4.1 shows the correlation matrix between the lensing kernels. As shown, the lensing kernels at each lens redshift is highly non-local. Furthermore, the lensing kernels of different lens redshifts are highly correlated. As a result, the column vectors that constitute the matrix $\mathbf{T}$ are strongly correlated, which makes it challenging to reconstruct mass

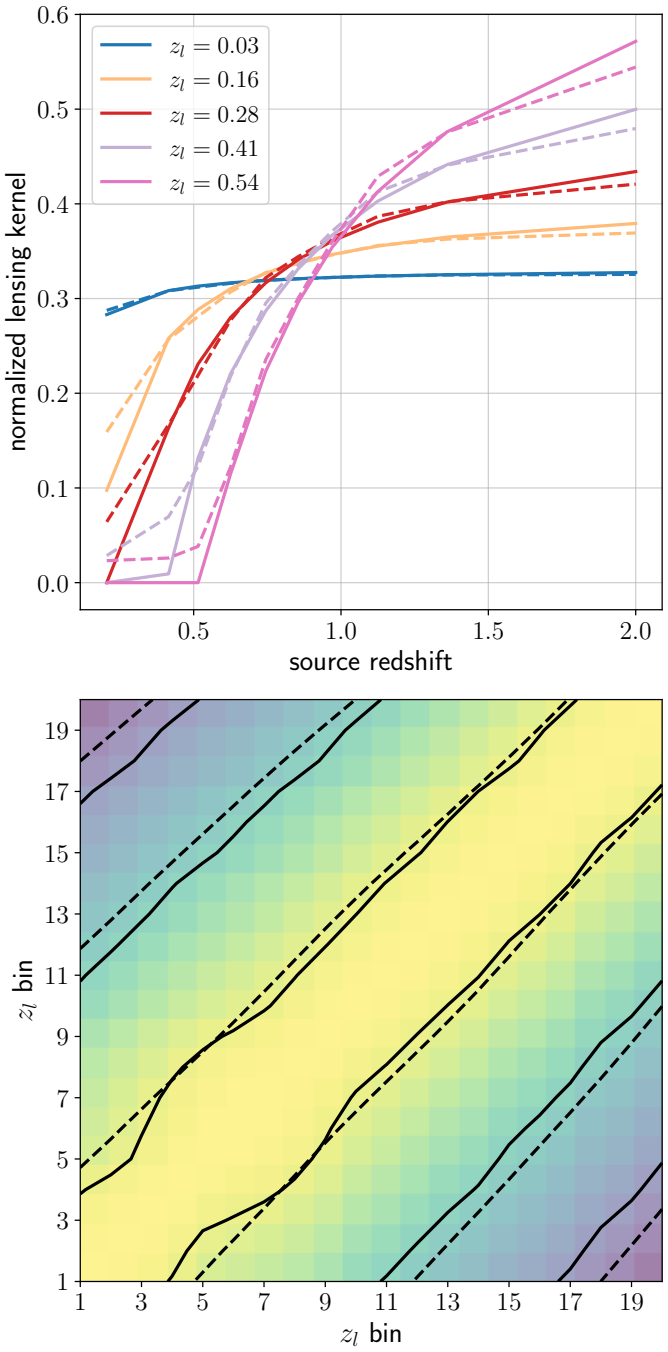

FIGURE 4.1: *Top panel* shows the normalized lensing kernels as a function of source redshift with lens redshifts fixed. The solid lines are the kernels for the source galaxies with precise spectroscopic redshifts, whereas the dashed lines are for source redshifts with HSC-like photometric redshift errors. *Bottom panel* shows the correlation matrix between the lensing kernels of different lens redshifts. The diagonal terms are normalized to 1. The color map is the correlation matrix for spectroscopic redshift. The solid (dashed) contours show the result for the lensing kernel of spectroscopic (photometric) redshift at levels 0.7, 0.85, and 0.98.

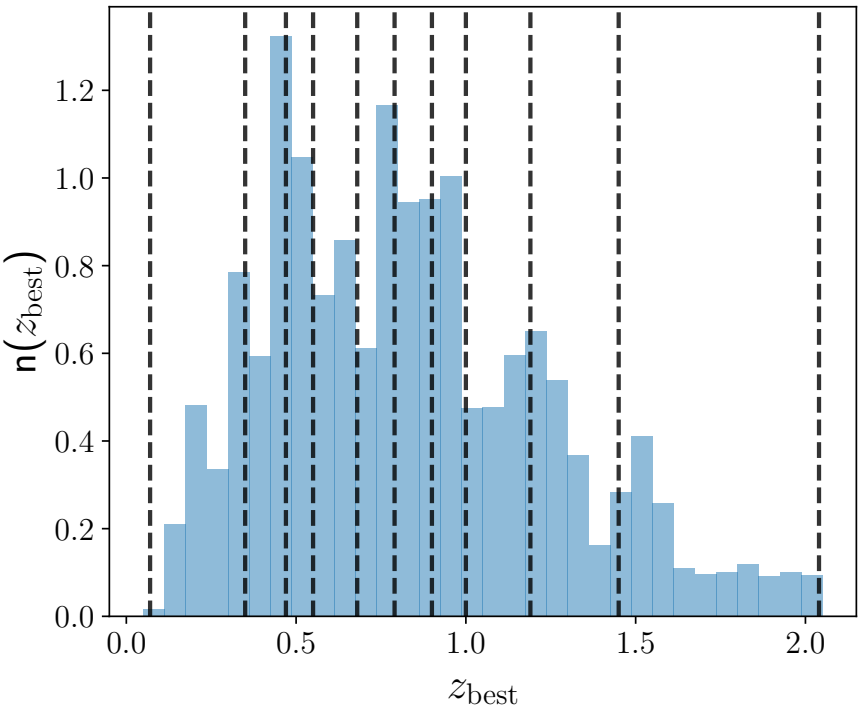

FIGURE 4.2: The blue histogram shows the normalized number distribution of the best-fit photo-z (MLZ) estimates from tract 9347 of the first-year HSC data. An equal-number binning scheme is adopted to divide the source galaxies into a total of 10 redshift bins that are indicated by the vertical dashed lines.

maps with high resolution in the line-of-sight direction.

4.1.2 Systematics

The observed shear is different from the true, physical shear owing to a variety of systematic effects in real observations. This section serves to discuss the influence of several major systematics on the lensing shear measurement, and describe the corresponding transform operator by decomposing into three parts of **R** (photometric redshift uncertainties), **W** (smoothing), and **M** (masking).

4.1.2.1 Photometric redshift Uncertainty

Since photometric redshifts (photo-z) are estimated with a limited number of broad optical and near-infrared bands in the current generation of weak lensing surveys (e.g., 9 bands are used for KIDS+VIKING survey (Hildebrandt et al., 2020), 5 bands for DES survey and HSC survey) the photo-z estimation suffers from considerable statistical uncertainties, compared to the high-precision spectroscopic redshift (spect-z) estimation.

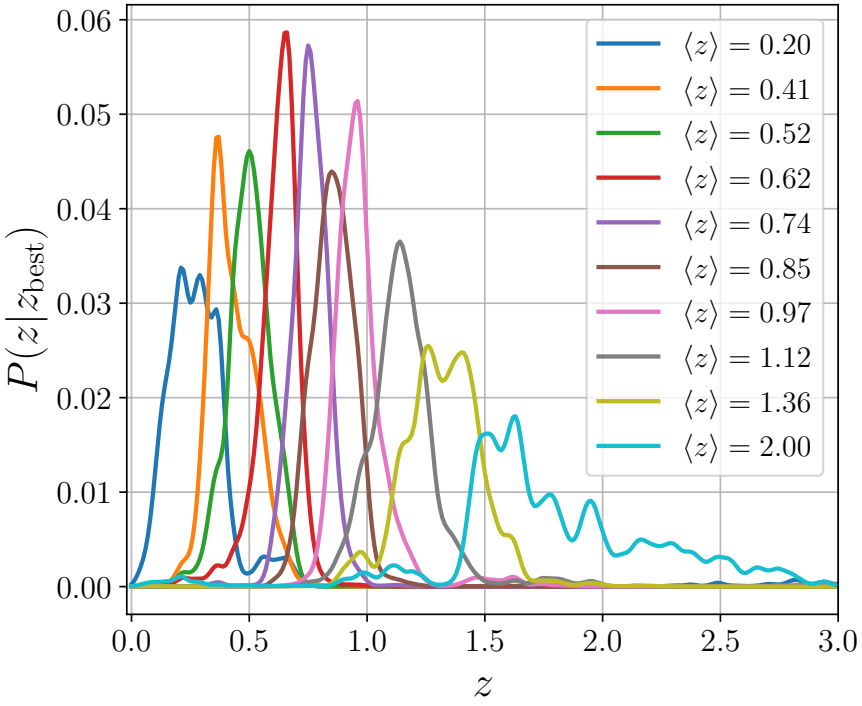

FIGURE 4.3: The average posterior PDF of `MLZ` in 10 source redshift bins with boundaries defined by the vertical dashed lines in Figure 4.2.

Figure 4.2 shows the histogram of the best-fit estimates of the Machine Learning for photo-Z (`MLZ`; Carrasco Kind & Brunner, 2013) algorithm[1] for galaxies in tract 9347 from the photo-z catalog (Tanaka et al., 2018) of the first-year HSC data release (Aihara et al., 2018b). Note that the HSC data is divided into rectangular regions called tracts covering approximately $1.7 \times 1.7\,\mathrm{deg}^2$, and each tract is broken into 9x9 patches. The galaxies are divided into ten redshift bins according to the best-fit estimates. Figure 4.3 shows the stacked mean posterior PDF for galaxies in each redshift bin.

In the presence of photo-z uncertainties, a source galaxy with a best-fit photo-z estimate z_s has a posterior probability $P(z|z_s)$ of being actually located at redshift z. This means that there is a possibility $P(z|z_s)$ that the concerning galaxy is actually distorted by the lensing shear at redshift z. The photo-z uncertainty hence *statistically* smears the lensing kernels, which is modelled by a smearing operator:

$$\mathbf{R} = \int dz_s P(z|z_s)\,. \tag{4.5}$$

Figure 4.1 shows the lensing kernels and their correlations in the case with photo-z

[1] https://github.com/mgckind/MLZ

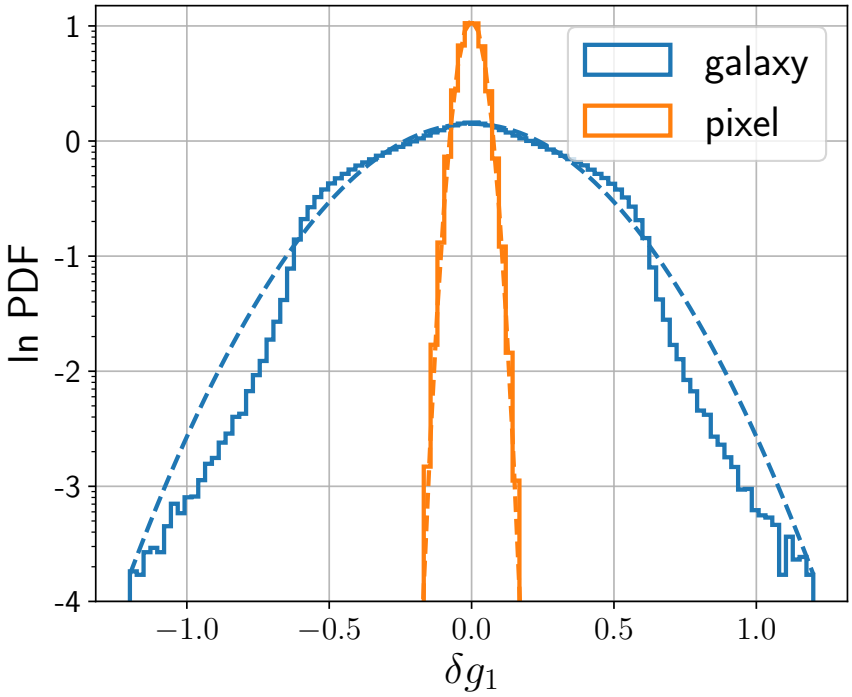

FIGURE 4.4: The solid blue (orange) line shows the histogram of the HSC-like shear measurement error on the first component of shear g_1 on individual galaxy (pixel) level. The dashed lines are the best-fit Gaussian distributions to the corresponding histograms.

uncertainties that are demonstrated in Figure 4.3. As shown, the photo-z uncertainty only slightly increases the correlations between lensing kernels at different lens plane.

4.1.2.2 Smoothing

Since the source galaxies are not uniformly distributed in the sky due to substantial fluctuations in the number density, in order to pixelate shear measurements onto a regular grid, the shear measurements are first smoothed by a smoothing kernel. After pixelation, the fast Fourier transform (FFT) can be directly conducted on the transverse plane in each redshift bin to compute the convolution operations shown in Equation (4.1). Additionally, smoothing reduces bias arising from the aliasing effect in the pixelation process since the smoothing kernel reduces the amplitude of the shear signal at high frequency. The details of the pixlation is described in Section 4.2.2.1.

The lensing shear measured from galaxy images is convolved with a 3D smoothing

kernel denoted by $W(\vec{\theta}, z)$. The shear measurements after smoothing is given by

$$\gamma_{\rm sm}(\vec{\theta}, z) = \frac{\sum_i W(\vec{\theta} - \vec{\theta}_i, z - z_i)\gamma_L(\vec{\theta}_i, z_i)}{\sum_i W(\vec{\theta} - \vec{\theta}_i, z - z_i)}, \tag{4.6}$$

where z_i refers to the photometric redshift; θ_i refers to the transverse position; $\gamma_L(\theta_i, z_i)$ refers to the shear measurement before the smoothing from the i-th galaxy in the galaxy ensemble.

I will focus on the situation that the smoothing kernel $W(\vec{\theta}, z)$ can be decomposed into a transverse component $W_t(\vec{\theta})$ and a line-of-sight component $W_l(z)$:

$$W(\vec{\theta}, z) = W_t(\vec{\theta})\, W_l(z)\,. \tag{4.7}$$

An isotropic 2D Gaussian kernel and a 1D top-hat kernel are used to smooth the shear field in the transverse plane and in the line-of-sight direction, respectively. These components are given by

$$\begin{aligned} W_t(\vec{\theta}) &= \frac{1}{2\pi\beta^2}\exp\left(-\frac{|\vec{\theta}|}{2\beta^2}\right), \\ W_l(z) &= \begin{cases} 1/\Delta z & (|z| < \Delta z/2), \\ 0 & \text{othewise}, \end{cases} \end{aligned} \tag{4.8}$$

The RMS of the Gaussian kernel is set to $\beta = 1.5'$ in this section. The smoothing kernel is, by definition, normalized as

$$\int {\rm d}^3 r\, W(\vec{r}) = 1\,. \tag{4.9}$$

With the assumption that the galaxy number distribution varies slowly at the smoothing scale, the smoothed shear can be written into

$$\gamma_{\rm sm} = \mathbf{W}\cdot\gamma_L, \tag{4.10}$$

where $\mathbf{W}$ is the smoothing operator defined as

$$\mathbf{W} = \int {\rm d}^3 r'\, W(\vec{r} - \vec{r'})\,. \tag{4.11}$$

The smoothed shear field is pixelated onto a regular grid. In this chapter, the pixel width is set to $1'$. Another widely used scheme is to average the shear measurements in each pixel, which is equivalent to resampling the shear field smoothed with a 3D

top-hat kernel with the same scale as the pixels.

In order to see the effect of smoothing clearly, the histograms of the statistical shear measurement errors due to shape noise and sky variance for the galaxies in tract 9347 of the first-year HSC shear catalog (Mandelbaum et al., 2018b) are demonstrated as follows. Figure 4.4 compares the error on an individual galaxy basis and that of individual pixels after the smoothing and pixelation procedures described in this section. As shown, the RMS on the individual pixel errors is much smaller than that on the individual galaxy level thanks to the smoothing. Moreover, even though the shear measurement error on the individual galaxy level does not follow a Gaussian distribution, the error after smoothing and pixelation is well described by a Gaussian distribution, which is simply explained by the central limit theorem.

4.1.2.3 Masking

In real observations, shear measurements can be performed in a finite sky region, and the boundaries often have complicated geometries. In addition, many isolated sub-regions near the bright stars are masked out to mitigate the bias due to the light from bright stars on shear estimations.

The masking window function is defined as

$$M(\vec{r}) = \begin{cases} 1 & n_{\rm sm} \geq 1, \\ 0 & \text{otherwise}, \end{cases} \tag{4.12}$$

where $n_{\rm sm}$ is the smoothed galaxy number density, and the masking operator as

$$\mathbf{M} = \int \mathrm{d}^3 r' \, M(\vec{r'}) \delta_D(\vec{r} - \vec{r'}), \tag{4.13}$$

where $\delta_D(\vec{r})$ is 3D Dirac delta function.

In summary, after taking into account the systematics discussed in previous Sections 4.1.2.1–4.1.2.3, the transform operator of systematics is given by

$$\mathbf{P} = \mathbf{M} \cdot \mathbf{W} \cdot \mathbf{R} \,. \tag{4.14}$$

4.2 Method

4.2.1 Model Dictionary

Assumptions on the density contrast field are incorporated into the mass map reconstruction to improve SNR and resolution of the reconstructed mass maps. Here the

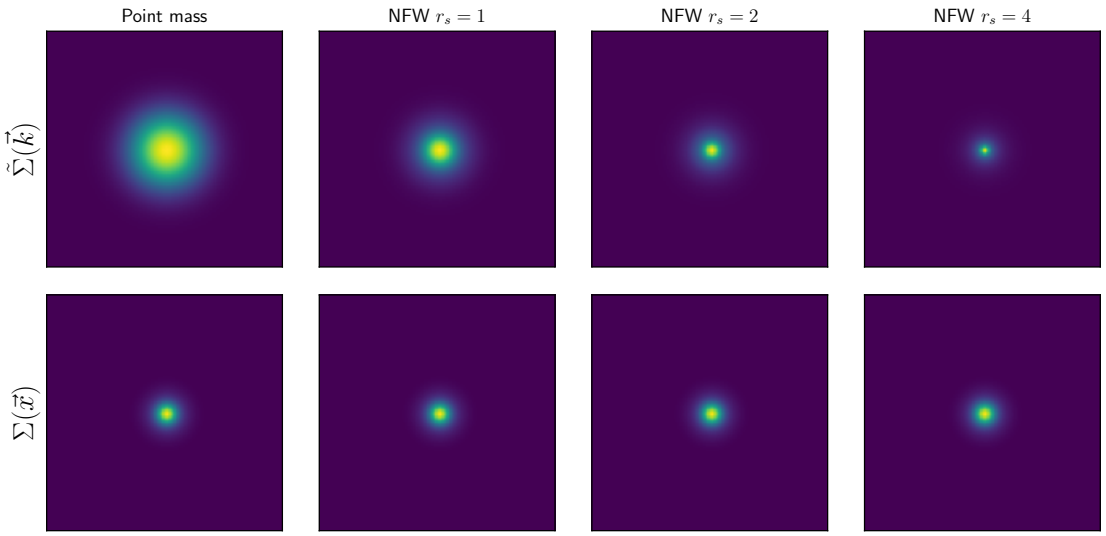

FIGURE 4.5: The normalized 2D profiles of the smoothed basis "atoms". The pixel size is $1'$.The leftmost column is the point mass atom, and the other columns show the NFW atoms with different scale radii (in unit of pixel) as indicated. The upper (lower) panels shows the basis atoms in Fourier (configuration) space. The two-dimensional profiles are smoothed using a Gaussian kernel with a 1.5 pixel width.

density contrast field is modelled as a sum of basis atoms in a "dictionary":

$$\delta = \mathbf{\Phi} \cdot x, \tag{4.15}$$

where $\mathbf{\Phi}$ is the matrix operator transforming from the projection coefficient vector x to the density contrast field δ. The column vectors of $\mathbf{\Phi}$ are the basis "atoms" of the model dictionary, and the atoms are denoted as ϕ_s.

According to cosmological N-body simulations, dark matter is concentrated in roughly spherical "halos" with the NFW density profile in the standard cosmological model(Navarro et al., 1997). Motivated by this fact, a model dictionary constructed by NFW atoms with N typical scale radii r_s $(s = 1, ..., N)$ in comoving coordinates can be used to model the density contrast field. The basis atom in the dictionary has the NFW surface density profile on the transverse plane (Takada & Jain, 2003) and the Dirac δ function in the line-of-sight direction. Note that, following Leonard et al. (2014), the size of halos along the line-of-sight is neglected as the resolution scale of the reconstruction is much larger than the halos.

The multi-scale NFW atom is defined as

$$\phi_s(\vec{r}_\theta, z) = \frac{f}{2\pi r_s^2} F(|\vec{r}_\theta|/r_s)\, \delta_D(z), \tag{4.16}$$

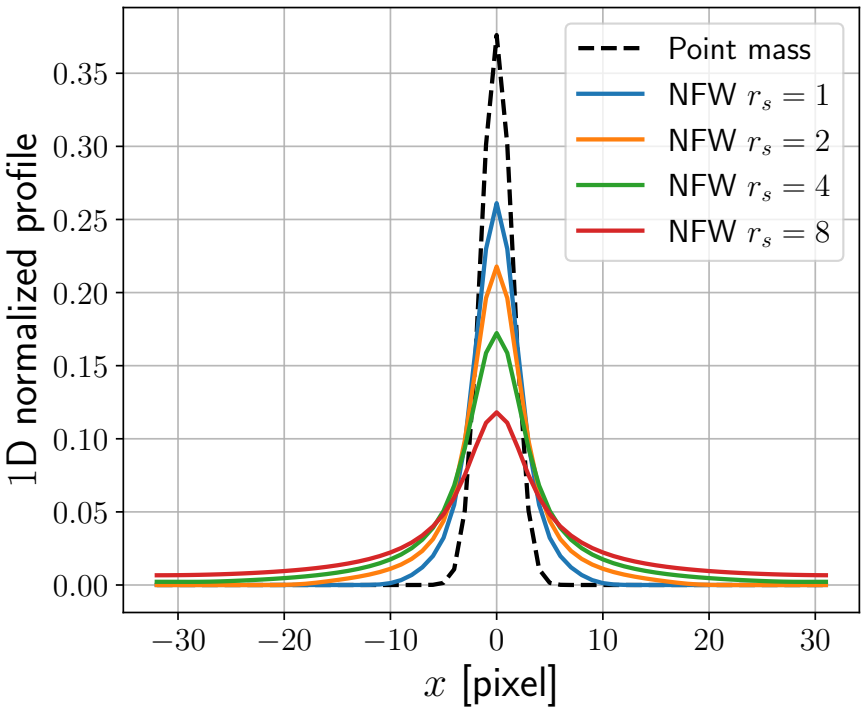

FIGURE 4.6: The normalized one-dimensional (1D) profiles of smoothed basis atoms, which are slices of the corresponding 2D profiles (shown in Figure 4.5) at $y = 0$. The scale radii shown in the figure are in unit of pixel.

where $\vec{r}_\theta$ is the projection of the comoving position on the transverse plane,

$$F(x) = \begin{cases} -\frac{\sqrt{c^2-x^2}}{(1-x^2)(1+c)} + \frac{\operatorname{arccosh}\left(\frac{x^2+c}{x(1+c)}\right)}{(1-x^2)^{3/2}} & (x < 1), \\ \frac{\sqrt{c^2-1}}{3(1+c)}(1+\frac{1}{c+1}) & (x = 1), \\ -\frac{\sqrt{c^2-x^2}}{(1-x^2)(1+c)} + \frac{\arccos\left(\frac{x^2+c}{x(1+c)}\right)}{(x^2-1)^{3/2}} & (1 < x \leq c), \\ 0 & (x > c)\,. \end{cases} \tag{4.17}$$

$f = 1/[\ln(1+c) - c/(1+c)]$, and c is the halo concentration. For simplicity, the concentration parameter is fixed to $c = 4$ for the NFW atoms in the NFW dictionary. A hard truncation on the NFW profile is adopted at a radius equals $c\,r_s$. Studying the influence of different truncation forms (Oguri & Hamana, 2011) on the mass map reconstruction is left to the future work.

Compared to other model dictionaries, the NFW dictionary is motivated by a physical consideration on the clumpy mass distribution in the Universe. Moreover, the multi-scale NFW atoms are built up in comoving coordinates. This setup takes into account of the scale difference in the angular separation coordinates due to the difference in the distances between the halos (at different redshifts) and the observer. The corresponding NFW atom in the angular separation coordinates is

$$\phi_s(\vec{\theta}, z) = \frac{f\chi^2(z)}{2\pi r_s^2}\, F(|\vec{\theta}|\chi(z)/r_s)\, \delta_D(z), \tag{4.18}$$

where $\chi(z)$ is the comoving distance to redshift z.

The transform from the projection coefficient vector to the density contrast field of Equation (4.15), for the NFW dictionary, is written as

$$\delta(\vec{r}) = \sum_{s=1}^{N} \int d^3r' \phi_s(\vec{r} - \vec{r'}) x_s(\vec{r'})\,. \tag{4.19}$$

In order to simplify the notation, the projection coefficient vectors of multiple scales are compressed into a single column vector:

$$x = \begin{pmatrix} x_0 \\ x_1 \\ \cdots \\ x_N \end{pmatrix}, \tag{4.20}$$

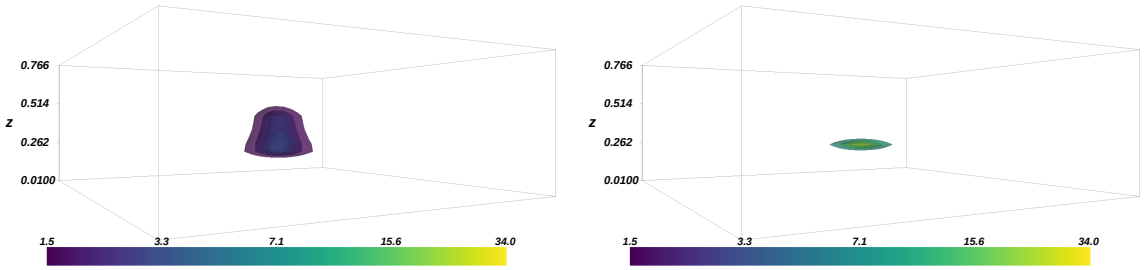

FIGURE 4.7: The density map reconstruction with LASSO (left) and with the adaptive LASSO (right) algorithm. The z-axes are for redshift. The color bars indicate the values of reconstructed density contrast fields. The mass of halo is $M_{200} = 10^{15}\ h^{-1}M_{\odot}$, and its redshift is $z = 0.35$. Shear measurement errors and photo-z uncertainties are not considered in the simulation.

and the dictionary transform operator is written into a single row vector:

$$\mathbf{\Phi} = \left(\int \mathrm{d}^3 r\, \phi_0(\vec{r}) \;\; \int \mathrm{d}^3 r\, \phi_1(\vec{r}) \;\; ... \;\; \int \mathrm{d}^3 r\, \phi_N(\vec{r}) \right). \tag{4.21}$$

A dictionary with the point mass atoms is introduced for an additional comparison. The point mass atoms are represented by the 3D Dirac function as

$$\phi_{\mathrm{PM}}(\vec{\theta}, z) = \delta_{\mathrm{D}}(\theta_1)\ \delta_{\mathrm{D}}(\theta_2)\ \delta_{\mathrm{D}}(z)\,. \tag{4.22}$$

The 2D profiles of the NFW atoms and the point mass atom on the transverse plane are shown in Figure 4.5; The corresponding 1D sliced profiles are plotted in Figure 4.6. In these figures, the profiles are smoothed with a Gaussian kernel (see Section 4.1.2.2) and pixelated on the regular grids (see Section 4.2.2.1).

The forward transform operator $\mathbf{A} = \mathbf{P} \cdot \mathbf{Q} \cdot \mathbf{\Phi}$ is introduced to simplify the notation, where $\mathbf{P}$ is systematic operator and $\mathbf{Q}$ is the physical lensing operator. Using Equations (4.1) and (4.15), the transform from the coefficient vector x to the observed lensing shear field is given by

$$\gamma = \mathbf{A} \cdot x + \epsilon\,. \tag{4.23}$$

4.2.2 Sparsity Prior

The projection coefficients can be estimated by optimizing a penalized loss function. An estimator is generally defined as

$$\hat{x} = \arg\min_{x} \left\{ \frac{1}{2} \left\| (\gamma - \mathbf{A}x) \right\|_2^2 + \lambda C(x) \right\}, \tag{4.24}$$

where $_{\Sigma}\left\|(\gamma - \mathbf{A}x)\right\|_2^2$ refers to the l^2 norm of residuals weighted by the inverse of the covariance matrix Σ of the shear measurement error, which measures the difference between the prediction and the data, and $C(x)$ is the "penalty term" incorporating prior knowledge of the distribution of parameter x. That is, the estimation with the "penalty" term prefers parameters that are able to describe the observation with a specified prior information. The penalty parameter λ adjusts the relative weight between the data and the prior assumption in the optimization process. There are two popular choices of penalties—one is the l^2 ridge penalty ($C = \|x\|_2^2$) and the other is the l^1 LASSO penalty ($C = \|x\|_1^1$)–ensuring that the loss function is convex; therefore the maximum likelihood can be achieved with a gradient descent algorithm.

A derivative version of the l^2 penalty (also known as LASSO penalty)—the adaptive LASSO penalty —is adopted in the new method. The pixelation of the shear measurements and the projection parameter field is shown in Section 4.2.2.1. The column vectors of the forward transform matrix is then normalized in Section 4.2.2.2. The loss function is subsequently introduced in Section 4.2.2.3 with the adaptive LASSO penalty. Finally, Section 4.2.2.4 optimizes of the loss function in with the FISTA algorithm (Beck & Teboulle, 2009).

4.2.2.1 Pixelation

The shear field is pixelated on $N_x \times N_y \times N_z$ grids, where N_x and N_y are the number of pixels of the two orthogonal axes of the transverse plane, and N_z is the number of pixels in the line-of-sight direction. The smoothed shear measurements recorded on the pixel are denoted by γ_α, where the index α is in the range: $1 \leq \alpha \leq N_x \times N_y \times N_z$. In the transverse plane, the grids are equally spaced with a pixel size of $1'$; whereas, in the line-of-sight direction, an equal galaxy number binning scheme is adopted as demonstrated in Figure 4.2.

Similarly, the projection coefficient vector x is pixelated onto an $N_x \times N_y \times N_l$ grid. Compared to the pixelation of the shear field, in the line-of-sight direction, the projection coefficient vector is pixelated in *equal spacing* in the redshift range: $0.01 \leq z_l < 0.85$. Here, N_l is used to denote the number of the lens planes and x_β to denote the projection field element with index $1 \leq \beta \leq N_x \times N_y \times N_l \times N$, where the last N is the number of NFW dictionary frames representing different physical scale radii. The corresponding pixelated elements of the forward transform matrix $\mathbf{A}$ is denoted as $A_{\alpha\beta}$.

4.2.2.2 Normalization

The l^2 norm of the i-th column vector of $\mathbf{A}$ weighted by the inverse of the noise covariance matrix is defined as

$$\mathcal{N}_i = (\Sigma^{-1})_{\alpha\beta} A_{i\alpha} A_{i\beta} \,. \tag{4.25}$$

The column vectors have different weighted l^2 norms mainly due to the difference in lensing efficiency for halos at different redshifts. As the FISTA algorithm based on gradient descent algorithm, which will be used to optimize the loss function in Section 4.2.2.4, takes each column vector equally, the column vectors are normalized before performing the density map reconstruction to improve the convergence speed of the gradient descent iteration. The normalized forward transform matrix and projection parameters are given by

$$\begin{aligned} A'_{\alpha\beta} &= A_{\alpha\beta} / \mathcal{N}_\alpha^{\frac{1}{2}}, \\ x'_\beta &= x_\beta \mathcal{N}_\beta^{\frac{1}{2}} \,. \end{aligned} \tag{4.26}$$

4.2.2.3 Adaptive LASSO

As known, the LASSO algorithm uses l^1 norm of the projection coefficient vector as the penalty term. The LASSO estimator is defined as

$$\hat{x'}^{\mathrm{LASSO}} = \arg\min_x \left\{ \frac{1}{2} \Sigma \left\| (\gamma - \mathbf{A}' \cdot x') \right\|_2^2 + \lambda \left\| x' \right\|_1^1 \right\}, \tag{4.27}$$

where $\|\bullet\|_1^1$ and $\|\bullet\|_2^2$ are the l^1 norm and l^2 norm, respectively. λ is the penalty parameter for the LASSO estimation.

The LASSO algorithm searches and selects the parameters that are relevant to the measurements, and simultaneously estimates the values of the selected parameters. In the absence of noise, with the increase of the penalty parameter, the LASSO algorithm selects the relevant modes more consistently but with a increased shrinkage of selected modes. A question arises here: Can LASSO perform a consistent selection and a accurate estimation simultaneously, by simply tunning the penalty parameter? Unfortunately, it has been shown by Zou (2006) that if the column vectors of the forward transform matrix $\mathbf{A}'$ are highly correlated, the LASSO algorithm cannot perform a consistent selection and an accurate estimation owing to the shrinkage in the LASSO regression. Note that, for the weak lensing density map reconstruction problem, the column vectors are highly correlated even in the absence of photo-z uncertainties since the lensing kernels for lenses at different redshifts are highly

correlated as shown in Figure 4.1.

Figure 4.7 shows an example reconstruction results for a single halo with mass $M_{200} = 10^{15}\ h^{-1}M_{\odot}$ at redshift 0.35[2]. The shear measurement and photo-z uncertainties are not included in this simulation. Significant smearing of the mass distribution with the LASSO algorithm is found and demonstrated in the left panel of Figure 4.7. As shown, the LASSO algorithm cannot accurately determine the consistent mass distribution in redshift, and the reconstructed map suffers from smearing in the line-of-sight direction even in the absence of noises.

In order to overcome the problem, Zou (2006) proposed the adaptive LASSO algorithm, which uses adaptive weights to penalize different projection coefficients in the l^1 penalty. To be specific, the adaptive LASSO algorithm performs a two-steps process. In the first step, the standard (non-adaptive) LASSO is used to estimate the parameters. Let us denote the preliminary estimation as $\hat{x'}_{\rm LASSO}$. In the second step, the preliminary estimate is used to calculate the non-negative weight vector for penalization as

$$\hat{w} = \frac{1}{\left|\hat{x'}_{\rm LASSO}\right|^{\tau}}, \tag{4.28}$$

where the hyper-parameter τ is set to 2. The adaptive LASSO estimator is then given by

$$\hat{x'} = \arg\min_{x'} \left\{ \frac{1}{2}_{\Sigma}\left\|(\gamma - \mathbf{A'}\cdot x')\right\|_2^2 + \lambda_{\rm ada}\left\|\hat{w}\circ x'\right\|_1^1 \right\}, \tag{4.29}$$

where "$\circ$" is the element-wise product, and $\lambda_{\rm ada}$ is the penalty parameter for the adaptive LASSO, which does not necessarily need to be the same as the penalty parameter for the preliminary LASSO estimation: λ. To simplify the equations in the following, the loss function is rewritten with the Einstein notation as follows:

$$\begin{aligned} L(x') = &\frac{1}{2}(\Sigma^{-1})_{\alpha\beta}(\gamma^*_{\alpha} - A'^*_{\alpha i}x'_i)(\gamma_{\beta} - A'_{\beta j}x'_j) \\ &+ \lambda_{\rm ada}\hat{w}_{\beta}\left|x'_{\beta}\right|, \end{aligned} \tag{4.30}$$

and the quadruple term in the loss function as

$$G(x') = \frac{1}{2}\Sigma^{-1}_{\alpha\beta}(\gamma^*_{\alpha} - A'^*_{\alpha i}x'_i)(\gamma_{\beta} - A'_{\beta j}x'_j)\,. \tag{4.31}$$

4.2.2.4 FISTA

Beck & Teboulle (2009) propose the Fast Iterative Soft Thresholding Algorithm (FISTA) to optimize the LASSO loss function. Since the loss functions of the pre-

[2]The critical over-density is set to 200, and use M_{200} to denote the halo mass.

liminary LASSO and the adaptive LASSO differ only in their penalty terms, both of which are convex functions, it is straightforward to apply FISTA to solve the adaptive LASSO problem. Here FISTA algorithm is hence applied to solve both the preliminary LASSO estimation and the adaptive LASSO estimation.

The FISTA algorithm is reviewed as follows. The coefficients are first initialized as $x_i^{(1)} = 0$. Then the projection coefficient vector x is iteratively updated. In the n-th iteration, a temporary update is calculated as

$$x_i'^{(n+1)} = \mathrm{ST}_\lambda \left(x_i'^{(n)} - \mu \partial_i G(x'^{(n)}) \right), \tag{4.32}$$

where ST is the soft thresholding function defined as

$$\mathrm{ST}_\lambda \left(x' \right) = \mathrm{sign}(x') \max \left\{ \left| x' \right| - \lambda, 0 \right\} . \tag{4.33}$$

Note that the soft thresholding is a part of the LASSO algorithm, which selects the modes with amplitude greater than λ, and shrinks the estimated amplitudes of the selected modes by λ in each iteration. Here the coefficient μ is the step size of the gradient descent iteration, and $\partial_i G(x'^{(n)})$ is the i-th element of the gradient vector of G at point $x'^{(n)}$:

$$\partial_i G(x'^{(n)}) = \Sigma_{\alpha\beta}^{-1} \, \mathrm{Re} \left\{ A_{\alpha i}'^{*} (\gamma_\beta - A'_{\beta j} x'_j) \right\}, \tag{4.34}$$

where $\mathrm{Re}\{\bullet\}$ denotes the real part of the input complex vector. Compared to gradient descent algorithm, FISTA algorithm requires an additional update using a weighted average between $x'^{(n+1)}$ and $x'^{(n)}$ to improve the convergence speed:

$$\begin{aligned} t^{(n+1)} &= \frac{1 + \sqrt{1 + 4(t^{(n)})^2}}{2}, \\ x'^{(n+1)} &\leftarrow x'^{(x+1)} + \frac{t^{(n)} - 1}{t^{(n+1)}} (x'^{(n+1)} - x'^{(n)}), \end{aligned} \tag{4.35}$$

where the relative weight is initialized as $t^{(1)} = 1$.

Note that FISTA algorithm converges as long as the gradient descent step size μ satisfies

$$0 < \mu < \frac{1}{\left\| \mathbf{A}^\dagger \cdot \mathbf{\Sigma}^{-1} \cdot \mathbf{A} \right\|}, \tag{4.36}$$

where the operation $\|\bullet\|$ returns the spectrum norm of the input matrix, which is estimated numerically by simulating a large number of random vectors with l^2 norms normalized to one taking different realizations. The matrix operator $\mathbf{A}^\dagger \cdot \mathbf{\Sigma}^{-1} \cdot \mathbf{A}$ is subsequently applied to each random vector to yield a corresponding transformed vector. Finally, the spectral norm of the operation is determined as the maximum l^2

norm of these transformed vectors.

As summarized in the following Algorithm, the projection coefficients are first initialized as zero, and FISTA algorithm is used to find the global minimum of the LASSO loss function. This global minimum is the preliminary LASSO estimation, which is subsequently used to weight the penalty coefficients in the adaptive LASSO loss function. Finally, the preliminary LASSO estimation is set as the "warm" start of the adaptive LASSO estimation, and FISTA algorithm again is used to find the global minimum of the adaptive LASSO loss function. This minimum is the final solution.

Algorithm mass map reconstruction algorithm

Input: γ: Pixelized complex 3D shear field

Output: δ: 3D array of density contrast

Normalize column vectors of $\mathbf{A}$
Estimate step size μ and
Initialization:
$x'^{(1)} = 0$
$\hat{w} = 1$
$t^{(1)} = 1$,$i = 1$, $j = 1$
while $j \leq 2$ **do**
  while $i \leq N_{\text{iter}}$ **do**
    # soft thresholding
    $x_i'^{(n+1)} = \text{ST}_{\hat{w}\lambda}\left(x_i'^{(n)} - \mu\partial_i G(x'^{(n)})\right)$
    # FISTA algorithm
    $t^{(n+1)} = \frac{1+\sqrt{1+4(t^{(n)})^2}}{2}$
    $x'^{(n+1)} \leftarrow x'^{(x+1)} + \frac{t^{(n)}-1}{t^{(n+1)}}(x'^{(n+1)} - x'^{(n)})$
    $i = i + 1$
  end while
  Re-initialization:
  $\hat{w} = \left|\hat{x'}_{\text{LASSO}}\right|^{-2}$, $\lambda \leftarrow \lambda_{\text{ada}}$
  $\hat{x'}^{(1)} = x'^{(N_{\text{iter}})}$
  $t^{(1)} = 1$, $i = 1$
  $j = j + 1$
end while
$\delta = \mathbf{\Phi}\mathcal{N}^{-\frac{1}{2}}x'^{(N_{\text{iter}})}$

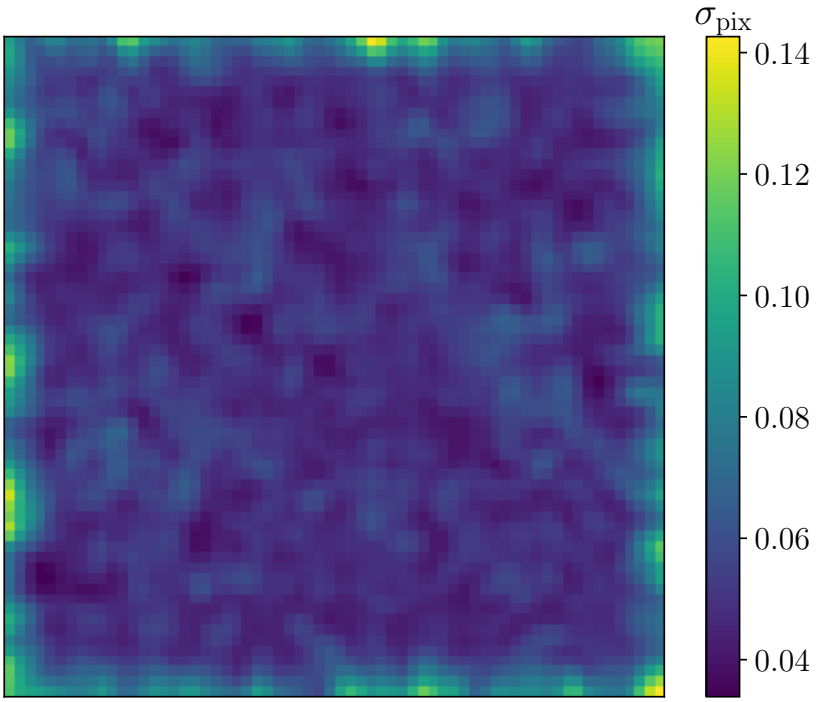

FIGURE 4.8: The standard deviation pixel map of the HSC-like shear measurement error for the fifth source galaxy bin ($0.69 \leq z < 0.80$).

4.3 Halo Simulations

This section presents the halo simulations that are used to test the algorithm, which use halos with a variety of masses in the range $10^{14}h^{-1}M_{\odot} < M < 10^{15}h^{-1}M_{\odot}$, and redshifts in the range $0.05 < z < 0.85$, respectively. The parameter space is divided into eight redshift bins and eight mass bins with equal separation. The input halo redshift and halo mass are randomly shifted from the bin center by a small amount in order to avoid repeatedly sampling at the exact same halo mass and redshift.

The concentration parameter $c_{\rm h}$ of a NFW halo is determined as a function of the halo mass (M_{200}) and redshift ($z_{\rm h}$) according to Ragagnin et al. (2019):

$$c_{\rm h} = 6.02 \times \left(\frac{M_{200}}{10^{13}M_{\odot}}\right)^{-0.12} \left(\frac{1.47}{1. + z_{\rm h}}\right)^{0.16} . \tag{4.37}$$

The weak lensing shear fields of the NFW halos are calculated according to Takada & Jain (2003). The shear distortions are applied to one hundred realizations of galaxy catalogs with the HSC-like shear measurement error and photo-z uncertainty.

The mock galaxy catalogs are generated using the HSC S16A shear catalog (Mandelbaum et al., 2018b). The simulations use the galaxies in a 1 square degree field at

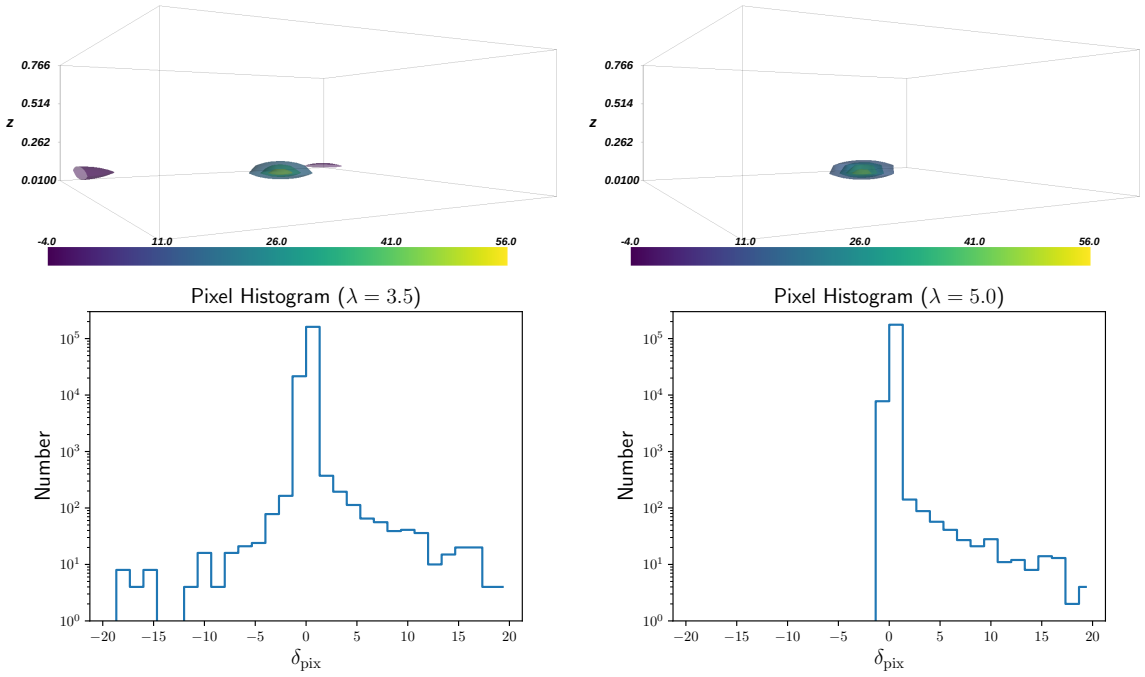

FIGURE 4.9: The upper panels show the density maps reconstructed from a mock galaxy shear catalog, which includes shear measurement and photo-z uncertainties, using the mass map reconstruction algorithm with penalty parameters $\lambda = 3.5$ (left) and $\lambda = 5.0$ (right). The axes and color maps have the same meanings as Figure 4.7. The lower panels show the corresponding number histograms of pixel values. The input halo mass is $M_{200} = 10^{15.02}\ h^{-1}M_{\odot}$, and its redshift is $z = 0.164$.

the center of tract 9347 (Aihara et al., 2018b). The average galaxy number density in this region is 22.94 arcmin^{-2}. The positions of galaxies are randomized to distribute homogeneously in the one-square degree stamp. The redshift for each galaxy is assigned following the `MLZ` photo-z probability distribution function (Tanaka et al., 2018).

I simulate the HSC-like shear measurement error due to shape noise and sky variance with different realizations by randomly rotating the galaxies in the HSC first-year shear catalog. The shear measurement error on individual galaxy level and individual pixel level are demonstrated in Figure 4.4. The standard deviation map of the noise is demonstrated in Figure 4.8.

4.4 Results

This section serves to test the performance of the mass map reconstruction algorithm by adopting models where the matter density field is represented by multi-scale NFW atoms. The dictionary is constructed with three frames of different NFW scale radii

in comoving coordinate: 0.12 h^{-1} Mpc, 0.24 h^{-1} Mpc, and 0.36 h^{-1} Mpc. The truncation radii are set to four times the scale radii for the atoms in the dictionary, i.e., assuming that $c_{\rm h} = 4$. Note that each frame of the NFW dictionary fixes the scale radius in *comoving* coordinates and thus the NFW atoms have different angular sizes when placed at different redshift.

The algorithm is tested by varying the penalty parameter for the LASSO estimation with $\lambda = 3.5$, 4.0, and 5.0. The corresponding penalty parameters for the final adaptive LASSO estimations are set to $\lambda_{\rm ad} = \lambda^{\tau+1}$. Here, both the LASSO estimation and the adaptive LASSO estimation select the modes with SNR greater than λ in each gradient descent iteration, and the local density is estimated for the selected pixels with a shrinkage of the estimation amplitude. The difference is that the LASSO algorithm shrinks the density amplitudes by λ for every selected pixels; in contrast, the adaptive LASSO algorithm suppresses the shrinkage by down-weighting their penalties if the preliminary estimation for this mode is greater than λ, and otherwise the adaptive LASSO algorithm enhances the shrinkage.

The smoothed shear measurements after pixelation have the resolution limit set by the Gaussian smoothing kernel with a standard deviation of $1\farcm5$ and the $1'$ pixel scale as detailed in Sections 4.1.2.2. The reconstructed density fields are smoothed with the same Gaussian kernel in each lens redshift plane and they have the same resolution limit.

Figure 4.9 shows the 3D density maps reconstructed with two different penalty parameters (i.e. $\lambda = 3.5$ and $\lambda = 5.0$) for a halo with $M_{200} = 10^{15.02}\ h^{-1}M_{\odot}$, located at redshift 0.164. The corresponding number histograms for pixelated density contrast field are shown in Figure 4.9. As shown, the adaptive LASSO algorithm assigns zero value to a fraction of the reconstructed modes, while retaining strong signals. In addition, the right panels demonstrate a case where almost all of the modes with pure noise are set to zero with a large penalty parameter. It is important to note that the reconstructed density contrast maps are not compromised by the smearing in the line-of-sight direction. That is, the reconstructed lens is localized in redshift.

Following Leonard et al. (2014), the detected peaks in the l-th ($l = 1...20$) lens redshift plane are normalized as follows to account for the peak amplitude difference arising from the difference in the norm of the lensing kernels in different redshift bins:

$$\delta^{\rm n}_{\rm peak}(\vec{\theta}, z_l) = \delta_{\rm peak}(\vec{\theta}, z_l)/\mathcal{R}_l^{\frac{1}{2}}, \tag{4.38}$$

where the normalization matrix is defined as

$$\mathcal{R}_l = \sum_s K^2(z_l, z_s)\,, \tag{4.39}$$

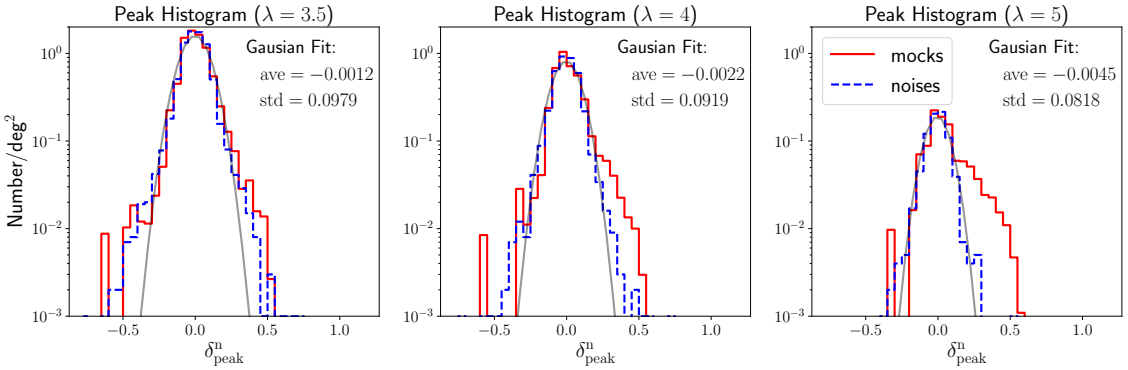

FIGURE 4.10: The peak counts, namely the number density per square-degree, as a function of peak overdensity for maps reconstructed with different setups. The solid red histograms show the results of the reconstructions from the mock shear catalogs with penalty parameters: $\lambda = 3.5, 4.0, 5.0$, from left to right. The dashed blue histograms are the corresponding results of the reconstruction from 1000 realizations of pure noise catalogs. The gray lines are the best-fit Gaussian distributions to the noise peak histograms.

where $K(z_l, z_s)$ is the lensing kernel. Figure 4.10 demonstrates the histograms of the normalized peaks with different penalty parameters . In the figure, the histograms from 100 realizations of all the halos sampled in the redshift-mass plane are stacked together. Additionally, 1000 realizations of pure noise catalogs are generated and the reconstruction are performed using the noise catalogs with the intent to examine the noise properties. The histograms of the normalized peaks detected from the pure noise catalogs are shown in Figure 4.10 along with the best-fit Gaussian functions of the noise peak histograms.

It is found that the number counts including both true and false peaks decrease as the penalty parameter λ increases. In addition, the standard deviation of noise peaks decreases as λ increases. As a result, with $\lambda = 5.0$, a clearer excess is found in the positive peak counts compared with the noise peak histograms, especially at the high density contrast. This is expected because a higher penalty parameter prefers a sparser solution; more peaks originating from the noise are removed than those from real clusters at the high density contrast.

The position offsets of the detected halos compared to the input positions are demonstrated in Figure 4.11. The left panel shows the 2D number histograms stacked over all the simulations as a function of the angular distance and the redshift offsets. A clear clustering of the peaks close to the position of the input halo is found on the stacked number histogram. For each simulation, the positive peaks closest to the input position (in the pixel unit) is identified. If a closest peak is located inside the region denoted with the dashed box in the left panel of Figure 4.11, it is regarded as a "true" peak detection. Other identified peaks, which include both positive and

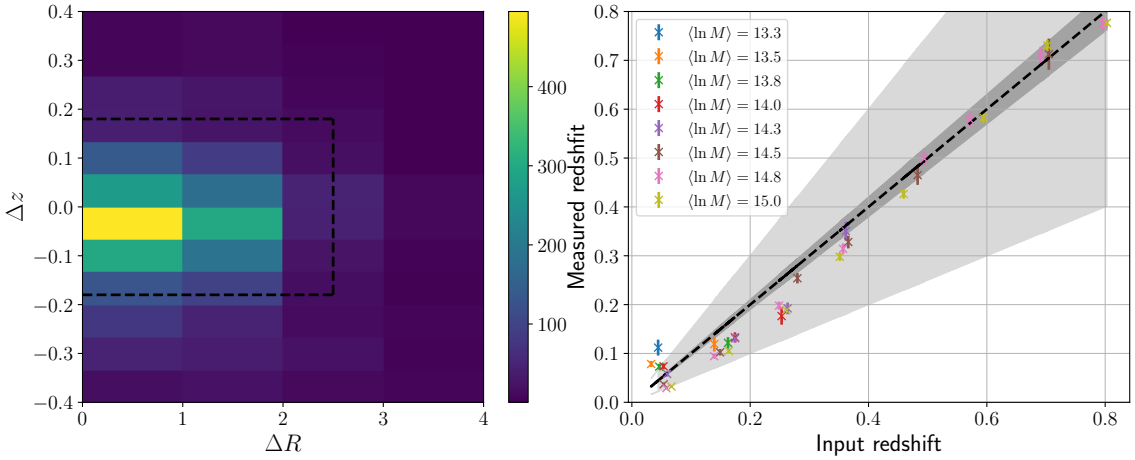

FIGURE 4.11: The left panel shows the stacked 2D distribution of the deviations of detected peak positions from the centers of the corresponding input halos. The x-axis is for the deviated distance in the transverse plane, and the y-axis is for the deviation in redshift. In each simulation, the positive peak inside the dashed black box with the minimal offset (in the pixel unit) from the position of the input halo is taken as "true" detection. The right panel shows the redshift deviation of detected peaks. The x-axis is the input halo redshifts, and the y-axis is the redshift of the detected peak. The cross-points denote the average of the detected peaks for each halo over different noise realizations, and the error-bars indicate the uncertainties of the averages. The deep gray area indicates relative redshift bias less than 0.05, and the light gray area for relative redshift bias less than 0.5. These results are based on the reconstruction with the NFW dictionary with $\lambda = 3.5$.

negative peaks, are judged to be false detection.

The right panel of Figure 4.11 shows the estimated redshift of the "true" detections averaged over the simulations (with different noise realizations) for each halo as a function of the input redshift. As shown, the estimated redshifts are slightly lower than the ground truth by $\Delta z \sim 0.03$ for halos in the low-redshift range ($z \leq 0.4$). For halos at $0.4 < z \leq 0.85$, the relative redshift bias is below 0.5%. The standard deviation of the redshift estimation is 0.092.

In order to reduce the number of false detections, peaks are selected as galaxy clusters if the peak values are greater than an empirically determined threshold. The threshold is set in units of the standard deviation of the noise peaks. Different detection thresholds (1.5σ and 3.0σ) are used to detect galaxy clusters from the mass maps reconstructed with different penalty parameters. Figures 4.12 and 4.13 show the detection rates for halos in the redshift-mass plane for different penalty parameters ($\lambda = 3.5$ and $\lambda = 5.0$). The corresponding number of false detections per square degree as a function of detection threshold are also demonstrated in the figures.

As shown, the false peak density is successfully reduced for relatively large detection threshold, but the detection rate of halo also decreases. After a few experiments,

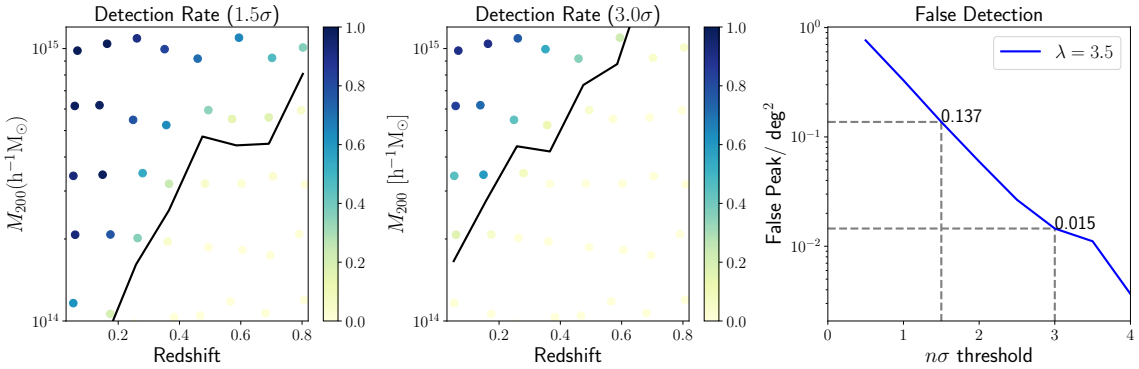

FIGURE 4.12: The detection rates and false peak densities for different detection thresholds. The left (middle) panel shows the halo detection rates for detection threshold that equals 1.5σ (3.0σ). The black lines refer to the contours for detection rates that equal 0.1 . The right panel shows the density of false peaks as a function of detection threshold. The penalty parameter is set to $\lambda = 3.5$.

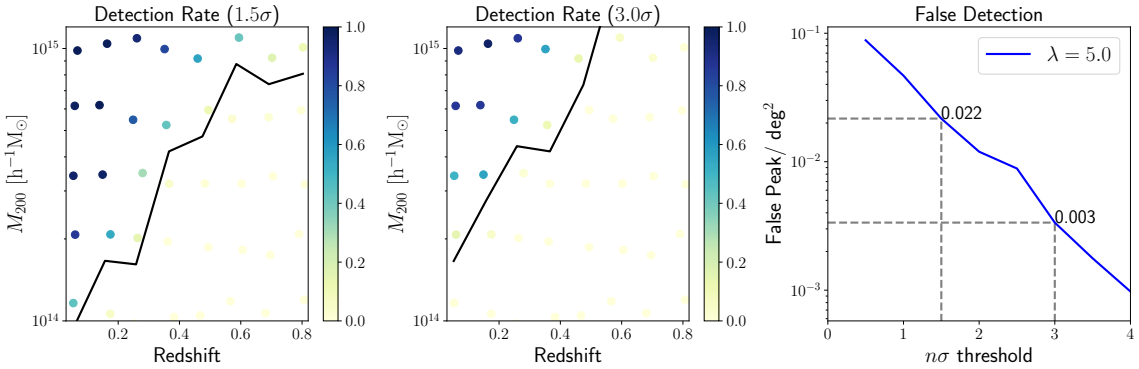

FIGURE 4.13: The same as Figure 4.12, but for the penalty parameter $\lambda = 5.0$.

the detection threshold is fixed to 1.5σ and set the penalty parameter λ to 5.0 since the combination suppresses the false detection to 0.022 while keeping a high halo detection rate. In summary, the mass map reconstruction method is able to detect halos with minimal mass of $10^{14.0}h^{-1}M_\odot$, $10^{14.7}h^{-1}M_\odot$, $10^{15.0}h^{-1}M_\odot$ for the low ($z < 0.3$), median ($0.3 \leq z < 0.6$) and high ($0.6 \leq z < 0.85$) redshift ranges, respectively.

Using the detection rate measured from the simulations, it is possible to predict the number density of clusters that can be detected with the assumption on the halo mass function of Tinker et al. (2008). Here, HMF (Murray et al., 2013), which is an open-source package[3], is used to calculate the halo mass function. The predicted halo detection number density for the setup $\lambda = 5$ and 1.5σ detection threshold is shown in Figure 4.14. The resulting cluster number density is 0.49 deg^{-2}, which

[3] https://github.com/halomod/hmf

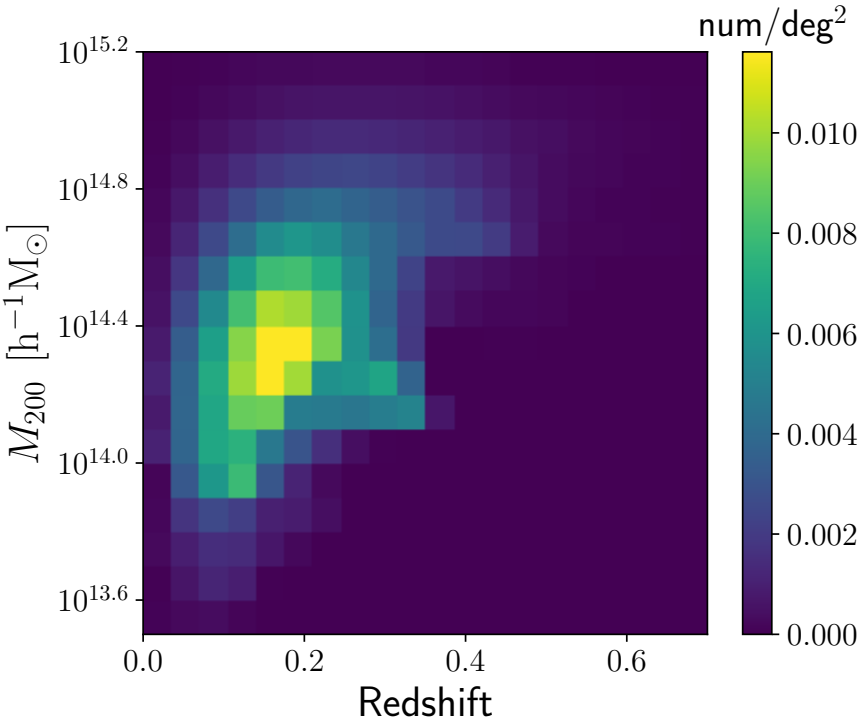

FIGURE 4.14: The expected number density of detected clusters per square degree as a function of halo redshift (x-axis) and halo mass (y-axis). The number density in total is 0.49 deg^{-2}.

is much higher than the estimated false detection rate: 0.022 deg^{-2}. This cluster number density corresponds to 78.4 clusters for the first-year HSC shear catalog (Mandelbaum et al., 2018b), which has a survey area of $\sim 160\,\mathrm{deg}^2$. In summary, the expected number of detection is slightly higher than that of 2D cluster detections (63 detected clusters) for the first year HSC shear catalog (Miyazaki et al., 2018a). Furthermore, the 3D detection method provides an accurate redshift estimation for individual clusters; whereas, the redshift information is not provided from the 2D mass map reconstruction.

4.5 Summary

This section develops a novel method to generate high-resolution 3D density maps from weak-lensing shear measurement with photometric redshift information. The 3D density field is modelled by a collection of NFW atoms with different physical sizes. With a prior assumption that the clumpy mass distribution is sparse in 3D, we reconstruct the density map using the adaptive LASSO algorithm (Zou, 2006). It has been found that the standard LASSO algorithm results in significant smearing

of structure in the line of sight direction even in the absence of galaxy shape noise and photometric redshift uncertainties. Our adaptive LASSO algorithm efficiently reduces the smearing of structure. The performance of cluster detection with the reconstructed 3D mass maps has been examined using mock catalogs that apply shear distortions from isolated halos to galaxies with HSC-like shapes and photo-z uncertainties. Under the realistic conditions, our method is able to detect halo with minimal mass limits of $10^{14.0}\mathrm{h}^{-1}M_{\odot}$, $10^{14.7}\mathrm{h}^{-1}M_{\odot}$, $10^{15.0}\mathrm{h}^{-1}M_{\odot}$ at low ($z < 0.3$), median ($0.3 \leq z < 0.6$) and high ($0.6 \leq z < 0.85$) redshifts, respectively, with an average false detection of 0.022 deg^{-2}. The estimated redshifts of the clusters detected in the reconstructed mass maps are slightly lower than the true redshift by $\Delta z \sim 0.03$ for halos at low redshifts ($z \leq 0.4$). The relative redshift bias is below 0.5% for halos at $0.4 < z \leq 0.85$, and the standard deviation of the redshift estimation is 0.092.

There are two other 3D mass map inversion methods adopting different dictionaries and regularizations:

- Simon et al. (2009) proposed to perform a reconstruction in Fourier space, which is equivalent to representing the density contrast field with sinusoidal functions. However, sinusoidal functions are not localized in configuration space, and the density contrast field is not sparse in Fourier space; therefore, sparsity priors can not be directly applied to this model dictionary for high-resolution mass map reconstructions. This method used the Wiener filter, which is also known as l^2 ridge penalty, to find a penalized solution in Fourier space. Oguri et al. (2018) applied this method to the first-year shear catalog of the Hyper Suprime-Cam Survey (Aihara et al., 2018b), and found that the density maps reconstructed by the method suffer from significant line-of-sight smearing with standard deviation of $\sigma_z = 0.2 - 0.3$.

- Leonard et al. (2014) proposed to model the density contrast field with starlets (Starck et al., 2015). This method is known as GLIMPSE algorithm. However, the Starlet dictionary does not account for the angular scale difference at different lens redshifts, and it is not specifically designed to model the clumpy mass distribution in the Universe. This method adopted a derivative version of the l^1 LASSO penalty to find a sparse solution in the Starlet dictionary (Starck et al., 2015). It reduced the smearing by adopting a "greedy" coordinate descent algorithm on a non-convex penalized loss function. Even though the non-convex loss function does not have global minimum, the "greedy" coordinate descent algorithm forced the structure to grow only on the most related lens redshift plane. However, this method cannot be directly applied to large dataset.

Compared to those methods, our method uses a more model dictionary that is

more representative to the mass distribution of clumpy dark matter in the universe. Moreover, our loss function is strictly convex; therefore, it can be directly applied to large data set in real observation. The performance of our algorithm will be demonstrated in Chapter 5.

5

3D mass map from HSC three-year data

Contents

This chapter serves to apply the 3D mass map reconstruction algorithm introduced in Chapter 4 to the weak lensing shear catalog introduced in Chapter 2, and reconstruct a 3D weak lensing mass map using a $4^\circ \times 4^\circ$ region of the HSC three-year data.

5.1 Algorithm and setup

The updates and setups of the algorithm are first introduced in this section.

5.1.1 non-negative Elastic net

The algorithm is updated to the adaptive elastic net version according to Zou & Zhang (2009). The elastic net (Zou & Hastie, 2005) estimation is defined as

$$\hat{x'}_{(0)} = (1+\eta)\arg\min_{x}\left\{\left\|\Sigma^{-\frac{1}{2}}(\gamma - \mathbf{A}'x')\right\|_2^2 + C_{(0)}(x')\right\}, \tag{5.1}$$

where $C_{(0)}$ is the regularization term given by

$$C_{(0)}(x') = 2\left\|\lambda_{(0)} \circ x'\right\|_1^1 + \left\|\eta_{(0)} \circ x'\right\|_2^2, \tag{5.2}$$

where "$\circ$" refers to the element-wise product and the index (0) refer to the preliminary estimation. As shown, the elastic net algorithm is a hybrid of l^1 and l^2 regularizations, where λ is the LASSO (l^1) regularization parameter and η is the Ridge (l^2) regularization parameter. The l^1 term is in charge of selecting modes that are related to data while setting the others to zeros; the l^2 term stabilizes the selection process and avoid mistakenly setting modes related to data to zero. Note that the $(1+\eta)$ term is multiplied to the estimation is to avoid the double shrinkage from LASSO and Ridge regularization (Zou & Hastie, 2005).

In addition to the elastic net regularization, a non-negative penalty requiring $x' \geq 0$ (see e.g., Wu et al., 2014) is used to regularize the loss functions, and thus the estimations focus on reconstructing mass distribution within massive halo and the negative density contrast field in voids are not take into account here.

Adaptive weights derived from the former estimation are used to to penalize different projection coefficients in the l^1 penalty following Zou (2006). The weighting vector for the '(t)'-th estimation is given by

$$\hat{w}_{(t)} = \frac{1}{\left|\hat{x'}_{(t-1)}\right|^{\tau}}, \tag{5.3}$$

where $\hat{x'}_{(t-1)}$ is the '$(t-1)$'-th estimation. The adaptive elastic net (Zou & Zhang, 2009) is a generalization of adaptive LASSO, the estimator of which is given by

$$\hat{x'}_{(t)} = \arg\min_{x'}\left\{\frac{1}{2}\left\|\Sigma^{-\frac{1}{2}}(\gamma - \mathbf{A}'x')\right\|_2^2 + C_{(t)}\right\} \tag{5.4}$$

The regularization of the '(t)'-th estimation is

$$C_{(t)}(x') = 2\left\|\lambda_{(t)} \circ x'\right\|_1^1 + \left\|\lambda_{(t)} \circ \hat{w}_{(t)} \circ x'\right\|_1^1. \tag{5.5}$$

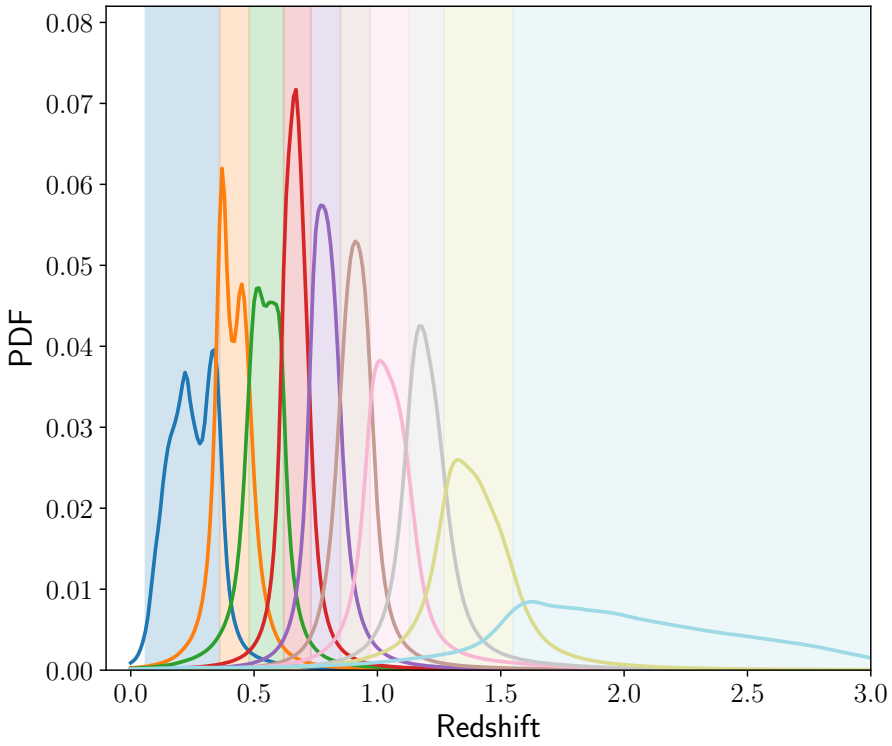

FIGURE 5.1: The stacked photo-z posteriors in each source redshift bin. The colored regions denote the source redshift bins.

5.1.2 Setup

The source galaxies are separated into 10 redshift bins, which is shown in Figure 5.1. The pixel size in the transverse plane for both shear field and reconstructed kappa map are set to $2'$. Gaussian smoothing is not applied on the transverse plane. The pixel scale in the line-of-sight direction is set to 0.06, and the redshift range is from 0.06 to 0.78. That is, the lens redshift is divided into 12 bins.

The elastic net estimator is used for the preliminary estimation since it is reasonable to start from a stable estimation. For the adaptive estimation after the preliminary estimation, η is set to zero, and it reduces to LASSO estimator, which focus on selecting related modes. The setup for the preliminary estimation $t = 0$ is $\lambda_{(0)} = 0$, $\eta_{(0)} = 1$, which is a Ridge estimation rescaled by $(1 + \eta_{(0)})$. The setup for the subsequent estimation is $\lambda_{(t)} = 5\,(\sigma_{\rm noi})^{\tau}$, $\eta_{(t)} = 1$. The hyper-parameter τ is set to 2. The parameter $\sigma_{\rm noi}$ is the STD of pure noise which is obtained by applying the Ridge estimator to 200 realizations of a pure noise field.

5.2 3D mass map

The algorithm is run on a 16 deg^2 ($4^\circ \times 4^\circ$) region in the XMM filed of the three-year HSC shear catalog. The stacked posteriors for 10 source galaxy redshift bins are demonstrated in Figure 5.1.

Figure 5.2 demonstrates a number of lensing kernels with (dashed lines) and without (solid lines) the influence of photo-z uncertainties. As shown, the photo-z uncertainties do not change the shape of lensing kernel significantly, hence no further calibration is conducted on the photo-z posteriors in the 3D mass map reconstruction.

Figure 5.3 shows the normalized number histograms of the first shear component g_1 on individual galaxy level (blue lines) and on individual pixel level (orange lines) after pixelation As shown, the noise on shear estimation is reduced after pixelation Furthermore, the number histogram on individual pixel level is not significantly different from a Gaussian distribution, which indicates that the noise on the shear measurements can be approximate by a Gaussian random variable.

The reconstructed 3D mass map in the 16deg^2 region from field XMM is demonstrated in Figure 5.4. After reconstruction, local peaks are detected from the mass map. As demonstrated by Figure 5.4, the sparse penalty sets most of the pixels to zero; therefore, the peak identification from the mass map is straightforward. Peaks are merged if the distance between two peaks are less than two pixels, namely $4'$, and the redshift difference is less than 0.12 . The center of the detection is set to the highest peak among the merged detection.

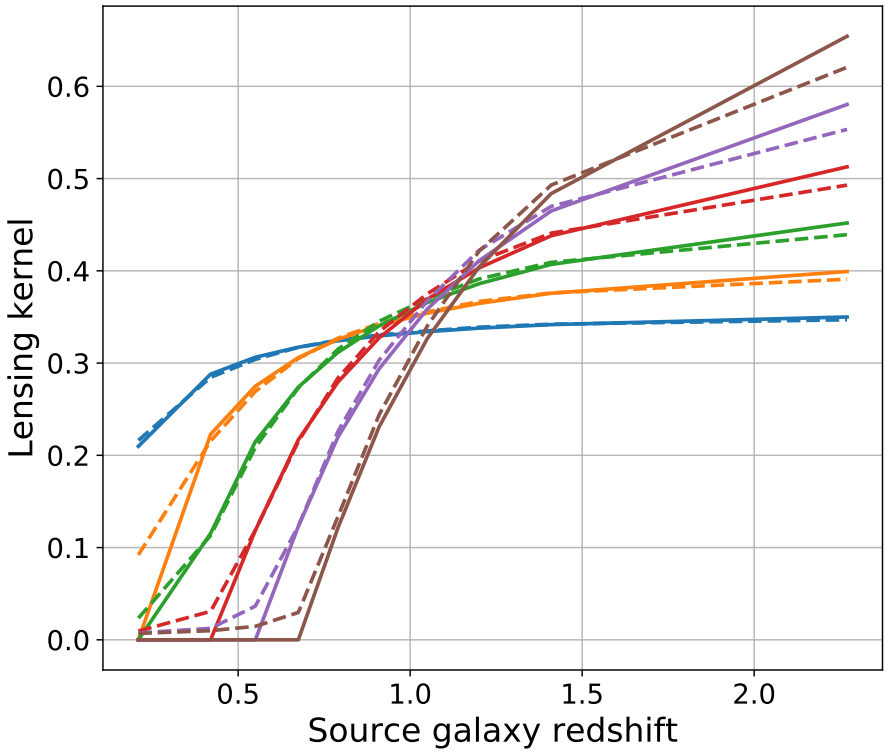

FIGURE 5.2: The normalized lensing kernels of the lens system as functions of source galaxy redshift. The solid (dashed) lines are for the results without (with) photo-z uncertainties. The colors from left to right correspond to lens systems at redshift 0.06, 0.18, 0.30, 0.42, 0.54, 0.66 .

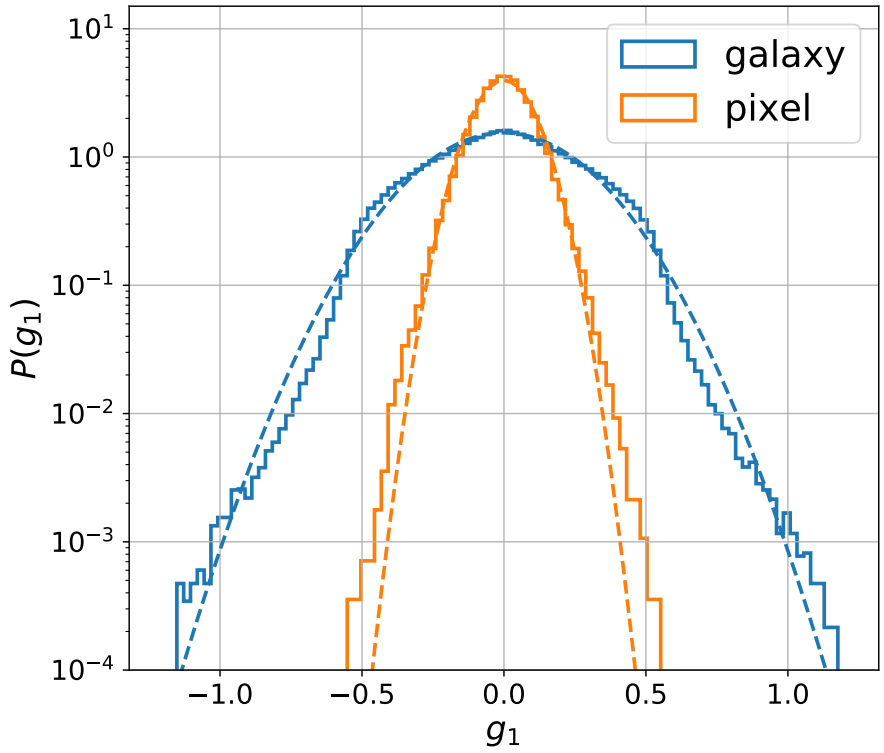

FIGURE 5.3: The histograms of the first component of shear g_1 on individual galaxy level (blue) and on individual pixel level (orange). The solid (dashed) lines are the histograms for g_1 (the best-fit Gaussian distributions).

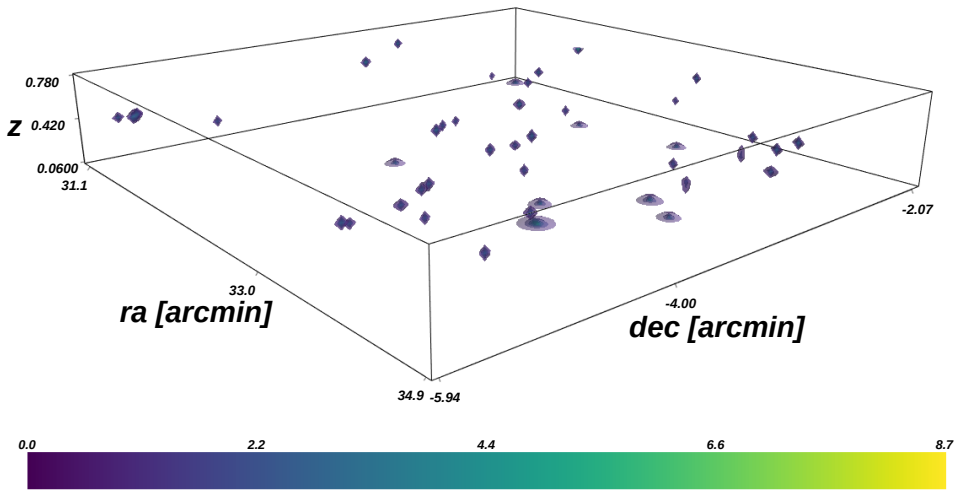

FIGURE 5.4: The reconstructed 3D weak lensing mass map using shear measurements from a $4^\circ \times 4^\circ$ region in the XMM field. The color bar indicate the value of the reconstructed density contrast field.

Moreover, it is possible to estimate halo masses of galaxy clusters from the 3D mass map by summing up the M_{200} for all the NFW basis atoms that are identified as part of the galaxy cluster. To be more specific, the M_{200} value of each basis atom can be calculated from the projection coefficient on this basis atom.

5.3 Matching to Optical clusters

Clusters can also be identified using the galaxy clustering information observed from SDSS (Section 5.3.2) and HSC (Section 5.3.1).

5.3.1 CAMIRA Clusters

The "Cluster finding algorithm based on Multiband Identification of Red-sequence gAlaxies"(CAMIRA) clusters (Oguri et al., 2018) are detected by the CAMIRA algorithm (Oguri, 2014) from the multi-bands images of the HSC Wide layer (Aihara et al., 2018b). The CAMIRA algorithm is based on the Stellar Population Synthesis (SPS) model of Bruzual & Charlot (2003) to predict colors of red-sequence galaxies at a given redshift for an arbitrary set of bandpass filters. This SPS prediction is then calibrated with spectroscopic galaxies to improve the accuracy of the model prediction. Using the calibrated SPS model, CAMIRA algorithm computes the likelihood of each galaxy being in the red sequence as a function of redshift and create a 3D

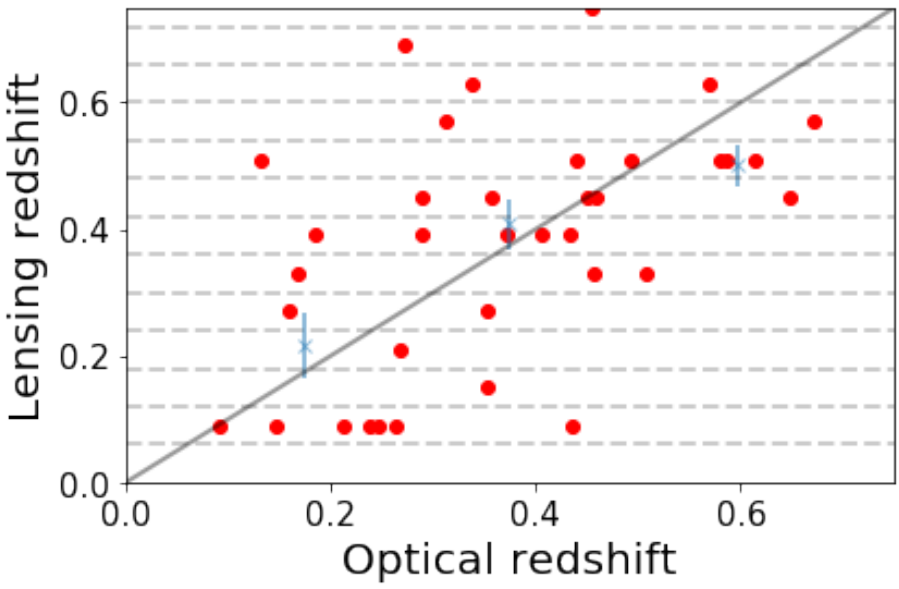

FIGURE 5.5: The scatter points show the relation between the redshifts of galaxy clusters estimated from the weak lensing mass map and the redshifts of their best-match optical clusters from CAMIRA and WHL15 catalogs. The blue "×" show the average of weak-lensing redshift versus the average of optical redshift in the optical redshift range $z < 0.25$, $0.25 < z < 0.50$, and $0.50 < z < 0.75$, respectively. The error bars are the error of the average.

richness map based on the likelihood. The CAMIRA clusters are detected as the peaks of the richness map with a richness threshold $N_{\rm mem} = 15$. The center of the cluster is defined as the center of the Brightest Cluster Galaxy (BCG).

5.3.2 WHL15 Clusters

Wen & Han (2015, WHL15) identify a cluster if more than eight member galaxies with r-band magnitude brighter than 21 are found within a radius of 0.5 Mpc and a photo-z gap of $z \pm 0.04(1 + z)$ in the in photometric images of SDSS DR12 (Alam et al., 2015). The richness of the identified cluster are subsequently calibrated using cluster masses estimated by X-ray or Sunyaev–Zeldovich measurements.

5.3.3 Results

The detected clusters from the weak lensing mass map are matched to the aforementioned optical galaxy clusters. The match distance is set to 2.5 pixels, namely $5'$. If one weak lensing cluster candidate has more than one matches in the optical cluster catalogs (i.e., CAMIRA and WHL15), the optical cluster with the minimum redshift difference is selected as the best-match to the weak lensing detection. On the other

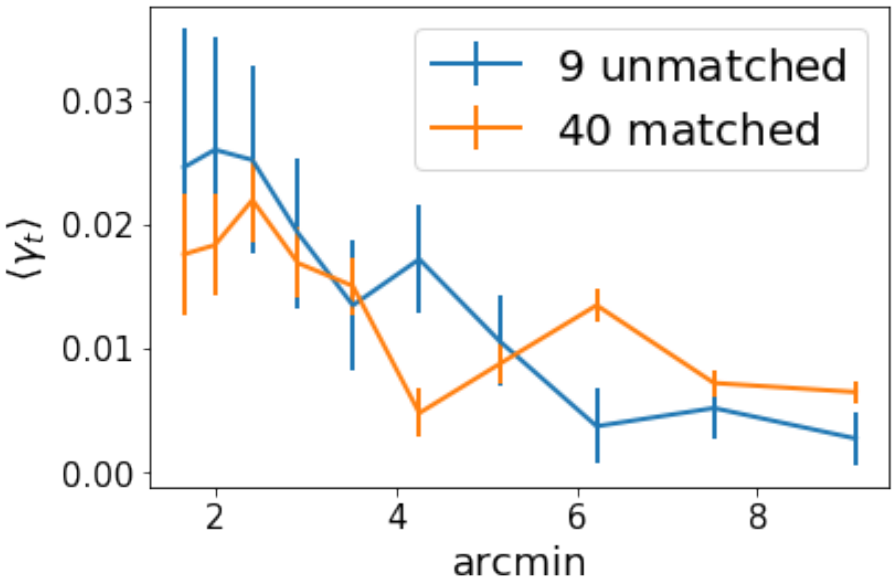

FIGURE 5.6: The stacked tangential shear as a function of angular distance to the detected peak for weak lensing detected clusters have matches and do not matched to the optical clusters.

hand, if one weak lensing cluster candidate has only one match, the match is regarded as the best-match. The weak lensing redshift versus the redshift of the best-match optical cluster is shown in Figure 5.5. The color indicates the M_{200} estimated from the weak lensing mass map. I bin the matched cluster into three redshift bins–$z < 0.25$, $0.25 < z < 0.50$, and $0.50 < z < 0.75$—and compare the average weak lensing redshift versus optical cluster redshift. A good correlation between the optical redshift and weak lensing redshift is detected even though the weak lensing redshift is relatively low compared to the optical redshift at the high redshift end.

In summary, 49 cluster candidates are detected from the 3D weak lensing mass map and 40 of them have matches to optical clusters. The stacked tangential shear signal of background galaxies with redshifts $z > z_{\rm wl} + 0.1$ is shown in Figure 5.6, where $z_{\rm wl}$ refers to the redshift estimated from the 3D mass map. Both the results for matched detections and unmatched detections are plotted. The results show that even the matched and unmatched detections causes comparable weak lensing shear distortion on the corresponding background galaxies. Those unmatched detection can be non-viralized dark matter projections, systematics or dark clusters with very high mass-to-light ratio. It is necessary to study the contamination from projected large scale structure in the detected peaks using weak lensing mock catalogs (Shirasaki et al., 2019).

6

Summary and Outlook

Contents

6.1 Weak lensing shear catalog

This thesis presented the HSC three-year galaxy shear catalog covering an area of 433.48 $\deg^2$ of the northern sky, with a mean i-band seeing of 0.59 arcsec. With conservative galaxy selection criteria, the raw galaxy number density is 22.9 arcmin^{-2} and the effective galaxy number density is 19.9 arcmin^{-2}. The galaxy catalog has a depth of 24.5th magnitude.

The current three-year galaxy shear catalog were calibrated with HSC-like image simulations that transfer the galaxy images from COSMOS HST to the HSC observing conditions. The simulated galaxy sample has the same distributions of galaxy properties as the real HSC data. The following subsections outlook the future developments on realistic galaxy image simulations.

6.1.1 Redshift-dependent shear in simulations

MacCrann et al. (2020) used parametric galaxy models that are fitted to the COSMOS HST galaxies as their input training sample, and they randomly populated these parametric galaxies in a homogeneous manner with a density matched to the DESY3 observation to simulate multi-band DES images that were used to test and calibrate Metacalibration (Sheldon & Huff, 2017).

They tested the performance of their pipeline with redshift-dependent-shear simulations, in which galaxies at different redshifts were distorted by different lensing shears, and compared the results with those from the conventional constant-shear simulations. According to Fig. 8 of MacCrann et al. (2020), the amplitude of the additional multiplicative bias due to the redshift-dependent shear is below 1% for redshift $z < 1$, whereas the multiplicative bias reaches $\sim 3\%$ for redshifts $1 < z < 3$.

However, the discrepancies of the 1D and 2D histograms (see Fig. 3 of MacCrann et al., 2020) of galaxy properties between the simulations and the corresponding data are visually larger when compared to the results in Figs. 2.12 and 2.13 for the DES three-year galaxy image simulations. This difference may be explained by using the postage stamps from the COSMOS HST images where the galaxy morphologies and the clustering (distance) between neighboring galaxies are fully realistic.

It is impossible to directly apply redshift-dependent shear distortions to blended galaxies in the current stamp-based image simulations since the current image simulations are constructed in units of postage stamps from the COSMOS HST images, and all the galaxies in one postage stamp can only be distorted in one piece by a constant shear. In contrast, MacCrann et al. (2020) are constructed in with parametric galaxy models. For that model-based simulations, redshift-dependent shears can be applied on blended galaxies on individual galaxy level.

The influence of redshift-dependent shear distortions in detail in the future image simulations.

6.1.2 Multi-band image simulations

Utilizing the galaxy shapes measured from filter bands other than i-bands in the HSC Wide layer can help reducing the shape estimation uncertainties in weak lensing analyses. However, shapes that are measured from other bands cannot be applied to weak lensing science since only i-band image simulations are produced to validate and calibrate shear estimations. This is because the input galaxy training images are from the COSMOS HST F814W filter band, the transmission curve of which has a much larger overlap with that of the HSC i-band filter than other bands. Therefore,

it would be necessary to carefully check whether the input training samples are still representative of the galaxy images in other filter bands in the future works.

6.1.3 unrecognized blendings

Unrecognized blending refers to the situation where multiple blended sources are identified as one single source by the pipeline. It has been shown by many existing works that unrecognized blends have two impacts on the accuracy of shear measurements:

(i) Sheldon et al. (2020) found that the possibility of unrecognized blends depends on the underlying shear distortion. Such a shear-dependent blending identification leads to an anisotropic selection in the galaxy sample; therefore, it can result in a few percent multiplicative bias.

(ii) MacCrann et al. (2020) found that shear estimated from a detected source with unrecognized blends is a weighted average of the true shears at different redshifts of each of the blends. Simulations that fail to reproduce the redshift dependent shear leads to a bias in the effective galaxy number density on redshift: $n(z)$.

Since the current image simulations directly used real images from the HST survey in our simulations, both recognized and unrecognized blended galaxies that can be resolved by the HST survey were fully included in the current simulations. Based on the fact that the matches in the histograms of different galaxy properties to the HSC data are reasonably good after applying a conservative galaxy selection, the incompleteness of the input HST sample (limited at F814W= 25.2) is not likely to cause significant biases that are not accounted for in the current simulations.

However, the current image simulations are in the regime that blended galaxies are distorted by the same shear. More efforts will be taken to understand and control the systematic biases related to unrecognized blending, especially under the circumstance of redshift-dependent shear distortion.

6.2 FPFS shear estimator

Fourier Power Function Shapelets (FPFS, Li et al., 2018) shear estimator is one of the shear estimators that can reach sub-percent ($\sim 0.6\%$) accuracy on isolated galaxies, but it relies on a calibration of a few percent ($\sim -5.7\%$) multiplicative shear bias in the presence of blending. I will improve the FPFS shear estimator, especially for the cases with blending. Here I summarize the difficulties need to be overcome to improve the FPFS shear estimator and reduce the shear estimation bias to subpercent level for blended galaxies.

6.2.1 Blending identification

Sheldon et al. (2020) found that the blending identification—the possibility that a blending is identified by the source detector—is dependent on the lensing-shear signal. The shear dependent blending identification induces an shear dependent anisotropy in the galaxy sample and thus leads to multiplicative bias in the shear estimation up to 4% under the situation of LSST-like galaxy number density. It is necessary to study the process of blending identification and correct for the bias from the shear dependent blending identification in the `FPFS` shear estimation.

6.2.2 Deblending

According to the results from recent researches (e.g., Li et al., 2018; MacCrann et al., 2020), it is necessary to improve the algorithm for deblending to control the shear estimation bias at subpercent level in the situation with blending. Recent researches explore the probability of using multi-bands information to isolate blended galaxies (Melchior et al., 2018). I will work on new algorithms to improve the performance of deblending on recovering the true shape of blended galaxies.

6.3 Cosmology analysis with 3D mass map

The analysis on the abundance of galaxy clusters is playing a crucial role in constraining cosmology. Since the number density of galaxy clusters as a function of mass and redshift, which is known as the halo mass function, is sensitive to, e.g., the density parameter of matter in the Universe Ω_M, and the dispersion of linear density fluctuations on a comoving scale of $8\,h^{-1}$Mpc, namely σ_8 .

As shown in Chapter 5, galaxy clusters can be identified from the 3D weak lensing mass maps. Both the redshift and the mass can be derived from 3D mass maps without any assumption on the relation between baryonic matter and dark matter. However, the bias and the covariance of the cluster abundance measurement need to be carefully studied using cosmological simulations. The mass estimation suffers from Eddington bias (Chen et al., 2020) originating from low-mass halos that scattered beyond the lower mass limit due to the influence of noise. In addition, the bias of the cluster redshift estimation need to be carefully quantified. I am going to run the weak lensing 3D cluster detector on HSC-like mock galaxy catalogs with different realizations (Shirasaki et al., 2019).

Acknowledgements

First of all, I would like to express my deepest gratitude to my supervisor Professor Naoki Yoshida, Professor Nobuhiko Katayama for introducing me to the research of observational cosmology for his continuous encouragement and advice; Professor Masamune Oguri, Professor Surhud More, Professor Shiro Ikeda for giving me many detailed helps and advices in my research; Professor Masahiro Takada, Professor Hironao Miyatake for introducing me to the Hyper Suprime-Cam Survey.

I would like to also thank Professor Jun Zhang, Ryoma Murata for fruitful discussions about our studies and gave me precious insights into cosmology and astrophysics. I am also thankful to the current and former members of the Kavli IPMU. Especially, Hiroko Niikura, Minxi He, Mingje Jian, Benjamin Throne, Robin Schneider, Tommaso Ghigna, Dominik Zürcher, Chenghan Zha, Tian Qiu, Shenli Tang, Yuxin Huang, Christopher Becker, Carolina Cuesta-lazaro, Natasha Abrams, Timothe Denys, Jiaxin Han, Wenting Wang, Wentao Luo who shared a lot of time with chatting over various things.

Bibliography

Abazajian, K. N., Adelman-McCarthy, J. K., Agüeros, M. A., et al. 2009, ApJS, 182, 543, doi: 10.1088/0067-0049/182/2/543

Aihara, H., Arimoto, N., Armstrong, R., et al. 2018a, PASJ, 70, S4, doi: 10.1093/pasj/psx066

Aihara, H., Armstrong, R., Bickerton, S., et al. 2018b, PASJ, 70, S8, doi: 10.1093/pasj/psx081

Aihara, H., AlSayyad, Y., Ando, M., et al. 2019, PASJ, 71, 114, doi: 10.1093/pasj/psz103

Alam, S., Albareti, F. D., Allende Prieto, C., et al. 2015, ApJS, 219, 12, doi: 10.1088/0067-0049/219/1/12

Baldry, I. K., Liske, J., Brown, M. J. I., et al. 2018, MNRAS, 474, 3875, doi: 10.1093/mnras/stx3042

Bardeen, J. M., Bond, J. R., Kaiser, N., & Szalay, A. S. 1986, ApJ, 304, 15, doi: 10.1086/164143

Bartelmann, M., & Schneider, P. 2001, Physics Reports, 340, 291 , doi: https://doi.org/10.1016/S0370-1573(00)00082-X

Beck, A., & Teboulle, M. 2009, SIAM Journal on Imaging Sciences, 2, 183

Bernstein, G. M., & Armstrong, R. 2014, MNRAS, 438, 1880, doi: 10.1093/mnras/stt2326

Bernstein, G. M., Armstrong, R., Krawiec, C., & March, M. C. 2016, MNRAS, 459, 4467, doi: 10.1093/mnras/stw879

Bernstein, G. M., & Jarvis, M. 2002, AJ, 123, 583, doi: 10.1086/338085

Bickerton, S. J., & Lupton, R. H. 2013, MNRAS, 431, 1275, doi: 10.1093/mnras/stt244

Blanton, M. R., Schlegel, D. J., Strauss, M. A., et al. 2005, AJ, 129, 2562, doi: 10.1086/429803

Bosch, J., Armstrong, R., Bickerton, S., et al. 2018, PASJ, 70, S5, doi: 10.1093/pasj/psx080

Bosch, J., AlSayyad, Y., Armstrong, R., et al. 2019, in Astronomical Society of the Pacific Conference Series, Vol. 523, Astronomical Data Analysis Software and Systems XXVII, ed. P. J. Teuben, M. W. Pound, B. A. Thomas, & E. M. Warner, 521

Bruzual, G., & Charlot, S. 2003, MNRAS, 344, 1000, doi: 10.1046/j.1365-8711.2003.06897.x

Carrasco Kind, M., & Brunner, R. J. 2013, MNRAS, 432, 1483, doi: 10.1093/mnras/stt574

Chen, K.-F., Oguri, M., Lin, Y.-T., & Miyazaki, S. 2020, ApJ, 891, 139, doi: 10.3847/1538-4357/ab74d3

Crittenden, R. G., Natarajan, P., Pen, U.-L., & Theuns, T. 2002, ApJ, 568, 20, doi: 10.1086/338838

Cunha, C. E., Lima, M., Oyaizu, H., Frieman, J., & Lin, H. 2009, MNRAS, 396, 2379, doi: 10.1111/j.1365-2966.2009.14908.x

Dark Energy Survey Collaboration, Abbott, T., Abdalla, F. B., et al. 2016, MNRAS, 460, 1270, doi: 10.1093/mnras/stw641

Davis, M., Efstathiou, G., Frenk, C. S., & White, S. D. M. 1985, ApJ, 292, 371, doi: 10.1086/163168

de Jong, J. T. A., Verdoes Kleijn, G. A., Kuijken, K. H., & Valentijn, E. A. 2013, Experimental Astronomy, 35, 25, doi: 10.1007/s10686-012-9306-1

Driver, S. P., Hill, D. T., Kelvin, L. S., et al. 2011, MNRAS, 413, 971, doi: 10.1111/j.1365-2966.2010.18188.x

Fan, Z., Shan, H., & Liu, J. 2010, ApJ, 719, 1408, doi: 10.1088/0004-637X/719/2/1408

Gaia Collaboration, Brown, A. G. A., Vallenari, A., et al. 2018, A&A, 616, A1, doi: 10.1051/0004-6361/201833051

Hamana, T., Shirasaki, M., Miyazaki, S., et al. 2020, PASJ, 72, 16, doi: 10.1093/pasj/psz138

Hartlap, J., Simon, P., & Schneider, P. 2007, A&A, 464, 399, doi: 10.1051/0004-6361:20066170

Hikage, C., Oguri, M., Hamana, T., et al. 2019, PASJ, 71, 43, doi: 10.1093/pasj/psz010

Hildebrandt, H., Köhlinger, F., van den Busch, J. L., et al. 2020, ApJ, 633, A69, doi: 10.1051/0004-6361/201834878

Hirata, C., & Seljak, U. 2003, MNRAS, 343, 459, doi: 10.1046/j.1365-8711.2003.06683.x

Hirata, C. M., & Seljak, U. 2004, Phys. Rev. D, 70, 063526, doi: 10.1103/PhysRevD.70.063526

Hsieh, B. C., & Yee, H. K. C. 2014, ApJ, 792, 102, doi: 10.1088/0004-637X/792/2/102

Huff, E., & Mandelbaum, R. 2017, ArXiv e-prints. https://arxiv.org/abs/1702.02600

Ivezić, Ž., Kahn, S. M., Tyson, J. A., et al. 2019, ApJ, 873, 111, doi: 10.3847/1538-4357/ab042c

Jarvis, M., Bernstein, G., & Jain, B. 2004, MNRAS, 352, 338, doi: 10.1111/j.1365-2966.2004.07926.x

Kaiser, N., & Squires, G. 1993, ApJ, 404, 441, doi: 10.1086/172297

Kaiser, N., Squires, G., & Broadhurst, T. 1995, ApJ, 449, 460, doi: 10.1086/176071

Kannawadi, A., Hoekstra, H., Miller, L., et al. 2019, A&A, 624, A92, doi: 10.1051/0004-6361/201834819

Kilbinger, M. 2015, Reports on Progress in Physics, 78, 086901, doi: 10.1088/0034-4885/78/8/086901

Koekemoer, A. M., Aussel, H., Calzetti, D., et al. 2007, ApJS, 172, 196, doi: 10.1086/520086

Komatsu, E., Kogut, A., Nolta, M. R., et al. 2003, ApJS, 148, 119, doi: 10.1086/377220

Laureijs, R., Amiaux, J., Arduini, S., et al. 2011, ArXiv e-prints. https://arxiv.org/abs/1110.3193

Leauthaud, A., Massey, R., Kneib, J.-P., et al. 2007, ApJS, 172, 219, doi: 10.1086/516598

Leonard, A., Lanusse, F., & Starck, J.-L. 2014, MNRAS, 440, 1281, doi: 10.1093/mnras/stu273

Li, H., & Zhang, J. 2021, ApJ, 911, 115, doi: 10.3847/1538-4357/abec6d

Li, X., Katayama, N., Oguri, M., & More, S. 2018, MNRAS, 481, 4445, doi: 10.1093/mnras/sty2548

Li, X., Yoshida, N., Oguri, M., Ikeda, S., & Luo, W. 2021a, arXiv e-prints, arXiv:2102.09707. https://arxiv.org/abs/2102.09707

Li, X., & Zhang, J. 2016, ApJ, 830, 116, doi: 10.3847/0004-637X/830/2/116

Li, X., Oguri, M., Katayama, N., et al. 2020, The Astrophysical Journal Supplement Series, 251, 19, doi: 10.3847/1538-4365/abbad1

Li, X., et al. 2021b, arXiv e-prints, arXiv:2107.00136. https://arxiv.org/abs/2107.00136

Li, Z., Liu, J., Zorrilla Matilla, J. M., & Coulton, W. R. 2019, Phys. Rev. D, 99, 063527, doi: 10.1103/PhysRevD.99.063527

Lupton, R., Gunn, J. E., Ivezić, Z., Knapp, G. R., & Kent, S. 2001, in Astronomical Society of the Pacific Conference Series, Vol. 238, Astronomical Data Analysis Software and Systems X, ed. J. Harnden, F. R., F. A. Primini, & H. E. Payne, 269

MacCrann, N., Becker, M. R., McCullough, J., et al. 2020, arXiv e-prints, arXiv:2012.08567. https://arxiv.org/abs/2012.08567

Mandelbaum, R. 2018, ARA&A, 56, 393, doi: 10.1146/annurev-astro-081817-051928

Mandelbaum, R., Slosar, A., Baldauf, T., et al. 2013, MNRAS, 432, 1544, doi: 10.1093/mnras/stt572

Mandelbaum, R., Hirata, C. M., Seljak, U., et al. 2005, MNRAS, 361, 1287, doi: 10.1111/j.1365-2966.2005.09282.x

Mandelbaum, R., Lanusse, F., Leauthaud, A., et al. 2018a, MNRAS, 481, 3170, doi: 10.1093/mnras/sty2420

Mandelbaum, R., Miyatake, H., Hamana, T., et al. 2018b, PASJ, 70, S25, doi: 10.1093/pasj/psx130

Martinet, N., Harnois-Déraps, J., Jullo, E., & Schneider, P. 2021, A&A, 646, A62, doi: 10.1051/0004-6361/202039679

Massey, R., & Refregier, A. 2005, MNRAS, 363, 197, doi: 10.1111/j.1365-2966.2005.09453.x

Massey, R., Heymans, C., Bergé, J., et al. 2007, MNRAS, 376, 13, doi: 10.1111/j.1365-2966.2006.11315.x

Medezinski, E., Oguri, M., Nishizawa, A. J., et al. 2018, Publications of the Astronomical Society of Japan, 70, 30, doi: 10.1093/pasj/psy009

Melchior, P., Moolekamp, F., Jerdee, M., et al. 2018, Astronomy and Computing, 24, 129, doi: 10.1016/j.ascom.2018.07.001

Miyatake, H., Battaglia, N., Hilton, M., et al. 2019, ApJ, 875, 63, doi: 10.3847/1538-4357/ab0af0

Miyazaki, S., Oguri, M., Hamana, T., et al. 2018a, PASJ, 70, S27, doi: 10.1093/pasj/psx120

Miyazaki, S., Komiyama, Y., Kawanomoto, S., et al. 2018b, PASJ, 70, S1, doi: 10.1093/pasj/psx063

Mukhanov, V. F., Feldman, H. A., & Brandenberger, R. H. 1992, Phys. Rep., 215, 203, doi: 10.1016/0370-1573(92)90044-Z

Murata, R., Oguri, M., Nishimichi, T., et al. 2019, Publications of the Astronomical Society of Japan, 71, doi: 10.1093/pasj/psz092

Murray, S. G., Power, C., & Robotham, A. S. G. 2013, Astronomy and Computing, 3, 23, doi: 10.1016/j.ascom.2013.11.001

Navarro, J. F., Frenk, C. S., & White, S. D. M. 1997, ApJ, 490, 493, doi: 10.1086/304888

Nishizawa, A. J., Hsieh, B.-C., Tanaka, M., & Takata, T. 2020, arXiv e-prints, arXiv:2003.01511. https://arxiv.org/abs/2003.01511

Nishizawa, T., et al. in prep.

Oguri, M. 2014, Monthly Notices of the Royal Astronomical Society, 444, 147, doi: 10.1093/mnras/stu1446

Oguri, M., & Hamana, T. 2011, MNRAS, 414, 1851, doi: 10.1111/j.1365-2966.2011.18481.x

Oguri, M., Miyazaki, S., Hikage, C., et al. 2018, PASJ, 70, S26, doi: 10.1093/pasj/psx070

Oguri, M., Lin, Y.-T., Lin, S.-C., et al. 2018, Publications of the Astronomical Society of Japan, 70, S20, doi: 10.1093/pasj/psx042

Planck Collaboration, Aghanim, N., Akrami, Y., et al. 2020, A&A, 641, A6, doi: 10.1051/0004-6361/201833910

Prat, J., Sánchez, C., Fang, Y., et al. 2018, Phys. Rev. D, 98, 042005, doi: 10.1103/PhysRevD.98.042005

Press, W. H., & Schechter, P. 1974, ApJ, 187, 425, doi: 10.1086/152650

Ragagnin, A., Dolag, K., Moscardini, L., Biviano, A., & D'Onofrio, M. 2019, MNRAS, 486, 4001, doi: 10.1093/mnras/stz1103

Reid, B., Ho, S., Padmanabhan, N., et al. 2016, MNRAS, 455, 1553, doi: 10.1093/mnras/stv2382

Riess, A. G., Filippenko, A. V., Challis, P., et al. 1998, AJ, 116, 1009, doi: 10.1086/300499

Rowe, B. T. P., Jarvis, M., Mandelbaum, R., et al. 2015, Astronomy and Computing, 10, 121, doi: 10.1016/j.ascom.2015.02.002

Rykoff, E. S., Rozo, E., Busha, M. T., et al. 2014, ApJ, 785, 104, doi: 10.1088/0004-637X/785/2/104

Schneider, P., van Waerbeke, L., & Mellier, Y. 2002, A&A, 389, 729, doi: 10.1051/0004-6361:20020626

Sérsic, J. L. 1963, Boletin de la Asociacion Argentina de Astronomia La Plata Argentina, 6, 41

Sheldon, E. S., Becker, M. R., MacCrann, N., & Jarvis, M. 2020, ApJ, 902, 138, doi: 10.3847/1538-4357/abb595

Sheldon, E. S., & Huff, E. M. 2017, ApJ, 841, 24, doi: 10.3847/1538-4357/aa704b

Shirasaki, M., Hamana, T., Takada, M., Takahashi, R., & Miyatake, H. 2019, MNRAS, 486, 52, doi: 10.1093/mnras/stz791

Shirasaki, M., & Takada, M. 2018, MNRAS, 478, 4277, doi: 10.1093/mnras/sty1327

Shirasaki, M., Takada, M., Miyatake, H., et al. 2017, MNRAS, 470, 3476, doi: 10.1093/mnras/stx1477

Simon, P., Taylor, A. N., & Hartlap, J. 2009, MNRAS, 399, 48, doi: 10.1111/j.1365-2966.2009.15246.x

Spergel, D., Gehrels, N., Baltay, C., et al. 2015, ArXiv e-prints. https://arxiv.org/abs/1503.03757

Starck, J., Murtagh, F., & Bertero, M. 2015, Starlet transform in astronomical data processing, Vol. 1 (United States: Springer New York), 2053–2098

Takada, M., & Jain, B. 2003, MNRAS, 340, 580, doi: 10.1046/j.1365-8711.2003.06321.x

Takahashi, R., Hamana, T., Shirasaki, M., et al. 2017, ApJ, 850, 24, doi: 10.3847/1538-4357/aa943d

Tanaka, M. 2015, ApJ, 801, 20, doi: 10.1088/0004-637X/801/1/20

Tanaka, M., Coupon, J., Hsieh, B.-C., et al. 2018, Publications of the Astronomical Society of Japan, 70, S9, doi: 10.1093/pasj/psx077

Tinker, J., Kravtsov, A. V., Klypin, A., et al. 2008, ApJ, 688, 709, doi: 10.1086/591439

Wang, W., & White, S. D. M. 2012, MNRAS, 424, 2574, doi: 10.1111/j.1365-2966.2012.21256.x

Wang, W., Han, J., Sonnenfeld, A., et al. 2019, MNRAS, 487, 1580, doi: 10.1093/mnras/stz1339

Wen, Z. L., & Han, J. L. 2015, ApJ, 807, 178, doi: 10.1088/0004-637X/807/2/178

Wu, L., Yang, Y., & Liu, H. 2014, Computational Statistics & Data Analysis, 70, 116, doi: https://doi.org/10.1016/j.csda.2013.08.012

Yang, X., Mo, H. J., van den Bosch, F. C., & Jing, Y. P. 2005, MNRAS, 356, 1293, doi: 10.1111/j.1365-2966.2005.08560.x

Yang, X., Mo, H. J., van den Bosch, F. C., et al. 2007, ApJ, 671, 153, doi: 10.1086/522027

Yang, X., Xu, H., He, M., et al. 2021, ApJ, 909, 143, doi: 10.3847/1538-4357/abddb2

Zhang, J., & Komatsu, E. 2011, MNRAS, 414, 1047, doi: 10.1111/j.1365-2966.2011.18436.x

Zhang, J., Luo, W., & Foucaud, S. 2015, JCAP, 1, 24, doi: 10.1088/1475-7516/2015/01/024

Zhang, J., Zhang, P., & Luo, W. 2017, ApJ, 834, 8, doi: 10.3847/1538-4357/834/1/8

Zou, H. 2006, Journal of the American Statistical Association, 101, 1418, doi: 10.1198/016214506000000735

Zou, H., & Hastie, T. 2005, Journal of the Royal Statistical Society Series B, 67, 301, doi: 10.1111/j.1467-9868.2005.00503.x

Zou, H., & Zhang, H. H. 2009, Annals of Statistics, 37, 1733, doi: 10.1214/08-AOS625

Zuntz, J., Sheldon, E., Samuroff, S., et al. 2017, ArXiv e-prints. https://arxiv.org/abs/1708.01533